A Lead-Acid Flow Battery for Utility Scale Energy Storage and Load Levelling

By

Richard George Andrew Wills B.Sc M.Res

Thesis for the degree of Doctor of Philosophy

Department of Chemistry

University of Southampton

October 2004

THE UNIVERSITY OF SOUTHAMPTON

ABSTRACT

THE SCHOOL OF CHEMISTRY

Doctor of Philosophy

A LEAD-ACID FLOW BATTERY FOR UTILITY SCALE ENERGY STORAGE AND LOAD LEVELLING

By

Richard George Andrew Wills B.Sc M.Res

This thesis describes the chemistry, electrochemistry and characterisation of a lead-acid flow battery with no membrane separator and a single electrolyte, concentrated lead(II) in aqueous methanesulfonic acid.

Voltammetry at rotating disc electrodes is used to investigate the electrode reactions and define conditions suitable for high rate deposition / dissolution of lead and lead dioxide from aqueous methanesulfonic acid. The solubility of lead(II) in aqueous methanesulfonic acid was determined and the conductivity of the electrolyte was assessed as a function of Lead(II) and methanesulfonic acid concentrations.

A small, parallel plate flow battery was constructed and its performance studied as a function of current density, temperature, electrolyte composition, flow rate, interelectrode spacing, state of charge and electrical connection to the electrodes.

The performance is shown to be modified by the addition of various additives to the electrolyte. Inorganic ions (Ni^{2+}, Fe^{3+} and Sb^{3+}) were investigated as possible additives for co-deposition at the positive electrode to enhance the electrical properties of the PbO_2 deposit. Sodium ligninsulfonate and polyethylene glycol-200 were investigated as possible additives to suppress the formation of dendritic Pb growths and promote the deposition of smooth, compact Pb layers. The former was found to improve the performance of the battery.

Contents

Acknowledgments

I would like to express my gratitude to Professor Derek Pletcher for his friendship and guidance throughout the project and during the writing of this thesis.

I wish to thank Regenesys Technologies Ltd for their financial support and would also like to mention the work of Dr Jon Cox of Regenesys Technologies Ltd with reference to the fabrication of the electrodes. My thanks also go to The University of Southampton for the opportunity to conduct this research.

My regards go to everyone in Electrochemistry, particularly those on the 7th floor, whom I have worked with and enjoyed the company of over the past three years.

Best wishes go to my family who have always provided enthusiastic backing for whatever enterprise I chose to pursue.

Finally, a special mention for my wife Claire to whom this thesis is dedicated. Without her encouragement and support the past few years would have been considerably harder and more arduous.

List of Abbreviations and Symbols (with typical units)

A	Planar geometric area (cm^2).
A_{cell}	Cross sectional area of flow compartment, width × separation (cm^2).
A_e	Active surface area per unit volume of a three dimensional electrode (cm^{-1}).
a_i	Activity of species *i*.
c_i	Concentration of species *i* (mol dm^{-3} or mol cm^{-3}).
E	Potential (V vs. SCE or mV vs. SCE).
E_{Cell}	Cell potential away from equilibrium (V).
E^e_{cell}	Equilibrium potential of a cell (V).
E^0_e	Formal potential (V).
E^e_{-ve}	Electrode potential of negative electrode (V).
E^e_{+ve}	Electrode potential of positive electrode (V).
$E_{O/C}$	Open circuit potential of a galvanic cell (V or mV)
F	Faraday constant (96485 C mol^{-1}).
j	Current density (mA cm^{-2}).
j_{anodic}	Anodic current density (mA cm^{-2}).
$j_{cathodic}$	Cathodic current density (mA cm^{-2}).
j_L	Limiting current density (mA cm^{-2}). Calculated using planar geometric area of electrode, *A*.
j_0	Exchange current density (mA cm^{-2})
I	Current (mA).
I_L	Limiting current (mA).
κ	Electrolyte conductivity (Ω^{-1} cm^{-1})
k_m	Mass transport coefficient (cm s^{-1}).
l	Electrode separation (cm).
n	Number of electrons per molecule of reactant in electron transfer reaction.
η	Overpotential (mV)

$\eta_{nucl.}$	Nucleation overpotential (mV).
Q_{anodic}	Anodic charge applied to an RDE (C).
$Q_{cathodic}$	Cathodic charge applied to an RDE (C).
Q_c	Charge applied to flow cell (C).
Q_d	Discharge applied to flow cell (C).
Q_v	Volumetric flow rate ($cm^3\ s^{-1}$).
$\frac{Q_{anodic}}{Q_{cathodic}}$	Efficiency of PbO_2 deposition / stripping onto an RDE (%).
$\frac{Q_{cathodic}}{Q_{anodic}}$	Efficiency of Pb deposition / stripping onto an RDE (%).
$\frac{Q_d}{Q_c}$	Charge efficiency of flow cell (%).
RDE	Rotating disc electrode.
R	Resistance (Ω).
Type I	Core plate electrode: carbon powder / polymer composite plate of thickness 3.2 mm, with no active layer.
Type II	Ni foam electrode: Core plate onto which nickel foam (40 ppi, initial thickness 1.8 mm) is heat bonded at a temperature of 433 K and a pressure of circa 6 kg cm^{-2}.
Type III	RVC foam electrode: Core plate onto which an active tile of reticulated vitreous carbon (70 ppi, initial thickness 1.5 mm) is bonded using a temperature of 433 K and pressure of 6 kg cm^{-2}.
Type IV	Scraped RVC electrode: As type III but with the protruding RVC structure removed with a sharp blade.
Type V	Carbon 500 electrode: "S" series Regenesys commercial electrode, with tile comprised of; activated carbon particles heat bonded with PVDF binder. Tile fused to core using a pressure of 29 kg cm^{-2}.
Type VI	Carbon 4500 electrode: As type V, but tile fused to core plate using a pressure of 261 kg cm^{-2}.
Type VII	Cloth electrode: Woven carbon fibre cloth, fused to core using a pressure of circa 6 kg cm-2 and a temperature of 433 K over a two second period.

Type VIII	AC7 electrode: As type V and VI, but with activated carbon particles, without PVDF binder, fused to the core.
U	Cell voltage (V)
U_c	Charge voltage (V).
U_d	Discharge voltage (V).
$\bar{U}_c$	Average charge voltage (V).
$\bar{U}_d$	Average discharge voltage (V).
$\bar{U}_{50}$	Average voltage during first 50 s of discharge (V).
$\bar{U}_{150}$	Average voltage during first 150 s of discharge (V).
V_e	Volume of a three dimensional electrode (cm^3).
v_L	Mean linear flow rate ($cm\ s^{-1}$).
ω	Rotation rate (rpm or radians s^{-1}).
$\frac{W_d}{W_c}$	Energy Efficiency (%).

Chapter 1: Introduction

1.1 Background

1.1.1 Fluctuations in Power Usage: The majority of electrical power produced in this country is generated by dedicated power utility companies and distributed to consumers, both domestic and business, via the National Grid. Customers expect electricity to be available instantly, as and when they require it. As a result the demand for electrical power can fluctuate greatly at different times of the day/night,[1-3] and indeed over longer time periods, such as between summer and winter.[2, 3] Resulting from these variations in usage, power generation can be categorised into three bands:

♦ Baseload: Electricity produced to satisfy the minimum supply requirement. Typically this is produced using the newest, most efficient generating facilities. These generators will be operated to give an optimum and usually constant output.

♦ Intermediate: Production to meet general increases in demand and to cover any requirements that are between baseload and maximum (peak) usage.

♦ Peak: The maximum amount of production needed to supply the electricity required during peak usage. This is usually produced with the least efficient, older power plants that are only brought online when needed.

Figure 1.1 shows the typical power requirement over a 24 hour period in the United Kingdom.[1] One challenge for electricity suppliers is that of matching the supply of power to the total demand at all times, increasing from the baseload to intermediate and peak power production. This requires the ability to react quickly to variations in power usage and resources of sufficient capacity to cover the maximum (peak) demand. Traditionally this necessitates having standby peak power production facilities that are idle for considerable time periods, coming online only occasionally during times of high demand. Associated with these standby facilities are considerable capital, infrastructure, maintenance and fuel costs.[1, 3]

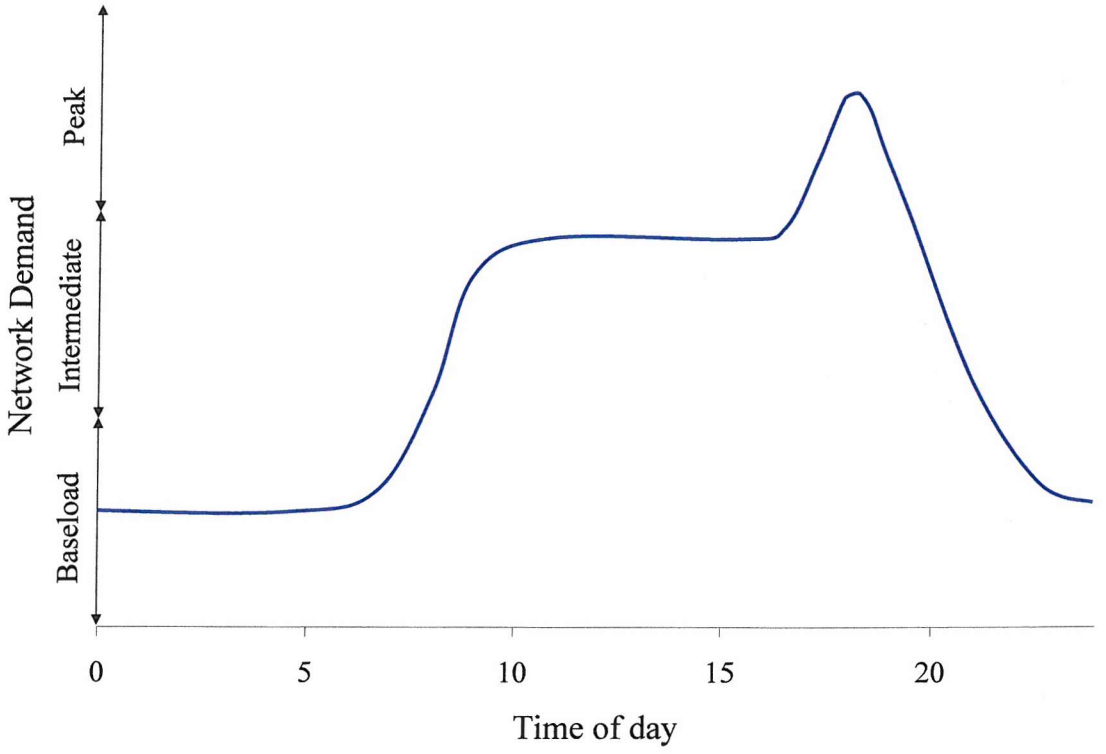

Figure 1.1: *Typical daily energy production profile for the UK, showing baseload, intermediate and peak production to balance demand.*

1.1.2 Load Levelling: A more efficient solution to the problem of matching power supply to demand is the development of a load levelling device. This would be charged during periods of low demand, typically at night, and then discharged at times of high usage, generally in the early evening. Theoretically, storing energy in this way reduces the quantity of power production facilities, with each of the remaining units able to operate at full / optimum capacity. The way in which such a system may be integrated into the supply network is shown in figure 1.2.

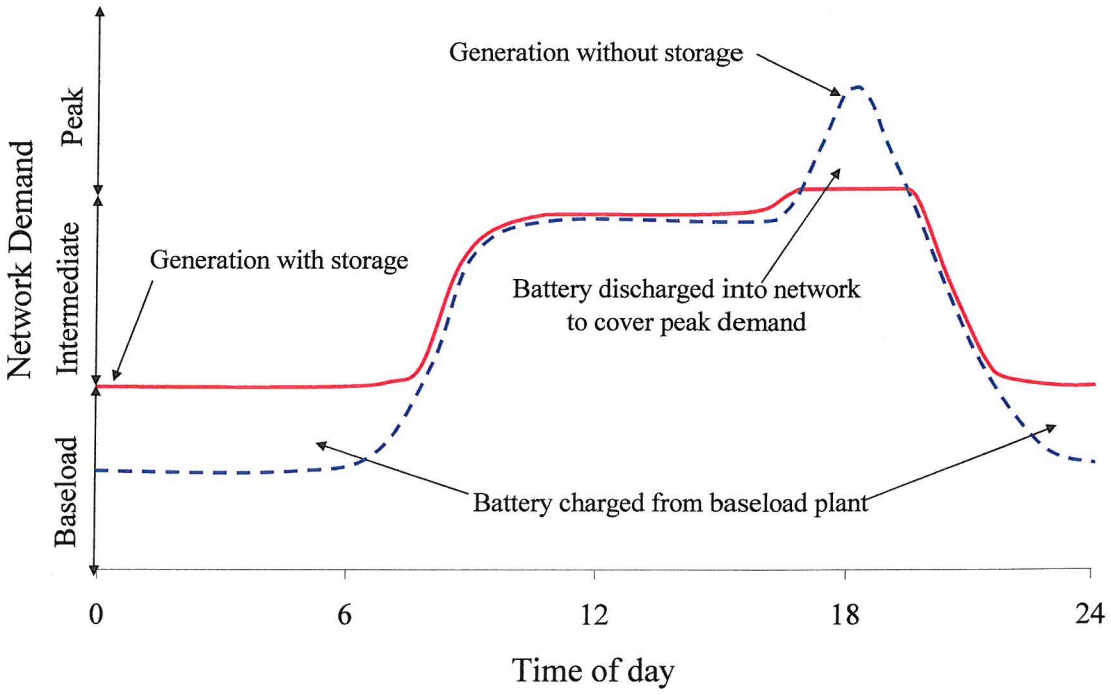

Figure 1.2: *Energy production profile showing how a load levelling battery would be intergrated into the system.*

1.1.3 Renewable Energy: The ability to store electrical energy is also a necessity if renewable power sources are to be fully exploited. Such sources typically harness the power of nature to generate electricity and are thus inherently sporadic in their output. For example solar cells can only operate while the sun is shining.

1.1.4 Reserve Storage: Reserve storage gives improved stability and reliability to supply networks. Not only can the stored energy be released when needed in a load levelling function, it can also be used to smooth voltage spikes, maintain frequency and for short periods, if needed, act as a substitute for normal production facilities.

1.1.5 Black Start: Worldwide there has been, in recent times, an increase in the number of major electricity blackouts.[4] If an electricity production unit is partially or fully taken offline, through failure or for routine maintenance, a large amount of power is required to bring the power station from a non-operational state back to one of power production. Different types of generators have various requirements specific to their individual technologies, however the general features of reenergizing a power station and its associated network include:[4]

- ♦ Sufficient power to restart the production plant.
- ♦ Power for running auxiliary systems required by the power station.
- ♦ Control of voltage and frequency over the network.
- ♦ Sequence for re-supplying external loads (consumers and substations).

The final two points depend heavily on system stability whilst reconnecting loads to the supply grid. Clearly a storage device, such as a battery, that has a quick response time for releasing energy is advantageous in such situations, compared to less responsive devices (e.g. diesel generators).

1.2 What is a Battery?

1.2.1 Basic Principles: A battery can be defined as a device that, during discharge produces electrical energy directly from a chemical reaction. This delivers a direct current (DC) of electricity to an external load. Batteries comprise one or more individual cells, which in turn comprise a positive and negative current collector (electrode) at which electron transfer takes place. Typically each cell produces a relatively small amount of power, so consequently groups of cells are arranged in series, parallel or in bipolar configurations to obtain a desired voltage and current. Dependant on their application batteries are separated into two categories:

♦ Primary Batteries: A single use battery that, once manufactured, may only be discharged a single time.

♦ Secondary Batteries: A battery that may be charged and discharged more than once.

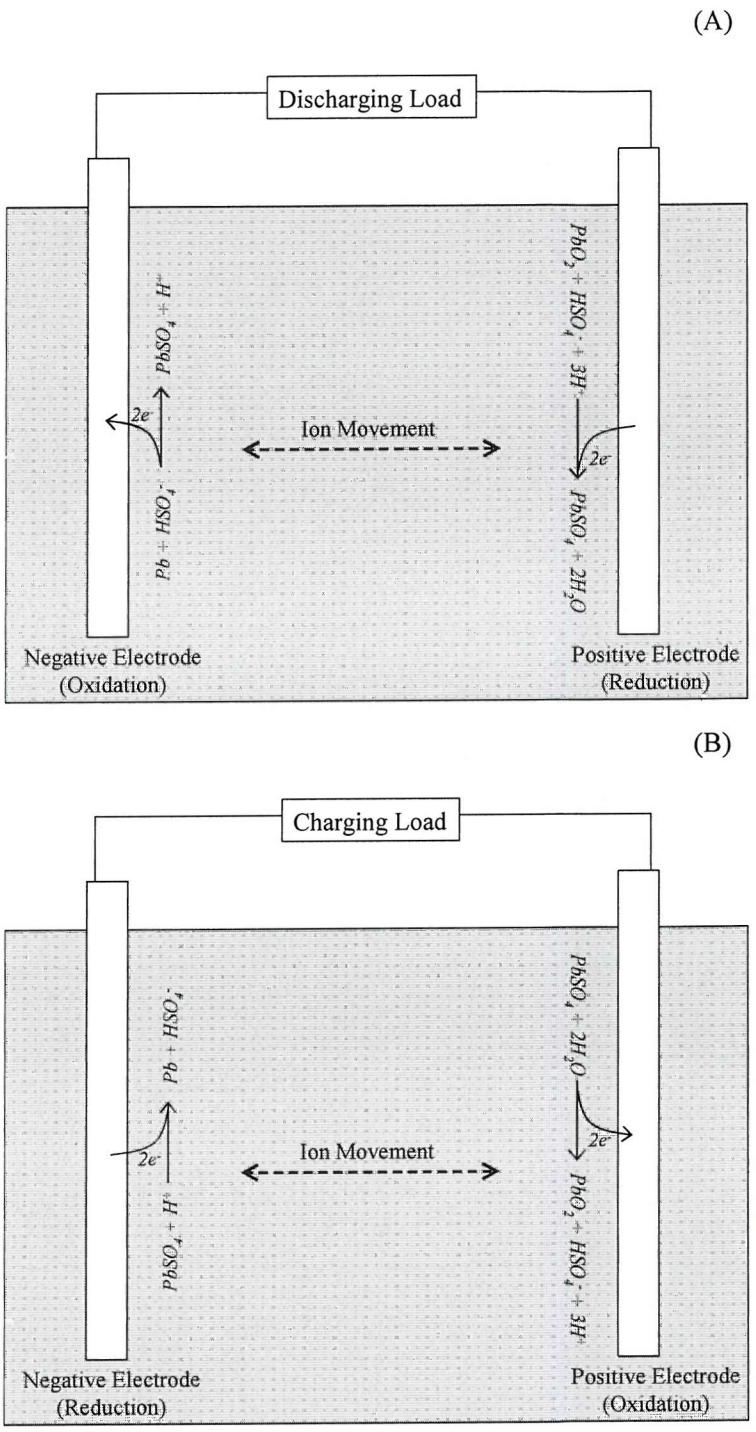

Figure 1.3: *Direction of current flow and electron transfer during (A) discharging and (B) charging of a secondary battery.*

Using the lead-acid battery as an example, Figure 1.3 presents a diagram of a secondary battery showing the direction of ion flow within the cell and electron transfer at the electrodes during discharging / charging. It should be noted that a primary battery operates in exactly the same manner as a secondary battery during discharge, as shown in figure 1.3 A.

1.2.2 Cell Potential: Any electrode in contact with an electrolyte solution develops a specific potential, determined by the electrode material and electrolyte composition.

When two electrodes are placed in the same electrode solution and connected via an external circuit a Galvanic cell is formed. The equilibrium potential of the cell is defined as the difference between the equilibrium potentials of the two electrode couples, making up the positive and negative electrodes, and is given in equation *1*, where E^e_{cell} is the equilibrium potential of the cell, E^e_{+ve} and E^e_{-ve} are the equilibrium potentials of the positive and negative electrode.

$$E^e_{cell} = E^e_{+ve} - E^e_{-ve} \qquad (1)$$

Thus, by definition the batteries' open circuit potential is always positive and the positive electrode is designated to be the plate at which reduction of the active material takes place during discharge and, vice versa oxidation occurs during charge. Similarly at the negative electrode, oxidation occurs during discharge and reduction occurs during charge.

At the equilibrium potential for an electrode reaction, no net current flows and the rates of oxidation and reduction are equal. However the concentrations of the oxidant and reductant are not necessarily equal and so the rate constants for oxidation and reduction may not be equal. At the formal potential, E^0_e, the concentrations of the oxidant and reductant species are equal and thus the rate constants are equal. Under these conditions, the current associated with oxidation is equal but opposite in sign to the current associated

with reduction and these partial current densities are termed the exchange current density, j_0. This is true for both the positive and negative electrode couples.

Under non-standard conditions, the potential can be estimated from the Nernst equation and this will be illustrated using the example of the lead-acid battery.

1.2.3 Electrode Reactions: The lead-acid battery operates with PbO_2 as the active material of the positive electrode and Pb as the active material of the negative electrode. Traditionally the electrolyte is aqueous sulfuric acid (H_2SO_4). The half cell reactions for each of the electrodes in the traditional lead-acid battery are given in equations *2* and *3*.

Positive electrode:

$$PbO_2 + HSO_4^- + 3H^+ + 2e^- \underset{\text{Charge}}{\overset{\text{Discharge}}{\rightleftharpoons}} PbSO_4 + 2H_2O \qquad E^0 = +1.69\ V \quad (2)$$

Negative electrode:

$$Pb + HSO_4^- \underset{\text{Charge}}{\overset{\text{Discharge}}{\rightleftharpoons}} PbSO_4 + H^+ + 2e^- \qquad E^0 = -0.36\ V \quad (3)$$

Combining these electrode reactions gives the overall cell reaction (equation *4*). It can be seen that $PbSO_4$ is formed at both electrode plates during discharge and unlike most other battery systems, the H_2SO_4 electrolyte not only acts as an ion conductor but takes part in the chemical reactions during charge and discharge of the battery.

Overall cell reaction:

$$Pb + PbO_2 + 2HSO_4^- + 2H^+ \underset{\text{Charge}}{\overset{\text{Discharge}}{\rightleftharpoons}} 2PbSO_4 + 2H_2O \quad E^0 = +2.05\ V \quad (4)$$

The equilibrium potential of each electrode may be related to the standard potential for the electrode reactions via the Nernst equation. Equations 6 and 7 gives the Nernst equation, written for the positive and negative electrode reactions of the lead-acid battery, where E^0_{+ve} and E^0_{-ve} are standard electrode potentials for the positive and negative electrodes respectively and a_i is the activity for species *i*.

$$E^e_{+ve} = E^0_{+ve} + \frac{2.3RT}{2F}\log\frac{a^3_{H^+}a_{HSO_4^-}a_{PbO_2}}{a_{PbSO_4}} \qquad (5)$$

$$E^e_{-ve} = E^0_{-ve} + \frac{2.3RT}{2F}\log\frac{a_{H^+}a_{PbSO_4}}{a_{Pb}a_{HSO_4^-}} \qquad (6)$$

Combining and rearranging equations *5* and *6* gives the Nernst equation for the overall cell reaction for the lead-acid battery, equation *7*.

$$E^e_{Cell} = E^0_{+ve} - E^0_{-ve} + \frac{2.3RT}{2F}\log\frac{a^2_{H^+}a_{PbO_2}a_{Pb}a^2_{HSO_4^-}}{a^2_{PbSO_4}} \qquad (7)$$

In many cases the equation can be simplified further if the activities of solid reactants are assumed to be unity and the remaining activities approximated by the concentration of each species, as given in equation 8.

$$E^e_{Cell} = E^0_{+ve} - E^0_{-ve} + \frac{2.3RT}{2F}\log c^2_{H^+}c^2_{HSO_4^-} \qquad (8)$$

At the open circuit potential a dynamic equilibrium exists at each electrode, i.e. both electrode processes occur in the charge and discharge directions but at the same rate so that no net current flows. At either electrode, the rate of oxidation equals the rate of reduction and is defined as the exchange current density, j_0. The Gibbs free energy associated with

the chemical change in the battery is related to the equilibrium or open circuit potential by equation *9*.

$$\Delta G = -2F E^{e}_{cell} \qquad (9)$$

1.2.4 On Load Cell Voltage: When a current is passed by a galvanic cell the potential difference between the electrodes is altered from the open circuit potential to an on-load voltage. During discharge this is denoted U_d and during charge U_c. As the load current is increased, so U_d decreases and U_c increases. The magnitude of the difference between the open circuit potential and the on-load voltage is determined by a combination of ohmic drop through the cell, IR_{cell}, and polarisation (overvoltage, η) of the electrodes. Equation *10* presents the dependence of the overpotential on the current density, exchange current density and temperature.

$$\eta = \frac{2.3RT}{2nF} \log \frac{j}{j_0} \qquad (10)$$

The cells' on-load voltages are described by equations *11* and *12*, where η_{+ve} and η_{-ve} are the overvoltages associated with the positive and negative electrodes respectively and IR_{cell} is the sum of all the cells' internal ohmic losses.

Discharge voltage:

$$U_d = E^{0}_{Cell} - \eta_{+ve} - \eta_{-ve} - IR_{cell} \qquad (11)$$

Charge voltage:

$$U_c = E^{0}_{Cell} + \eta_{+ve} + \eta_{-ve} + IR_{cell} \qquad (12)$$

The overpotentials and *IR* drops are therefore always inefficiencies that lead to an increase in temperature of the cell.

1.2.5 Efficiency: The efficiency of secondary batteries during discharge may be measured by a variety of methods. For convenience, within this project, two means of measuring efficiency are defined:

♦ *Coulombic Efficiency*: The coulombic efficiency is simply the ratio between the quantity of charge passed, in coulombs, during charge and discharge. This can be calculated according to equation *13*, where $_d$ and $_c$ denote charging and discharging quantities respectively, Q is the charge passed, I is the current applied to the cell and t is the length of time the current is passed.

$$\frac{Q_d}{Q_c} = \frac{\int I_d dt}{\int I_c dt} \qquad (13)$$

However, when constant currents are used the relationship can be simplified to equation *14*.

$$\frac{Q_d}{Q_c} = \frac{(It)_d}{(It)_c} \qquad (14)$$

♦ *Energy Efficiency*: The coulombic ratio does not take into account energy losses via, for example, ohmic drop and heating of the cell. The energy efficiency addresses this by factoring in the voltage during charging and discharging the cell. In this project the energy used to charge or discharge the cell was calculated by integrating the area beneath a voltage vs. time plot of the discharge or charge period, as given by equation *15*. Where W is the energy used and U is the voltage of the cell during charge or discharge.

$$\frac{W_d}{W_c} = \frac{Q_d \int U_d dt}{Q_c \int U_c dt} \qquad (15)$$

1.3 Large Scale Energy Storage

1.3.1 Traditional Methods: This section gives a brief overview of methods used to store large quantities of energy (10^4 – 10^8 Wh) and with the ability to discharge into an electricity network.

♦ *Pumped Hydroelectric*:[5-9] This is the most widely used method of energy storage for load levelling purposes. Pumped hydroelectric energy storage consists of two large water reservoirs situated at different altitudes, connected via conduit pipes with a dynamo and pump system situated towards the lower reservoir. The greater the vertical distance (head) between the lower and upper reservoirs, the more potential energy can be stored. During times of low power usage water is pumped from the lower reservoir up to the top reservoir. Then when needed, during peak usage, the water is allowed to flow back to the lower reservoir, producing power via the dynamo. With efficient pumps and generators the efficiency of such systems can be as high as 80 %. The storage capacity is only limited by the size of the two reservoirs. One of the best known facilities is the Dinorwig plant in Wales. This plant can produce 1800 MW from its 6 million cubic meter reservoirs and 600 m head. The obvious disadvantage of this method of energy storage is that it is limited to specific geographic locations.

♦ *Compressed Air*:[9, 10] During off peak times air is pumped into large storage tanks, typically underground rock caverns. During times of peak energy consumption the air is then released, turning a turbine to produce electricity. Alternatively the stored air is mixed with natural gas and burnt as it is released. This improves the energy efficiency of the system. Compressed air plants are only limited in capacity by the size of the storage cavern. Currently the largest operating system is a 290 MW plant operating in Huntorf, Germany. As with pumped hydro and underground thermal energy the geological dependence of sighting such energy storage facilities is a considerable disadvantage.

♦ *Superconducting Magnets*: Energy may be stored in the magnetic field of DC current flowing in the coil of a superconducting magnet. Advantages of this system are that superconducting magnets can be charged and discharged rapidly and over many cycles without degradation of the system. This storage method is also very efficient: circa 95 %. However, currently, operational systems are only capable of storing around 10 MW.

Typically this technology is used for smoothing electrical supply for specific users, for example factories in which precision instruments, that are sensitive to voltage variation, are used.

♦ *Supercapacitors*:[11-13] Supercapacitors store energy by the separation of positive and negative electrostatic charge. Normal capacitors are constructed by placing a thin insulating layer (dielectric) between two conducting plates. Typically supercapicitors contain an electrolyte to enable electrostatic storage of energy using ions. Using ions results in a lower voltage than traditional capacitors but longer charge / discharge characteristics due to the relatively slow movement of ions compared to electrons. As there is no chemical change associated with the energy storage, supercapacitors have a much longer cycle life (circa 10^5 cycles) than batteries (10^3 cycles) and no overpotentials.

♦ *Flywheel*:[5, 6, 14-20] The principle behind flywheel energy storage is relatively simple; Energy is used to rotate a disc on a low friction bearing, this kinetic energy can then be converted into electrical energy when needed. Traditionally such flywheels were only used in small scale applications for voltage smoothing, their inefficiencies preventing large scale storage or prolonged output. However the development of superconducting magnetic bearings has increased their efficiency by reducing idling loses to a negligible amount. Currently these superconducting magnetic bearing devices are quite small; test systems circa 10 kW have been produced that operate at circa 84 % efficiency.

♦ *Underground Thermal Energy*:[9, 21, 22] Typically this technology involves having two aquifers: one for warm water and one for cold water. During winter, water from the warm aquifer is pumped to the cold aquifer via a heat exchanger. Energy removed in this way is used for heating buildings. During summer months this process is reversed and cold water used for cooling. Clearly this method of energy storage, being limited to heating cooling purposes, is not a suitable method for the commercial storage and release of electrical energy.

1.3.2 Flow Batteries: Flow systems differ from conventional batteries by having one or more of the active materials stored in an external reservoir, in a liquid phase. The active material(s) and supporting electrolyte are pumped through the cells during operation.

Figure 1.4 presents a schematic diagram of a general flow battery, operating with two electrolytes.

The storage capacity of flow batteries is therefore limited by the size of the electrolyte reservoir and the power of the battery is determined by the size of the individual cells and their assembly. Typically the cells are arranged in a bipolar stack of electrodes, as shown in figure 1.5. Bipolar stacks are capped at each end by either a positive or negative current collecting plate, between which are a series of plates whose opposite sides act as positive and negative electrodes. This is achieved by having electrolyte solution flowing past both sides of these plates and operating one side as the positive electrode and the other as a negative electrode. One disadvantage of such systems is current leakage through the electrolyte solution rather than passing via the electrodes. This is addressed by increasing the flow path between cell chambers to such an extent that *IR* drop through the electrolyte is significant enough to prevent flow of current other than through the electrodes.

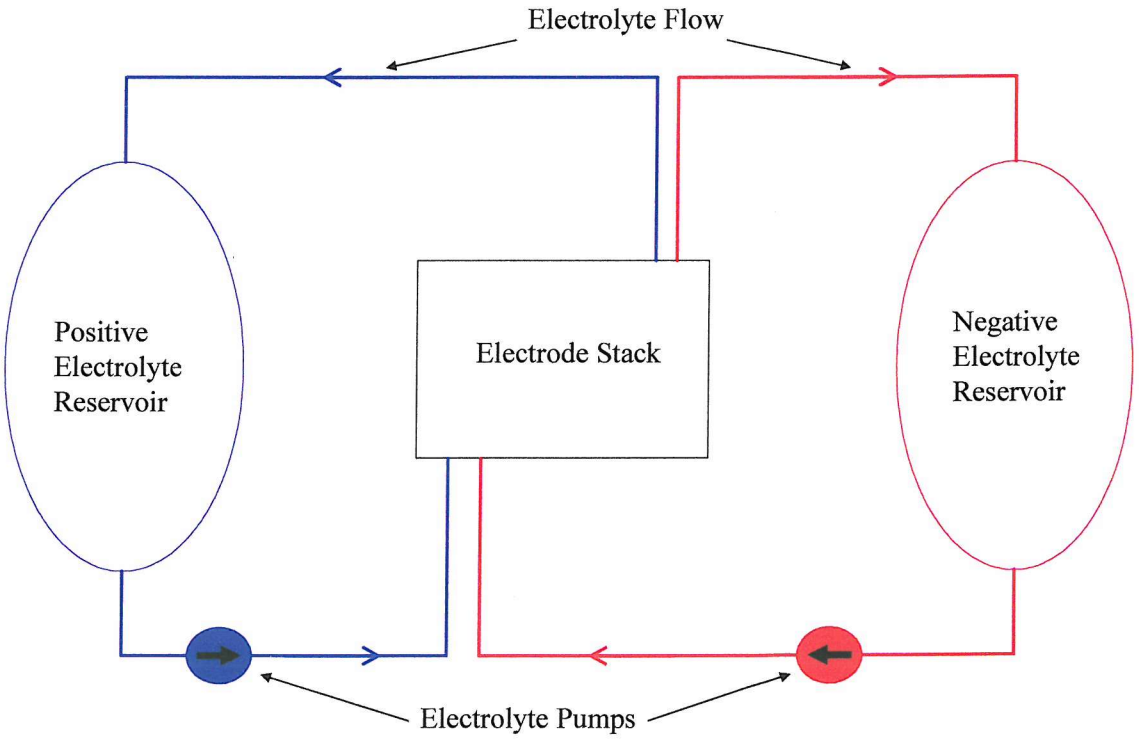

Figure 1.4: *Schematic diagram of a flow battery operating with two electrolytes held in separate reservoirs.*

Separating the energy and power functions enables the technology to be scaled according to specific requirements and in theory used on a very large scale. However flow technology can only be applied to chemical systems in which the desired materials are liquid or have sufficient solubility in the chosen electrolyte to enable pumping.

As with conventional batteries, flow systems operate using direct current and therefore require a converter and suitable transformer to link them to AC power distribution networks.

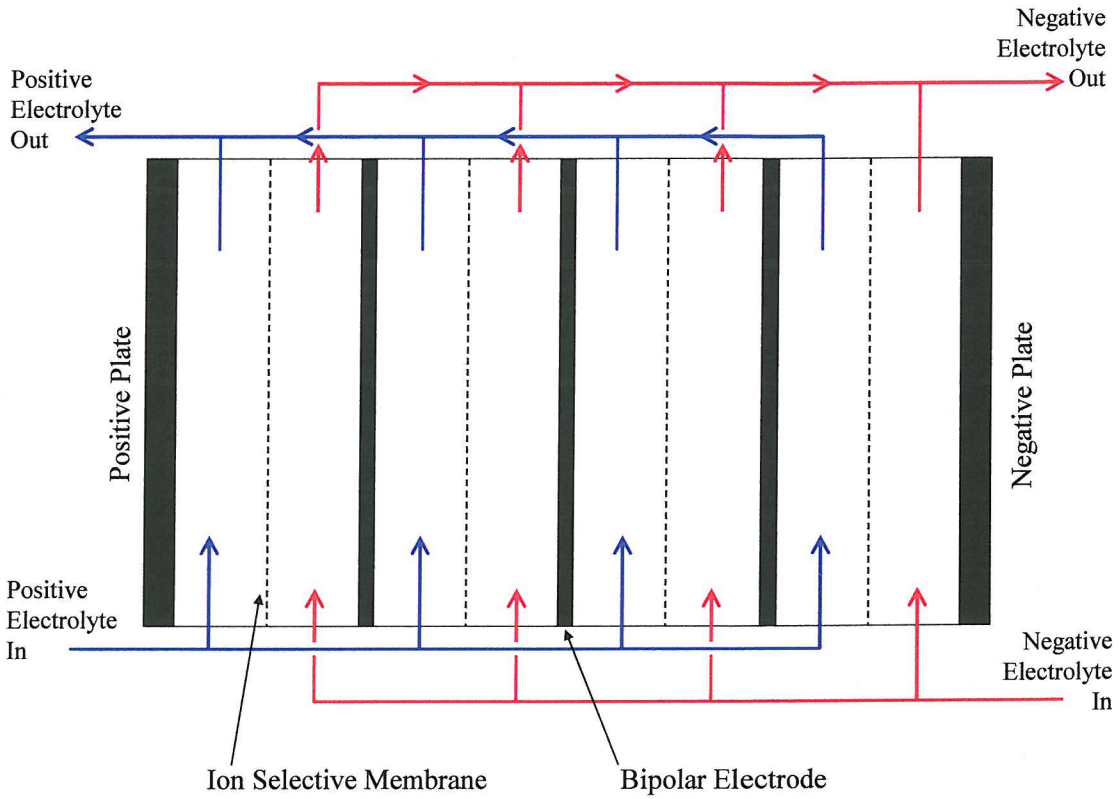

Figure1.5: *Diagram showing a bipolar stack arrangement of electrodes. System operating with two electrolytes.*

Several chemical systems are considered suitable for use in flow batteries:

♦ *Iron-Chromium*:[3, 23-25] An early example is the iron-chromium battery which operates via the reactions given in equations *16* and *17*. The major obstacle to this

technology is finding a suitable separator material to prevent cross contamination of the iron and chromium ions and overcoming large overpotentials.

Positive electrode:

$$Fe^{3+} + e^{-} \underset{\text{Charge}}{\overset{\text{Discharge}}{\rightleftharpoons}} Fe^{2+} \qquad E^{0} = +0.77\ V \qquad (16)$$

Negative electrode:

$$Cr^{2+} \underset{\text{Charge}}{\overset{\text{Discharge}}{\rightleftharpoons}} Cr^{3+} + e^{-} \qquad E^{0} = -0.41\ V \qquad (17)$$

♦ *Bromine-Polysulfide*:[3, 26-28] This system has been researched by Regenesys Technologies and is based on the electrode reactions given in equations *18* and *19*. The chemistry differs from most other flow batteries as the redox active species for both electrode reactions are anions. In the uncharged state the positive electrolyte comprises of aqueous sodium bromide and the negative electrolyte consists of aqueous sodium polysulfide. Charging the system, the bromide ions are oxidised to bromine and stored as a sodium tribromide complex, while sulfur, present as the polysulfide anion, is converted to sulfide. During discharge bromine is reduced to bromide and the sulfide is oxidised to sulfur. The cells are arranged in bipolar stacks and the two electrolyte solutions are separated by a Nafion membrane, permeable to Na^{+} to maintain electrical balance. As with the iron-chromium battery the selectivity of the cell membrane is not 100 %. Along with the desired Na^{+} ion transfer, S^{2-} ions and to a lesser extent Br_2 and H_2O also permeate the membrane. Despite this, the efficiency was high enough to warrant the planned construction of a 100 MWhr storage plant.

Positive electrode:

$$Br_2 + 2e^- \underset{\text{Charge}}{\overset{\text{Discharge}}{\rightleftharpoons}} 2Br^- \qquad E^0 = +1.07\ V \qquad (18)$$

Negative electrode:

$$S^{2-} \underset{\text{Charge}}{\overset{\text{Discharge}}{\rightleftharpoons}} S + 2e^- \qquad E^0 = -0.51\ V \qquad (19)$$

♦ *Vanadium*:[3, 29-34] The vanadium system overcomes some of the problems associated with cross contamination of the positive and negative electrolytes as both solutions comprise vanadium in different oxidation states. Therefore contamination between the two electrolytes only results in a lowering of battery efficiency and not unwanted chemical species in the electrolyte. The system operates via the reactions given in equations *20* and *21*.

Positive electrode:

$$VO_2^+ + 2H^+ + e^- \underset{\text{Charge}}{\overset{\text{Discharge}}{\rightleftharpoons}} VO^{2+} + H_2O \qquad E^0 = +1.00\ V \qquad (20)$$

Negative electrode:

$$V^{2+} \underset{\text{Charge}}{\overset{\text{Discharge}}{\rightleftharpoons}} V^{3+} + e^- \qquad E^0 = -0.26\ V \qquad (21)$$

♦ *Zinc-Bromine*:[3, 26, 35, 36] The previous three systems operate with the active materials entirely in the solution state and the electrodes acting only as electron transfer surfaces. The zinc-bromine battery differs slightly and during operation the electrodeposition/dissolution of zinc occurs at the negative electrode. Also the bromine produced is stored in a complexed state. The electrode reactions are given in equations *22* and *23*.

Positive electrode:

$$Br_2 + 2e^- \underset{\text{Charge}}{\overset{\text{Discharge}}{\rightleftharpoons}} 2Br^- \qquad E^0 = +1.07\ V \qquad (22)$$

Negative electrode:

$$Zn \underset{\text{Charge}}{\overset{\text{Discharge}}{\rightleftharpoons}} Zn^{2+} + 2e^- \qquad E^0 = -0.76\ V \qquad (23)$$

♦ *Zinc-Cerium*: A similar system to the zinc-bromine, the zinc-cerium battery operates with the same negative electrode couple (equation *23*). However at the positive electrode Ce^{3+} is oxidised to Ce^{4+} during charge and visa versa Ce^{4+} is reduced to Ce^{3+} during discharge, as shown in equation *24*.

$$2Ce^{4+} + 2e^- \underset{\text{Charge}}{\overset{\text{Discharge}}{\rightleftharpoons}} 2Ce^{3+} \qquad E^0 = 1.72\ V \qquad (24)$$

1.3.3 Fuel Cells: The fuel cell was first suggested by Grove in 1839[37] since when a number of suitable chemical systems have been proposed and developed, most notably the PEM type of fuel cell. However, the overriding obstacle with fuel cells is finding suitable catalysts, which are not easily poisoned, for high reaction rates.[3, 38] Fuel cells generate electrical energy via a chemical reaction between an oxidising and a reducing active material. The reactants are constantly fed into the cell and the reaction products continuously removed. To some degree, fuel cells can therefore be likened to primary batteries which are continuously refuelled and in principle the fuel cell may be run indefinitely. Large scale application of fuel cells was proposed by Ostwald in 1894[39] but technological difficulties have prevented widespread use so far.

The best known example of fuel cell technology is the oxygen-hydrogen fuel cell. Hydrogen has very high energy density and its combustion in oxygen is environmentally

benign, producing water as the only reaction product. The electrode reactions are given in equations *25* and *26*. At the positive electrode (anode), hydrogen is oxidised with the release of two electrons. The H^+ ions migrate to the negative electrode (cathode), where they combine with oxygen to produce water.

Positive electrode:

$$H_2 \rightarrow 2H^+ + 2e^- \qquad E^0 = 0.0\ V \qquad (25)$$

Negative electrode:

$$\tfrac{1}{2}O_2 + 2H^+ + 2e^- \rightarrow H_2O \qquad E^0 + 1.23\ V \qquad (26)$$

The development of fuel cells has spawned a technology for the efficient supply of gaseous reactants to dispersed catalyst surfaces, i.e. gas diffusion electrodes.

1.3.4 Properties Sought / Factors Determining Methods Used: Obviously, the choice of an energy storage system is determined by many factors including financial, technological and, in some cases, political issues. However, in general any decision will take into account the following considerations:

♦ *Cost*: The cost of constructing and operating the system must be offset by the operational lifetime to justify using the system.

♦ *Efficiency*: Linked to operational costs, the more efficient an energy storage system, the more profitable it is to run.

♦ *Capacity*: Any energy storage system must be capable of storing a sufficient quantity of energy to meet day to day and seasonal usage requirements and ideally be flexible enough to cover any future increase in operation.

♦ *Location*: Geographical features should be taken account of, e.g. for pumped hydro.

♦ *Start-up Speed*: Voltage and frequency smoothing as well as responding to peaks in electricity demand requires the ability to switch rapidly from charging to discharging to open circuit is essential.

Focusing specifically on the use of batteries to store energy, the following factors must be considered in addition:

♦ *Voltage*: A very negative value for the Gibbs free energy for the battery reaction, to give a substantial voltage and having a sustained voltage plateau over the majority of battery discharge is desirable.

♦ *Unwanted Reactions*: No competing electrode reactions or homogeneous reactions leading to loss of reagents.

♦ *Cycling*: After a charge/discharge cycle, the electrodes and electrolytes should be returned to their initial conditions.

♦ *Cell Resistance*: Lowering the cell resistance decreases the ohmic losses of the system and increases the efficiency.

♦ *Power*: High reactant availability to discharge at a high rate for short periods or a low rate for extended periods.

♦ *Materials*: The materials used should have a long lifetime to reduce servicing of the cells. One remit for using energy storage systems is to reduce emissions and therefore a load levelling device would preferably be manufactured using environmentally benign materials and chemicals.

1.4 Electrochemistry of Aqueous Lead Solutions

1.4.1 General Overview: The properties of lead and its ions are well known[40] and its solubility in aqueous alkali and acidic solutions, along with some aprotic solvents, is widely documented.[26, 41, 42] In the context of this project, it is the aqueous acidic solutions that are of most interest.

Lead Salt	Solubility[42] /mol dm^{-3}
$Pb(NO_3)_2$	1.01
$Pb(ClO_4)_2$	5.57
$PbSiF_6$	1.97
$Pb(CH_3COO)_2$	0.94
$PbCl_2$	0.03
$PbSO_4$	1.3×10^{-4}
$Pb(CH_3SO_3)_2$	1.36
$Pb(NH_2SO_3)_2$	1.78

Table 1.1: *Table of solubilities for lead salts in aqueous solution.*

In general, the salts of many univalent anions have some solubility, but in chloride and sulfate, the lead(II) is insoluble. Table 1.1 presents solubility data for a selection of lead salts reported by Jordan.[42] The solubility value quoted for the lead methanesulfonate salt is lower than reported by Gernon (3.8 mol dm^{-3}).[43] A solubility for this salt of circa 2.3 mol dm^{-3} was measured during this project.

It has been found that the characteristics of Pb and PbO_2 deposits may be altered by the use of additives in the electrolyte solution. Typically, additives for Pb deposition are used to produce compact, dendrite free layers while additives for PbO_2 deposition are used to improve the conductivity of the PbO_2 and perhaps the kinetics of the interconversion between solid Pb^{4+} and aqueous Pb^{2+} species during discharge / charge.

Additives are considered further in chapter 6.

1.4.2 Pb^{2+}/Pb Couple in Acid Solution: Lead has a high hydrogen overpotential and is readily electrodeposited from acidic media.[42] Indeed the electroplating of lead and lead alloys is a considerable industry. The main industrially used plating baths are:[42]

- *Perchlorate*
- *Amidosulphate*
- *Hexafluorsilicate*
- *Tetrafluoroborate*
- *Methanesulfonate*

The electrodeposition of Pb metal from aqueous solution is relatively straight forward, following equation *27.*

$$Pb^{2+} + 2e^- \rightarrow Pb \qquad E^0 = -0.12\ V \qquad (27)$$

1.4.3 Pb^{2+}/PbO_2 Couple in Acid Solution: In acid solution, the oxidation of Pb^{2+} leads to Pb^{4+} and in many media this is plated out as insoluble PbO_2 as shown by equation *28.* Stable PbO_2 (typically the β-PbO_2 modification) deposits are readily deposited from high Pb(II) containing acid solutions.[41, 43-52] Electrodeposition of stable β-PbO_2 layers have been reported for various substrates[46-52] with preference for gold, indeed one paper recommends applying a gold undercoat onto the base electrode to improve the stability of the PbO_2 layer.[52] High rate electrodeposition of β-PbO_2 in nitric acid with current efficiency close to 100 % has been demonstrated in two recent papers.[53, 54]

$$Pb^{2+} + 2H_2O \rightarrow PbO_2 + 4H^+ + 2e^- \qquad E^0 = +1.46\ V \qquad (28)$$

The application of PbO_2 as the active material in lead-acid batteries and as electrodes suitable for reactions such as waste water treatment, ozone generation electrosynthesis and the electrowinning of metals[55and references therein] has led to a large amount of literature being produced on the mechanism for the nucleation and growth of PbO_2 deposits from acidic solutions onto a variety of substrates including gold, platinum, titanium and vitreous carbon.[41, 43, 53-72] The electrodeposition of PbO_2 from acid electrolytes is inherently a more complex reaction than the electrodeposition of Pb metal. There has been some conjecture[73, 74] over the mechanism of PbO_2 deposition, Fleischmann and Liler[72] proposed a mechanism for the nucleation of PbO_2, involving adsorbed $Pb(OH)_2^{2+}$, evidence has been presented that the reaction more likely proceeds via a soluble Pb^{3+} species. A widely accepted mechanism has been suggested by Velichenko.[62, 75]

1.5 Project Overview

1.5.1 Battery Concept: A novel lead-acid flow battery for large scale energy storage is proposed, based on Pb^{2+} in aqueous methanesulfonic acid, CH_3SO_3H. The electrode reactions are given in equations *29* to *31*. The system would be based on a bipolar electrode stack with an external electrolyte reservoir. The battery would differ from conventional lead-acid batteries as lead is highly soluble in methanesulfonic acid.[42, 76] It also differs from all flow batteries as it requires only one electrolyte, reducing significantly the quantity of pipe work needed and also removing the need for expensive membrane materials to separate positive and negative electrolytes. It also negates any problems associated with the unwanted transport of species through the membrane. Figure 1.6 shows a schematic diagram of the battery layout and bipolar arrangement of electrodes, clearly demonstrating the simplification compared with conventional flow batteries, c.f. figures 1.4 and 1.5.

Methanesulfonic acid also has the advantage that it is environmentally benign[43] indeed it has been implicated as a natural product in the sulfur cycle.[77]

Having a soluble lead source reduces the complexities associated with traditional lead-acid batteries, where charging and discharging involves the interconversion of two solid phase lead compounds.

Lead-acid batteries where the lead is present in the solution phase have been suggested previously. Primary batteries with a perchloric acid electrolyte have been patented,[78-80] however these are predominantly designed as dry reserve batteries where the acid is introduced into the cell immediately before use. These batteries produce a high current density for a short period of time and are only intended for small scale emergency operations, returning a low efficiency. A number of additional patents[81-84] have described small box/button cells with electrolytes based on perchloric acid, hexafluorosilicic acid and tetrafluoroboric acid. These have been reviewed in a book chapter.[41]

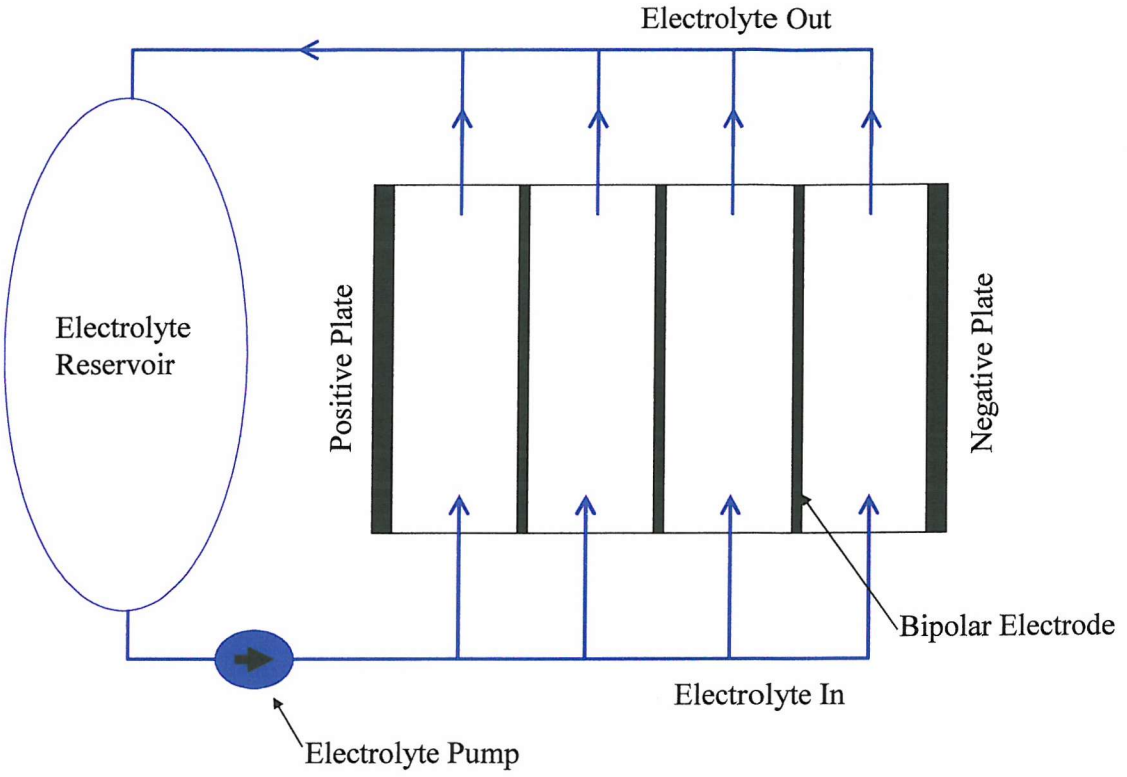

Figure 1.6: *Diagram of flow battery based on a bipolar stack electrode arrangement and using only a single electrolyte.*

1.5.2 Chemistry: The battery would operate via the electrode reactions presented in equations *29* to *31*. During charge, solid Pb layers would be deposited on the negative electrode and PbO_2 deposited on the positive electrode. During discharge the Pb and PbO_2 deposits would be respectively oxidised and reduced back to Pb^{2+} ions and re-dissolved into the electrolyte solution.

Positive electrode:

$$PbO_2 + 4H^+ + 2e^- \underset{\text{Charge}}{\overset{\text{Discharge}}{\rightleftharpoons}} Pb^{2+} + H_2O \qquad (29)$$

Negative electrode:

$$Pb \underset{\text{Charge}}{\overset{\text{Discharge}}{\rightleftharpoons}} Pb^{2+} + 2e^{-} \qquad (30)$$

Overall battery reaction:

$$Pb + PbO_2 + 4H^{+} \underset{\text{Charge}}{\overset{\text{Discharge}}{\rightleftharpoons}} 2Pb^{2+} + 2H_2O \qquad (31)$$

1.5.4 Project Outline: Following preliminary investigations,[76, 85] this thesis describes the characterisation of the Pb^{2+}/Pb and Pb^{2+}/PbO_2 electrode couples in aqueous methanesulfonic acid. A model flow cell is constructed and performance tested, showing the concept of a lead-acid flow battery based on the proposed chemistry is viable. Further flow cell investigations are carried out and the use of electrolyte additives to improve electrode deposits and improve conductivity of the PbO_2 layers are performed.

Chapter 2: Experimental

2.1 Reagents: Preparation of Chemicals, Solutions and Gases

2.1.1 General: All reagents, presented in table 2.1, were used as received from the manufacturers without further purification. All solutions were prepared with water obtained from a Whatman Analyst water purifier and unless otherwise stated were thoroughly de-oxygenated with a vigorous stream of nitrogen bubbles before experiments.

Chemical	Supplier	Purity / %
Lead carbonate: $PbCO_3$	BDH Laboratory Supplies	99
Methanesulfonic acid: CH_3SO_3H	Aldrich	99.5+
Sodium nitrate: $NaNO_3$	Fisons Scientific Equipment	99.5+
Sodium ligninsulfonate	Aldrich	-
Lead nitrate: $Pb(NO_3)_2$	BDH Laboratory Supplies	99.5+
Polyethyleneglycol (200)	Lancaster Synthesis Ltd	-
Potassium hexacyanoferrate(II) 3-hydrate: $K_4Fe(CN)_6.3H_2O$	BDH Laboratory Supplies	99.0
Potassium hexacyanoferrate(III): $K_3Fe(CN)_6$	FSA Laboratory Supplies	98
Nickel carbonate: $NiCO_3.2Ni(OH)_2.4H_2O$	BDH Laboratory Supplies	38 – 46[a]
Sodium sulfide: $Na_2S.xH_2O$	Timstar Laboratory Suppliers	30[b]
Sodium hydroxide: NaOH	BDH Laboratory Supplies	97.5
Nitrogen (Oxygen free): N_2	BOC Gases	99.99
Oxygen: O_2	BOC Gases	-

Table 2.1: *List of chemicals the used during the project, their supplier and purity.* [a] *Percentage of Ni, by weight.* [b] *Minimum percentage, by weight, of Na_2S.*

2.1.2 Lead Solutions: Lead methanesulfonate, $Pb(CH_3SO_3)_2$, was prepared in situ as an aqueous solution, via the reaction of lead carbonate with methanesulfonic acid (equation *32*).

$$PbCO_3(s) + 2CH_3SO_3H(aq) \rightarrow Pb(CH_3SO_3)_2(aq) + CO_2(g) + H_2O(l) \qquad (32)$$

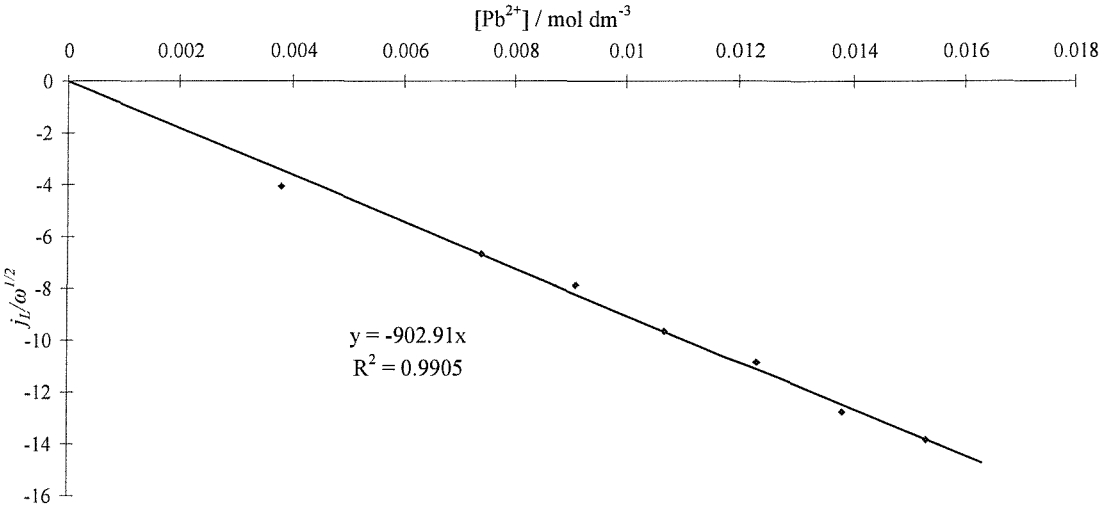

Figure 2.1: *Calibration curve showing* $\frac{j_L}{\omega^{\frac{1}{2}}}$ *vs.* $[Pb^{2+}]$. *Experiments performed at a VC carbon RDE (area 0.08 cm²) at 298 K.*

In general, the concentration of lead ions, $[Pb^{2+}]$, in a solution was calculated from the quantity of $PbCO_3$ consumed in its manufacture. However, when required for quantitative calculations, the concentration was determined by voltammetry, performed at a vitreous carbon rotating disc electrode, RDE. For solutions of unknown Pb^{2+} concentration, after dilution the limiting current density, j_L, was measured as a function of rotation rate and a graph of j_L vs. square root of rotation rate, $\omega^{1/2}$, was prepared. These plots were

linear, passing through the origin and their gradients, $\frac{j_L}{\omega^{\frac{1}{2}}}$, were compared to a calibration plot (figure 2.1) to determine the [Pb^{2+}]. To produce the calibration plot, aqueous solutions were prepared with known quantities of Analar $Pb(NO)_3$ in 1 mol dm^{-3} $NaNO_3$. With each of these solutions the limiting current density was measured as a function of rotation rate and graphs of j_L vs. $\omega^{1/2}$ were produced. The gradients of these plots ($\frac{j_L}{\omega^{\frac{1}{2}}}$) were then plotted against the [Pb^{2+}] to give the calibration plot, see figure 2.1.

Disposal of lead containing solutions was achieved using the following procedure: Solutions were adjusted to pH 6 (with NaOH) and the Pb^{2+} reacted with sodium sulphide. The resulting lead sulfide precipitate was separated from the liquid phase by filtration, dried and collected and the solid sent for disposal. The remaining, lead free solution was disposed of via the drain with excess water.

2.2 Flow Cell

2.2.1 Design: The cell design is shown in figure 2.2. It consists of two, identical polypropylene plates with dimensions 100 mm × 40 mm × 12 mm. In each of the plates was recessed a 20 mm × 20 mm × 3 mm deep pit to hold the electrodes so that the front surface of the carbon powder/polymer composite plate was plush with the surface of the polypropylene. Two holes towards the top and bottom of the polypropylene plates acted as entries and exits for the electrolyte. The interelectrode gap was controlled with a polypropylene spacer and/or thin Viton gaskets; within each was machined a 10 mm × 80 mm channel which formed the flow compartment for the electrolyte. Two thicknesses of flow compartment, 4 mm and 16 mm, were used. The cell was held together with a small clamp consisting of two metal plates and four bolts that allowed rapid dismantling and reconstruction of the cell.

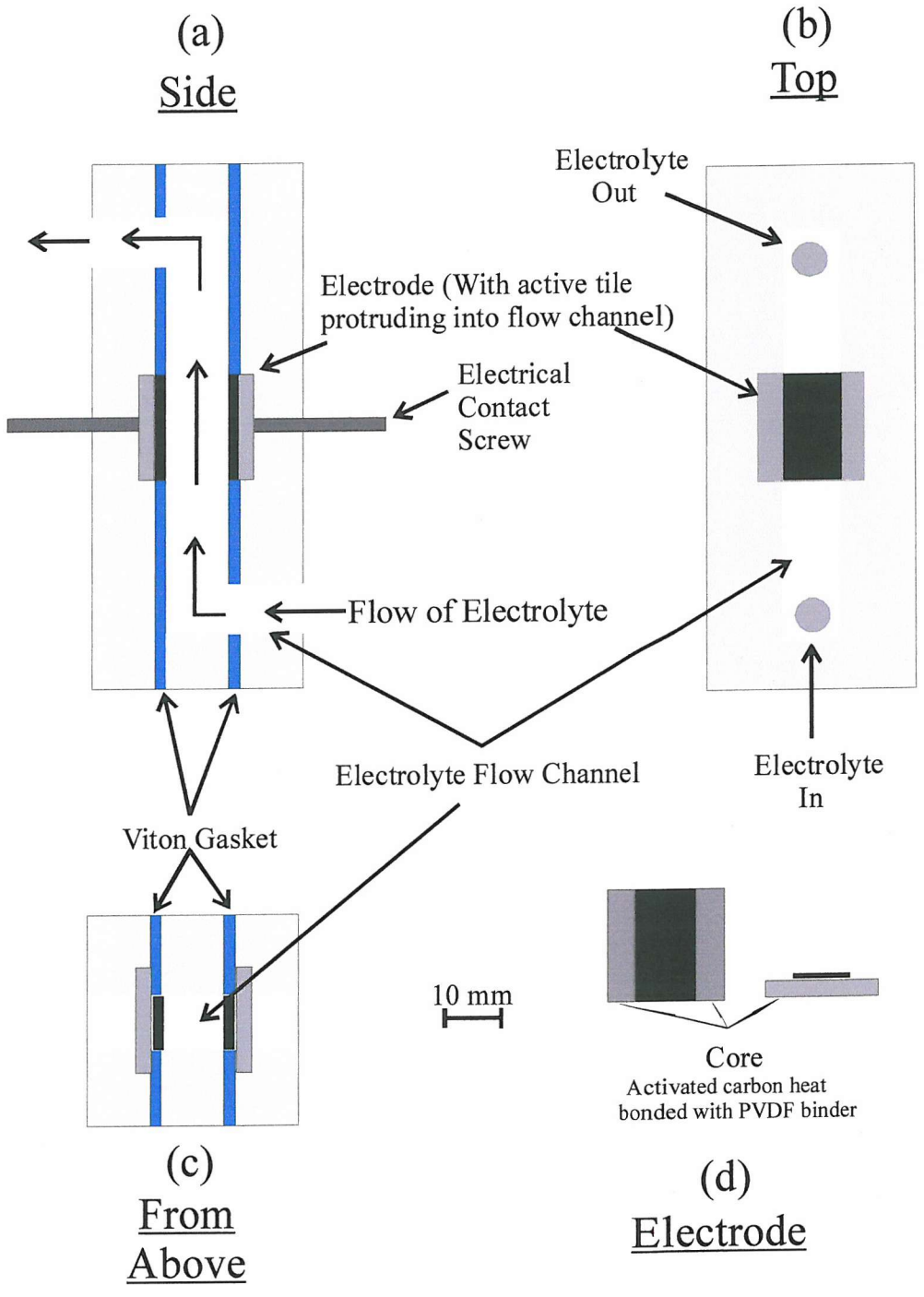

Figure2.2: (a), (b) and (c) are views of the cell side, front and from above. (d) shows the design of the electrodes.

Figure 2.3: *Photographs showing (A) flow cell components and (B) assembled flow cell system. 1: Cell clamp, 2: Flow compartment plates, 3: Gasket and interelectrode spacer, 4: Type II electrode, 5: Type III electrode, 6: assembled flow cell, 7: Peristaltic pump and pump head, 8: Pump controller, 9: Potentiaostat / Galvanostat, 10: Electrolyte reservoir, 11: Thermostated water bath.*

2.2.2 Electrolyte flow circuit: The electrolyte flow circuit consisted of a reservoir (maximum capacity 100 cm^3) placed in a water thermostat, the cell and a Masterflex Model 7553-79 pump fitted with a Masterflex pump head, Type 70-16-20, interconnected with Masterflex 6412-16 Viton tubing. The tubing was connected to the cell entries and exits with SwageLok PTFE connectors.

Figure 2.3 shows photographs of the flow cell components and assembled flow cell system. Unless otherwise stated each experiment was commenced with a new set of electrodes and the system configured such that a mean linear flow rate between 2 cm s^{-1} and 10 cm s^{-1} was achieved across the face of the electrodes, the reservoir was maintained at 298 K by immersion in a thermostated water bath and contained 40 cm^3 of electrolyte. The flow circuit was deliberately designed to operate with small electrolyte volumes in order to minimise the cost of chemicals and the volumes of Pb^{2+} containing solutions to be disposed of.

Type	Electrode	Description
I	Core	Carbon powder / polymer composite plate of thickness 3.2 mm, with no active layer
II	Ni	Core plate onto which nickel foam (40 ppi, initial thickness 1.8 mm) is heat bonded at a temperature of 433 K and pressure of circa 6 kg cm^{-2}.
III	RVC	Core plate onto which an active tile of reticulated vitreous carbon (70 ppi, initial thickness 1.5 mm) is heat bonded using a temperature of 433 K and pressure of 6 kg cm^{-2}.
IV	Scraped RVC	As above but with the protruding RVC structure scraped off with a sharp blade.
V	Carbon 500	"S" Series Regenesys commercial electrode, with tile comprised of; activated carbon particles heat bonded with PVDF binder. Tile fused to core using a pressure of 29 kg cm^{-2}.
VI	Carbon 4500	As above, but tile fused to core using a pressure of 261 kg cm^{-2}.
VII	Cloth	Woven carbon fibre cloth, fused to core using a pressure of circa 6 kg cm^{-2} and a temperature of 433 K over a 2 s period.
VIII	AC 7	As type V and VI but with activated carbon particles without polymer.

Table 2.2: Table relating electrode type and active material to specific fabrication details.

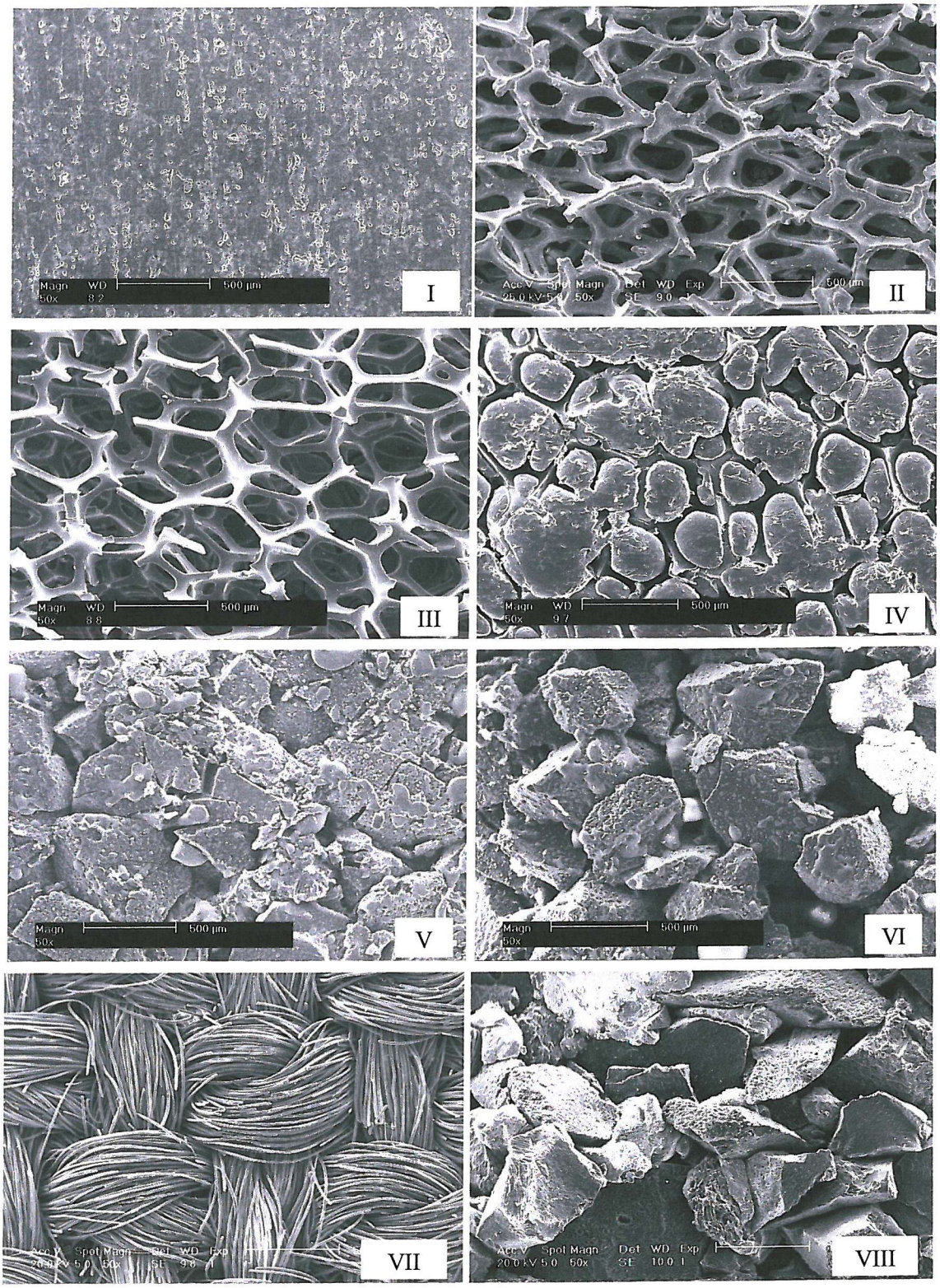

Figure 2.4: *SEM images, taken of the various electrodes used: (I) Core, (II) pressed Ni foam, (III) Pressed RVC, (IV) Scraped Pressed RVC, (V) Carbon 4500, (VI) Carbon 500, (VII) Cloth, and (VIII) AC 7. The distance bar represents a measurement of 500 μm in all of the photographs.*

2.2.3 Electrodes: The flow cell was based on electrodes with an operational area of 10 mm × 20 mm. These electrodes consisted of a carbon powder/polymer composite plate (the core), 20 mm × 20 mm × 3 mm, with an active layer (the tile) on the surface produced by heat bonding, under pressure a material onto the core. On each side of the plate, 5 mm of active material was scraped away to leave an effective electrode area of 10 mm × 20 mm at the centre. The bare edges produced fitted under the cell gasket (see section 2.2.2) so that they were not exposed to the electrolyte solution. This was also an effective means of securing the electrodes into the cell. A layer of PTFE tape was wrapped around the edge of the electrodes to give a snug fit into the recess and also to provide extra protection against electrolyte leaking to the rear of the electrodes. In this project, electrodes with various active layers were used. These are presented in table 2.2.

Scanning electron microscope images of the electrodes are shown in figure 2.4. Image (I) is that of the carbon / polymer composite core electrode. On the scale shown the surface appears smooth and uniform. Images (II) and (III) show the pressed nickel foam and reticulated vitreous carbon electrodes respectively. It is clear that both have retained their structure, although some strands have been broken by the pressures used to fuse the active layers to the core. Photograph (IV) is that of the scraped reticulated vitreous carbon electrode. It can be seen that embedded within the carbon / polymer plate remain fragments of RVC, giving a substantially rougher surface than the core itself. Images (V) and (VI) show the carbon 4500 and carbon 500 electrodes respectively. These are prepared by pressing a carbon powder / polymer mixture into the core. The granular structure of the active tile on each of the electrodes is clearly visible. The higher pressure used in manufacturing the carbon 4500 electrode results in a smoother, more compact surface having less cavities running through it. However both the 4500 and 500 electrode active tiles are made up from interconnecting 200-300 μm carbon / polymer composite particles. Type VII electrodes were produced by bonding a woven carbon cloth onto the core plate. Type VIII electrodes are similar to types V and VI but the active tile is made up of activated carbon particles bonded to the core plate.

With all these electrodes, it was found that the resistance on the carbon / polymer composite plate was not negligible if current had to pass along the plate and it proved

essential to provide uniform electrical contact across the back of the electrodes. Electrical contact was achieved in the following ways, listed in order of improving effectiveness:

♦ *Method A*: A screw (diameter 3 mm) was tightened into the back of the electrode once the cell was assembled. Electrical contact being maintained by the pressure exerted from the electrode (held in place by the cell gasket).

♦ *Method B*: As with *method A* but with the addition of a platinum gauze, inserted between the back of the electrode and the screw, thus improving current distribution across the back of the electrode.

♦ *Method C*: An electrical wire with fine wire core (16 strands) was stripped of insulation (10 mm) at one end. The wire strands were then untwisted and separated. These were then distributed evenly over the back of the electrode and merged into the carbon / polymer composite plate by melting the core surface with a soldering iron. The reverse of the electrode was then sealed with epoxy resin to add strength and prevent the wire strands coming into contact with any electrolyte solution that may seep around the gasket seals.

The third method proved to be the most successful and gave reproducible results with a lowered *IR* drop associated with the electrode.

2.2.4 Pump Calibration: In order to determine the flow rate of electrolyte across the electrodes within the flow cell, a calibration curve relating the pump setting to volumetric flow rate was produced. At each of the numerical points marked on the pump control, 1 through 10, the time taken to displace a known volume (250 cm^3) of water was recorded. For each setting, several readings were taken and an average calculated. The volume, in cubic centimetres per second, was then calculated and plotted against the numerical pump setting, see figure 2.5. Volumetric flow rate, Q_V, through the circuit was subsequently taken from the trendline of this plot and the linear flow rate, v_L, across the surface of the electrodes calculated using equation *33*, where; A_{cell} is the cross sectional area of the flow compartment.

$$v_L = \frac{Qv}{A_{Cell}} \qquad (33)$$

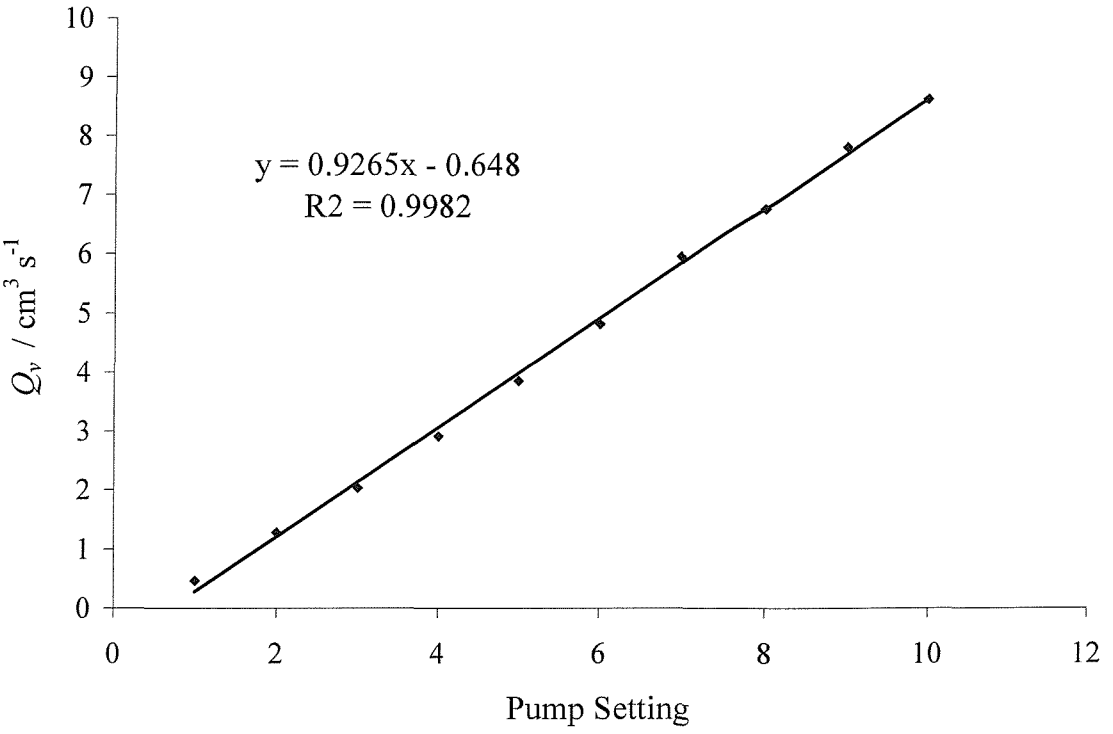

Figure 2.5: *Pump Calibration curve.*

2.2.5: Current density and Mass Transport to Electrodes within the Flow Cell: The rate of mass transport of the lead ions within the electrolyte, to the electrode surfaces was anticipated to be most important during high rates of charge and low Pb^{2+} concentrations. The relationship between limiting current and rate of mass transport for two dimensional electrodes (e.g. Type I) is given by equation *34*,[86] where; I_L is the limiting current, n the number of electrons transferred per molecule of reactant, F the Faraday constant, k_m the mass transport coefficient, A the specific geometric area of the electrode and c is the concentration of reactant.

$$I_L = nFk_mAc \qquad (34)$$

With three dimensional electrodes (e.g. Type II) it is not possible to easily distinguish the influence of the electrode structure on the mass transport coefficient from the differences in the real surface area of the material/solution interface. In dealing with

these three dimensional electrodes, the area of the electrode is expressed by equation *35*, where; A_e is the active surface area per unit volume of the electrode and V_e is the volume of the three dimensional electrode. Hence, the limiting current for three dimensional electrodes is given by equation *36*.[86]

$$A = A_e V_e \qquad (35)$$

$$I_L = nFk_m A_e V_e c \qquad (36)$$

Throughout this thesis, where current density, j, is referred to, it is calculated using the planar geometric area of the electrodes, A, i.e. 2 cm^2 for the flow cell electrodes. On this basis the mass transport coefficient may be expressed in terms of the limiting current density, j_L, and this gives (by rearrangement of equations *35* and *36*) equation 37 for two dimensional electrodes and equation *38* for three dimensional electrodes, where j_L is measured in A cm^{-2}.

$$j_L = nFk_m c \qquad (37)$$

$$j_L = \frac{nFk_m A_e V_e c}{2} \qquad (38)$$

From a solution containing 1 mmol dm^{-3} ferrocyanide and 10 mmol dm^{-3} ferricyanide, j_L was measured at linear flow rates, v, between 1 and 15 cm s^{-1}. Figure 2.5 shows plots of j_L vs. v, on a logarithmic scale, for the core plate electrode (type I), pressed RVC electrode (type III) and scraped pressed RVC electrode (type IV). Using the smooth core plate as the electrode the current densities are of the order of 0.1 mA cm^{-2} (equivalent to a mass transfer coefficient of 5×10^{-4} cm s^{-1}) and there is a small increase with an increase of flow rate over the range 1 – 15 cm s^{-1}. With the very rough surface of the type IV electrodes, the current densities are increased by a factor up to four and the dependence on flow rate increases; these result from the turbulence introduced by the embedded RVC fragments. With the type III electrodes, the current densities are greater than 10 times

higher than at the flat, type I electrodes. This arises from enhancements in both the mass transfer coefficient and the electrode surface area. Applying equation *36* values for $k_m A_e$ in the range of 0.03 – 0.14 $cm^3\ s^{-1}$ are obtained in the flow rate range used. These are similar to values reported previously for RVC electrodes in flow cells.[87-89]

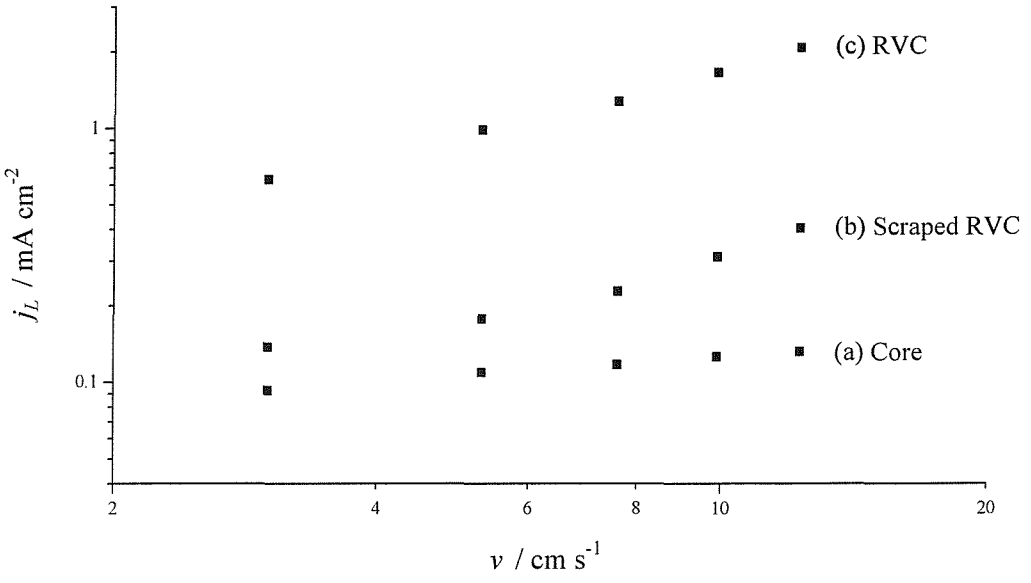

Figure 2.5: *Limiting current density, j_L, as a function of the mean linear flow rate of the electrolyte, v. Cell with (a) a flat plate carbon electrode (b) a scraped reticulated vitreous carbon electrode (c) a reticulated vitreous carbon electrode. Data for the oxidation of ferrocyanide. Solution: 10^{-3} mol dm^{-3} $K_4Fe(CN)_6$ and 10^{-2} mol dm^{-3} $K_3Fe(CN)_6$.*

2.3 Rotating Disc Electrodes

The majority of experiments using rotating discs were carried out with two vitreous carbon disc electrodes (areas 0.08 cm^2 and 0.13 cm^2) but a few used a nickel disc (area 0.32 cm^2) or a gold disc (area 0.20 cm^2). Each of these discs was mounted in a PTFE shroud. The discs' rotation rates were controlled with an EG&G Model 616 RDE unit. Before each experiment, the RDE's were polished with alumina powder slurries (1 μm, then 0.3 μm,

and finally 0.05 μm) on a polishing cloth (Beuhler), wiped with a clean cloth and thoroughly rinsed with purified water after each polish.

2.4 Voltammetry

2.4.1 At a rotating disc electrode (RDE): Unless otherwise stated, all solutions were thoroughly de-oxygenated with a vigorous stream of nitrogen gas before voltammograms were recorded. Voltammetric measurements were performed and data recorded using one of three equivalent sets of apparatus:

♦ A HiTek Instruments PPR1 waveform generator coupled to a HiTek Instruments type DT2101 potentiostat. Results were recorded with the use of a Gould Series 60000 chart recorder.

♦ An laboratory constructed potentiostat controlled by a PC operating with a National Instruments LabVIEW^{TM} 5.1 interface card and in house data acquisition software.

♦ A model 263A EG&G combined potentiostat / galvanostat coupled to a PC with a National Instruments MC-GPIB interface card. The potentiostat was controlled and data collected using EG&G M270 electrochemistry software.

The voltammetry was carried out in a two compartment, glass cell (See figure 2.6) with a volume ~ 20 cm^3 immersed in a Camlab W14 water thermostat. The working electrode, WE, was rotated using an EG&G PARC model 616 RDE rotating platform. A looped, platinum wire formed the counter electrode, CE. The WE and CE were separated from the saturated calomel reference electrode, SCE, by a Luggin capillary. The tip of the Luggin capillary was placed ~ 1 mm from the surface of the WE disc. The cell was designed with a fine glass sinter to allow the efficient entry of gases into the electrolyte solutions.

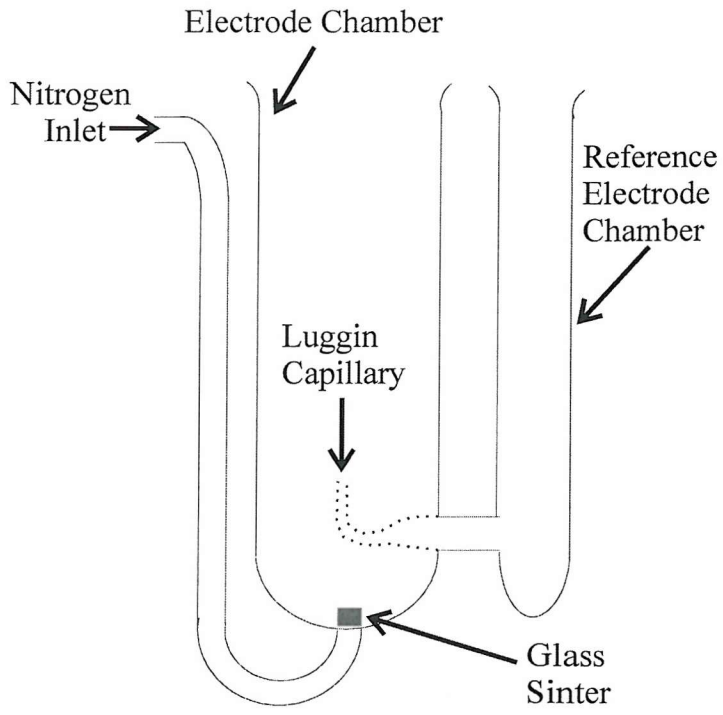

Figure 2.6: *Electrochemical cell.*

2.4.2 Voltammetry with electrodes of types I to VIII: Voltammetric investigations of the flow cell electrode materials were carried out using two distinct apparatus configurations:

♦ Sections of the electrode material were cut (5 mm × 15 mm), and some active material removed to leave a square measuring 5 mm × 5 mm at one end. An electrical contact was made at the opposite end to the remaining active tile and any exposed core insulated with epoxy resin to form an electrode of active tile with an area 0.25 cm^2. This electrode was then suspended in the glass cell described in section 2.4.1 and figure 2.2. Voltammograms were performed with a HiTek Instruments PPR1 waveform generator coupled to a HiTek Instruments type DT2101 potentiostat. Results were recorded with the use of a Gould Series 60000 chart recorder.

♦ In situ current vs. cell voltage characteristics were obtained for the electrode materials within the flow cell (See section 2.2). When assembled, the flow cell forms a two electrode electrochemical cell. The experiments were performed with a model 263A EG&G combined potentiostat / galvanostat coupled to a PC with a National Instruments MC-GPIB

interface card. The instrument was controlled and data collected using EG&G M270 electrochemistry software. Measurements obtained at electrodes mounted in the flow cell were taken without the use of a reference electrode. In some of the experiments the current was ramped and in others the potential was ramped.

2.5 Chronopotentiometry

2.5.1 At the rotating disc electrode: Constant current experiments were performed in the electrochemical cell shown in figure 2.2. A carbon RDE was used and prepared as set out in section 2.3. Experiments were performed with the use of a laboratory constructed galvanostat controlled by a PC operating with a National Instruments LabVIEW^{TM} 5.1 interface card and in-house written data acquisition software.

2.5.2 In the flow cell: Experiments were controlled via a model 263A EG&G potentiostat / galvanostat coupled to a PC with a National Instruments MC-GPIB interface card. The galvanostat was operated, and data collected, using EG&G M270 electrochemistry software.

2.6 Scanning Electron Microscope, SEM

Electrode materials as well as lead and lead dioxide deposits were examined with the use of a Phillips ESEM environmental scanning electron microscope including elemental analysis by EDAX x-ray diffraction. The microscope was operated with the sample chamber under high vacuum (chamber pressure of 10^{-5} mBar or lower) with an observational sphere of circa 5 μm diameter. An electron accelerating voltage of 25 keV

was typically used to observe Pb deposits and bare electrodes. Due to its lower conductivity and to avoid charging effects or sample damage, PbO_2 deposits were typically observed using an electron acceleration voltage of 20 keV. Samples were mounted on an adjustable stage within the microscope such that a working distance of 8 – 12 mm was established between the probe and sample surface. The majority of images were obtained perpendicular to the samples surface.

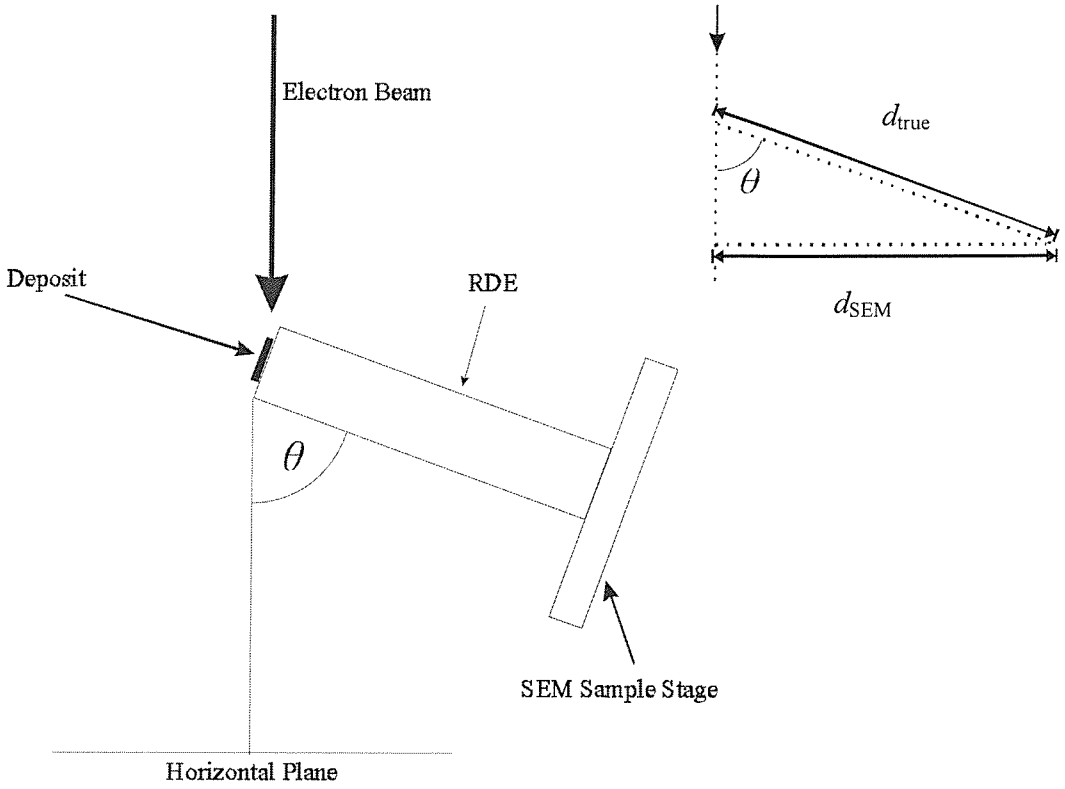

Figure 2.6: *Diagram showing the orientation of a sample within the SEM chamber compared to the incident electron beam, when the sample stage is tilted at an angle θ.*

Where deposit depth or topology was required, the sample stage was tilted to an angle of 70° from perpendicular before an image was taken, as shown in figure 2.6. For

such images the dimensions must be converted by a factor given by the simple trigonometric expression given in equation *39*:

$$d_{true} = \frac{d_{SEM}}{\sin 70} \qquad (39)$$

Where; d_{true} is the true distance value required and d_{SEM} is the measured value obtained form the SEM image.

2.7 AC Impedance

Determination of the resistance, R, of the electrolyte solutions was carried out with a Hewlet Packard 4192A LF impedance analyser coupled to a PC using in house software. Measurements were performed in a single compartment glass cell (capacity ~ 5 cm^3) with two platinum electrodes (areas 0.004 cm^2) spaced by 1 cm. Experiments were carried out at 293 K. Solution conductivities were calculated by substituting the measured resistance into equation *40*. Where; κ = electrolyte conductivity (Ω^{-1} cm^{-1}), l = electrode separation (cm) and A = electrode area (cm^2).

$$R = \kappa\left(\frac{l}{A}\right) \qquad (40)$$

An accurate value for the cell constant, l/A, was determined by measuring the cell resistance when it was filled with aqueous potassium chloride (1 mol dm^{-3}). This has a known conductivity of 0.102 Ω^{-1} cm^{-1} at 293 K.[90]

Chapter 3: Electrolyte Composition and Voltammetric Studies of the Electrode Reactions

3.1 Introduction

It was noted, in chapter 1, that the electrolyte chosen for the proposed battery contains soluble $Pb(CH_3SO_3)_2$ in aqueous CH_3SO_3H. Two properties critical to battery performance will be the solubility of the Pb^{2+} ion in the acid medium and, secondly, the conductivity of the solution. To maximise the energy storage capacity of the battery, per unit volume of electrolyte, it is desirable to have a high initial concentration of Pb^{2+} in solution. In addition, a high charge rate requires a high concentration of aqueous lead ions, $[Pb^{2+}]$. In the context of the proposed battery, it is preferable to have an electrolyte with a high conductivity to minimise resistance losses and optimise the energy efficiency during charge and discharge.

The next stage in assessing the suitability of the chosen electrolyte was the characterisation of the electrode reactions. These were individually investigated with the use of rotating disc electrodes.

3.2 Solubility of Lead Methanesulfonate

The solubility of $Pb(CH_3SO_3)_2$ was experimentally determined as a function of $[CH_3SO_3H]$ at 298 K and 333 K. Different concentrations of aqueous methanesulfonic acid (1.0 – 9.0 mol dm^{-3}) were equilibrated in a thermostat at 298 K before lead carbonate was added slowly in aliquots, allowing the reaction:

$$PbCO_3 + 2CH_3SO_3H \rightarrow (CH_3SO_3)_2Pb + CO_2 + H_2O \qquad (41)$$

Addition of $PbCO_3$ continued until no further reaction took place. This was determined by one of two outcomes:

♦ No further $PbCO_3$ solid reacted and evolution of CO_2 ceased. In this case the endpoint was taken to be the point at which solid $PbCO_3$ accumulated at the bottom of the solution.

♦ Addition of $PbCO_3$ still resulted in reaction 41, however simultaneous precipitation of $Pb(CH_3SO_3)_2$ occurred. The endpoint in this instance was taken as the point at which insoluble $Pb(CH_3SO_3)_2$ was first observed. This may lead to the final methanesulfonic acid concentration being lower than estimated, however the error is not thought to be significant.

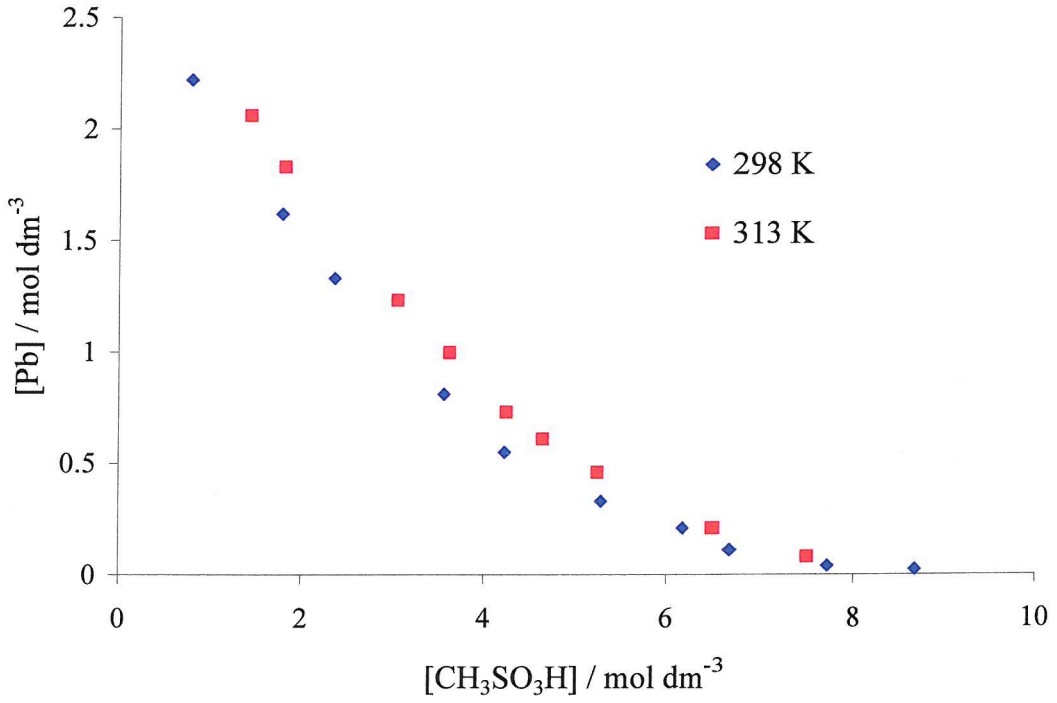

Figure 3.1: *Solubility of lead methanesulfonate as a function of methanesulfonic acid concentration, at temperatures of 298 K and 313 K.*

Once the maximum concentration of $Pb(CH_3SO_3)_2$ had been reached, a 1 cm^3 sample of the solution was taken and made up to 1 litre with 1 mol dm^{-3} aqueous $NaNO_3$. Using this diluted solution, a set of voltammograms was recorded at a vitreous carbon rotating disc electrode (area = 0.08 cm^2). Rotation rates of 400, 900 1600 and 2500 rpm were used and the electrochemical cell maintained at 298 K. The limiting current density, j_L, was plotted against the square root of rotation rate, $\omega^{1/2}$, and the lead(II) methanesulfonate concentration determined by comparing its slope to a calibration plot (Section 2.1.2, figure 2.1). The concentration of methanesulfonic acid in the solutions after Pb^{2+} saturation was simply calculated from the initial $[CH_3SO_3H]$ and $[Pb(CH_3SO_3)_2]$ according to the molar ratios implied by equation 41. The solubility of lead methanesulfonate in aqueous methanesulfonic acid is reported in figure 3.1.

It can be seen, at 298 K, that the solubility of $Pb(CH_3SO_3)_2$ tends to a maximum (~ 2.5 mol dm^{-3}) as the free acid concentration approaches zero. From this maximum the $Pb(CH_3SO_3)_2$ solubility decreases steadily with increasing acid concentration. These solubility values agree with data published by Gernon, T Buszta and P Janney[91], who quote two values of 2.6 mol dm^{-3} and 3.5 mol dm^{-3} for the maximum solubility of lead methanesulfonate in aqueous solution at 298 K.

The procedure used becomes inaccurate when a large amount of $PbCO_3$ reacts to leave a low final concentration of acid. When the final acid concentration is below 0.5 mol dm^{-3}, the calculated acid concentration is no longer accurate.

As expected, at the higher temperature of 313 K, the solubility of Pb^{2+} is slightly increased. Again, with increasing acid concentration the solubility decreases rapidly.

It should be noted that within the battery, in accordance with equation 31, the electrolyte composition varies with the state of charge. As the quantity of lead is depleted during charge, or replenished during discharge, the methanesulfonic acid concentration increases and decreases respectively. In fact, for each one mole change in $[Pb^{2+}]$ there is a two mole change in $[CH_3SO_3H]$. Hence the concentrations of lead(II) and methanesulfonic acid should be suitably chosen so that at all states of charge precipitation of lead is avoided. A suitable initial composition for room temperature operation of the battery, and the one chosen for a large number of experiments in this project, is 1.5 mol dm^{-3} $Pb(CH_3SO_3)_2$ and 0.9 mol dm^{-3} CH_3SO_3H. According to equation *42* (where n = the number of electrons

transferred per mole, F = Faraday's constant and c = lead concentration), an initial lead concentration of 1.5 mol dm^{-3} gives a maximum theoretical storage capacity of 40 Ah dm^{-3}.

$$Storage\ Capacity = 0.5nFc/3600 \qquad (42)$$

3.3 Conductivity

The conductivity of electrolyte solutions of different composition was determined with the use of a small cell, containing two platinum electrodes (as described in section 2.7), and resistance estimations from the cell impedance diagrams. Figure 3.2 reports the conductivities, at a temperature of 293 K, for these solutions. As would be expected the conductivity values rise with increasing methanesulfonic acid concentration. With increasing lead methanesulfonate concentration the conductivity decreases, possibly due to a combination of increasing solution viscosity and ion pairing of the divalent lead cation with methanesufonate anions. However the conductivity values obtained, particularly those for low $[Pb^{2+}]$, compare well with literature values.[92] For example, conductivity values for 0.9 mol dm^{-3} and 1.5 mol dm^{-3} HNO_3 are cited as 0.301 Ω^{-1} cm^{-1} and 0.401 Ω^{-1} cm^{-1} respectively, very similar to the same concentrations of methanesulfonic acid with 4 mmol dm^{-3} lead methanesulfonate.

Data presented in figure 3.2 shows that the maximum conductivity is achieved with high acid concentration and low lead concentration.

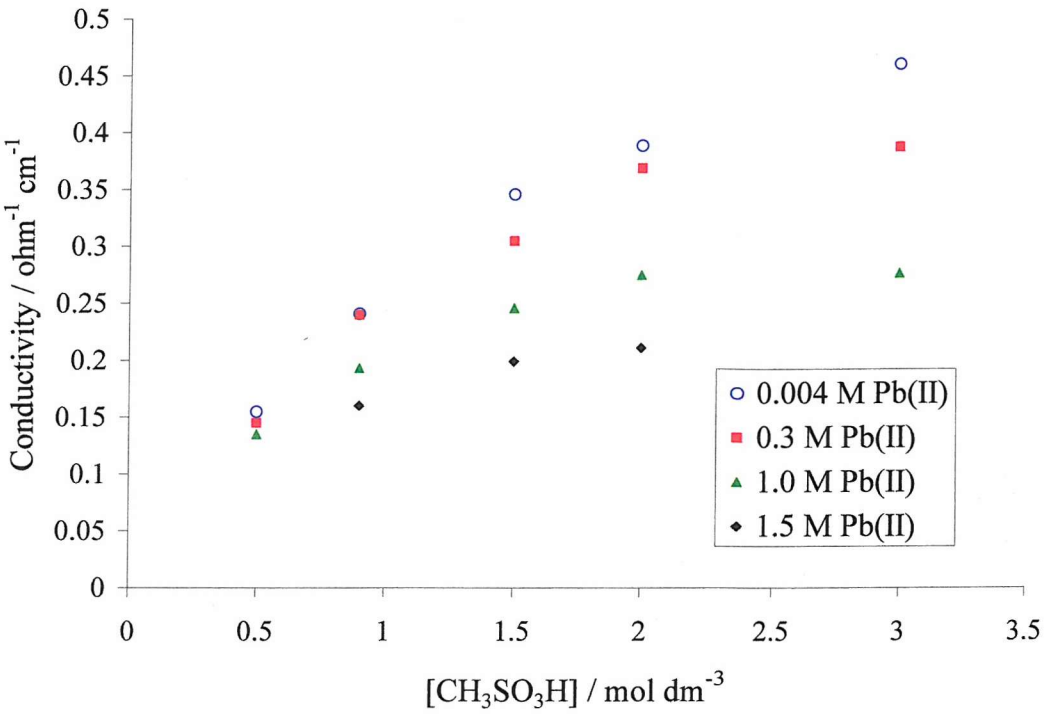

Figure 3.2: *Solution conductivities as a function of $Pb(CH_3SO_3)_2$ and CH_3SO_3H concentrations, determined with an AC impedance spectrometer. Temperature 292 K.*

3.4 Pb/Pb^{2+} Electrode Couple

3.4.1 Pb/Pb^{2+} Voltammetry: Cyclic voltammograms were taken at vitreous carbon (Figure 3.3) and nickel (Figure 3.4) rotating disc electrodes (ω = 1600 rpm), from an aqueous electrolyte solution containing $Pb(CH_3SO_3)_2$ (4 mmol dm^{-3}) and CH_3SO_3H (2.0 mol dm^{-3}). The temperature was maintained at 298 K. The potential was scanned from a starting value of -300 mV, to a final potential of -700 mV, before returning to -300 mV, using a constant scan rate of 25 mV s^{-1}. Potentials were measured against a saturated calomel reference electrode.

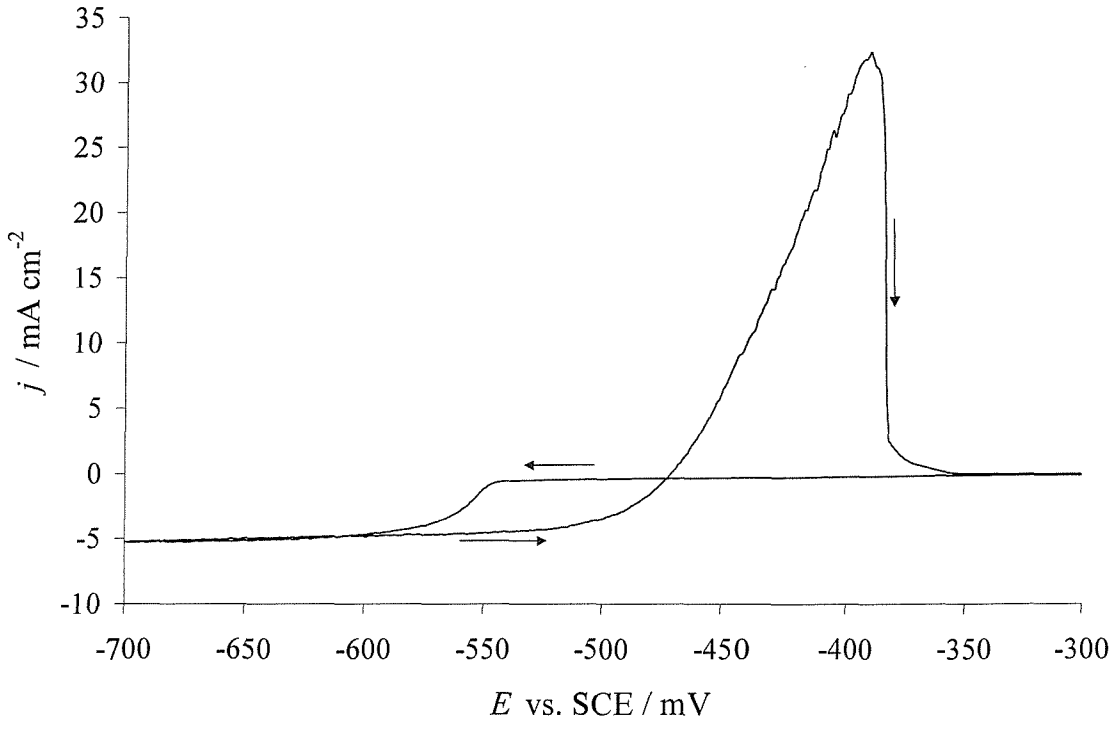

Figure 3.3: *A cyclic voltammogram recorded at a rotating vitreous carbon disc electrode (ω = 1600 rpm) in a electrolyte containing $Pb(CH_3SO_3)_2$ (4.0 mmol dm^{-3}) in aqueous CH_3SO_3H (2.0 mol dm^{-3}). Potential scan rate 25 mV s^{-1}. Temperature 298 K.*

At the vitreous carbon RDE, during the negative scan a cathodic reduction wave is observed starting at -550 mV, which corresponds to the reduction of Pb^{2+} to Pb (i.e. the deposition of metallic lead onto the RDE's surface). Following the reduction wave, a plateau region of steady current density is observed. This is typical for mass transport controlled kinetics and gives a limiting current density, j_L, of -5 mA cm^{-2}.

On the reverse scan, the deposition of lead continues to a potential more positive than the reduction wave, before a sharp anodic stripping peak commences at -475 mV vs. SCE. This is a good approximation of the formal potential for the Pb/Pb^{2+} couple (although it should be noted that the deposition / stripping of lead will slightly alter the lead ion concentration at the electrode surface and hence shift the formal potential), and the overvoltage for the nucleation of Pb, η_n, appears to be 75 mV. This overvoltage is due to the unfavourable kinetics of nucleating Pb on the clean electrode surface. The stripping

peak shows no mass transport kinetics as the lead is present as a solid deposit on the electrode surface. The steep intersection of the response through zero current on the reverse scan confirms the rapid kinetics of the Pb/Pb^{2+} couple in methanesulfonic acid.

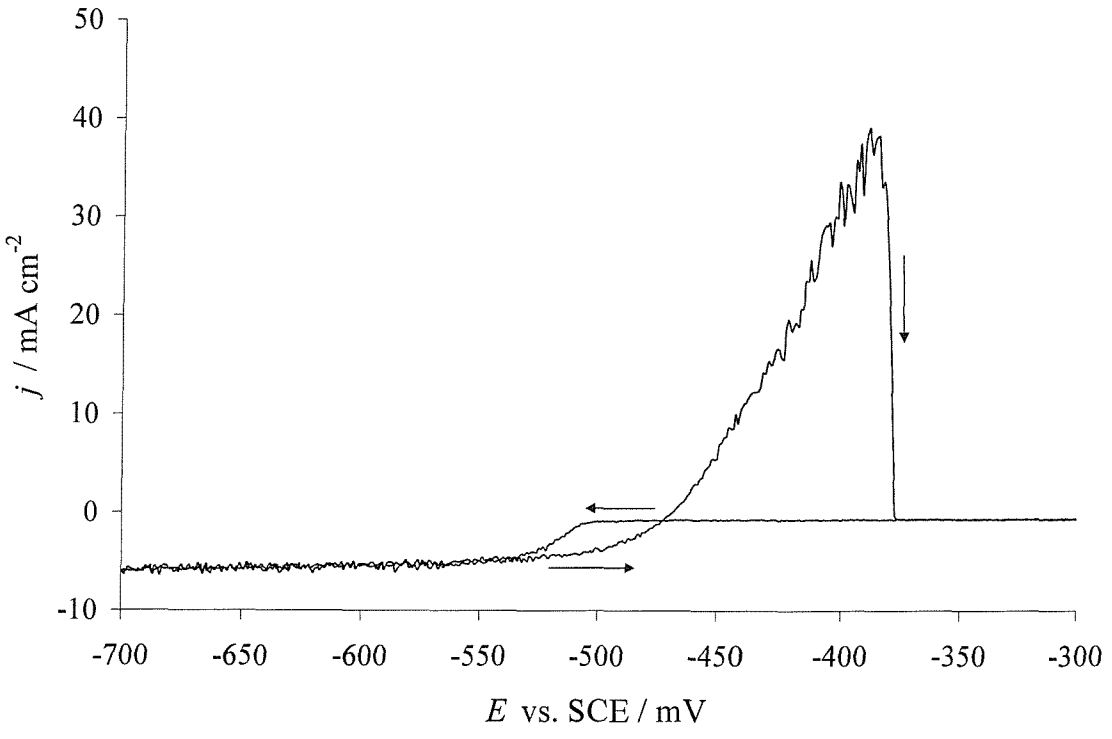

Figure 3.4: *A cyclic voltammogram recorded at a nickel rotating disc electrode (ω = 1600 rpm) in a electrolyte containing $Pb(CH_3SO_3)_2$ (4 mmol dm^{-3}) in aqueous CH_3SO_3H (2 mol dm^{-3}). Potential scan rate 25 mV s^{-1}. Temperature 298 K.*

The voltammogram obtained at the nickel RDE was essentially the same except that, during the negative sweep, deposition of lead proceeded at the more positive potential of -510 mV vs. SCE. This corresponds to an nucleation overpotential of 35 mV, which is approximately half the observed value at the vitreous carbon RDE, implying that the formation of Pb nuclei is easier at the nickel surface.

The form of the cyclic voltammograms are characteristic of metal deposition and dissolution[93] and are typical voltammograms of the Pb^{2+}/Pb couple in methanesulfonic acid[76, 85] and other acidic media.[58, 94-98]

Figure 3.5 shows voltammograms for the deposition of lead onto a vitreous carbon rotating disc electrode at various rotation rates (ω = 400, 900, 1600, 2500 and 3600 rpm). A linear potential sweep was performed, between -300 mV vs. SCE and -700 mV vs. SCE at a scan rate of 25 mV s^{-1}. As with the cyclic voltammogram (figure 3.2) each of the rotation rates produces a reduction wave, associated with the Pb^{2+}/Pb couple, which commences at circa -550 mV vs. SCE. Also evident with each of the potential scans is a clearly defined plateau limiting current density. In fact, a plot of j_L vs. $\omega^{1/2}$ gives a linear graph passing through the origin (figure 3.6), confirming that the deposition of lead becomes mass transport controlled. The Levich equation was used to obtain a diffusion coefficient, D, of 6.1×10^{-6} cm^2 s^{-1}, for Pb^{2+} in 2.0 mol dm^{-3} aqueous CH_3SO_3H.

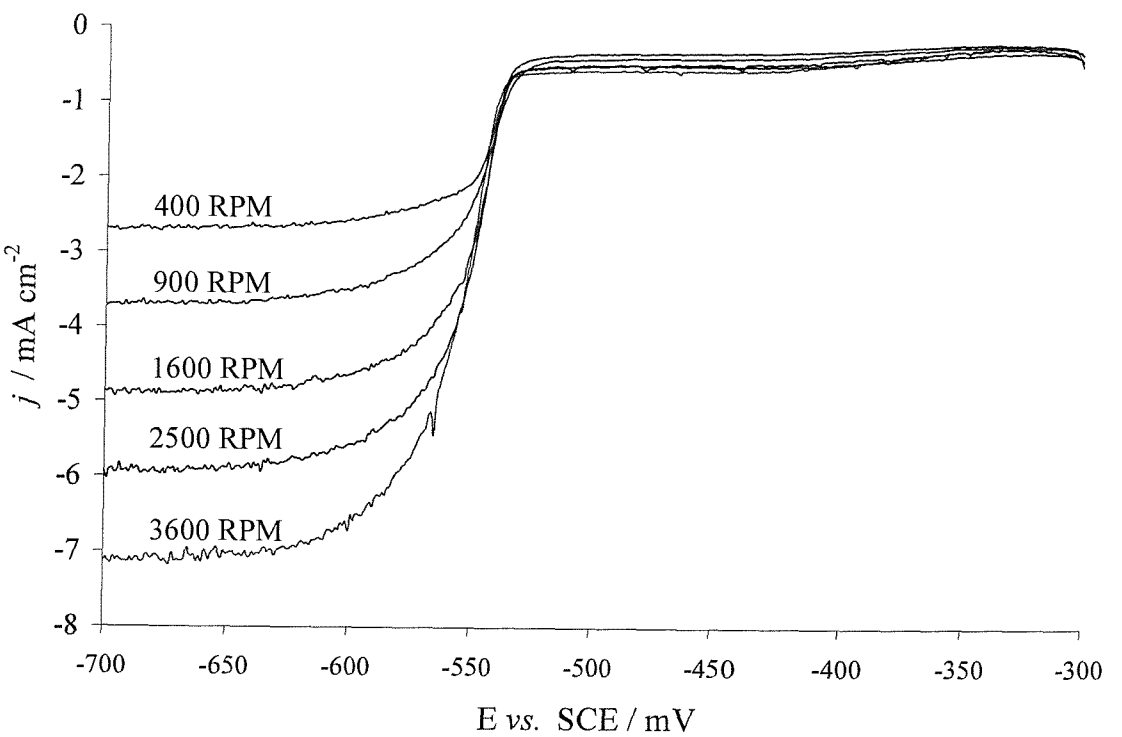

Figure 3.5: *Linear sweep voltammograms performed at a vitreous carbon rotating disc electrode (ω = 400, 900, 1600, 2500 and 3600 rpm). The electrolyte comprised of $Pb(CH_3SO_3)_2$ (4.0 mmol dm^{-3}) in aqueous CH_3SO_3H (2.0 mmol dm^{-3}). Potential scan rate 25 mV s^{-1}. Temperature 298 K.*

A number of voltammograms were recorded using electrolytes of varying composition; [$Pb(CH_3SO_3)_2$] from 4 mmol dm^{-3} to 1.5 mol dm^{-3} and [CH_3SO_3H] from 0.1 mol dm^{-3} to 5 mol dm^{-3}. The voltammograms obtained with each of the electrolytes were essentially the same as those discussed above, however with high $Pb(CH_3SO_3)_2$ concentrations a significant degree of polarisation, due to uncompensated IR drop, was observed. Consecutive cyclic voltammograms also produced similar results, with a slight lowering in the overpotential associated with nucleation of lead deposition.

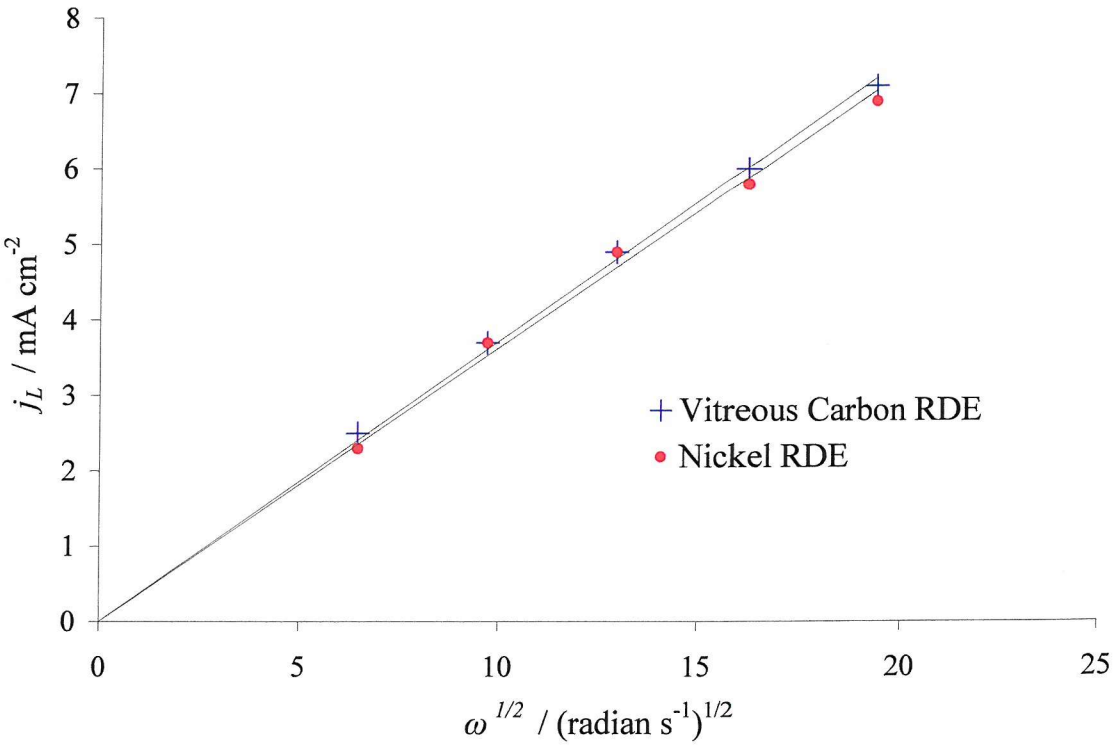

Figure 3.6: *Plot of j_L vs. $\omega^{1/2}$ at vitreous carbon and nickel RDE's (ω = 400, 900, 1600, 2500 and 3600 rpm). The electrolyte comprised of $Pb(CH_3SO_3)_2$ (4.0 mmol dm^{-3}) in aqueous CH_3SO_3H (2.0 mmol dm^{-3}). Potential scan rate 25 mV s^{-1}. Temperature 298 K.*

3.4.2 Deposition of Lead: Lead layers of varying thicknesses were deposited at vitreous carbon and nickel RDE's using current densities between 10 and 40 mA cm^{-2}. Compact, dendrite free deposits were readily obtainable at both electrode materials. However adhesion of the deposited layer to the surface of the electrode was noticeably better at the

nickel electrode. In fact the deposit was readily removed from the vitreous carbon surface by scraping with a finger nail, while anodic dissolution was required to clean the nickel surface.

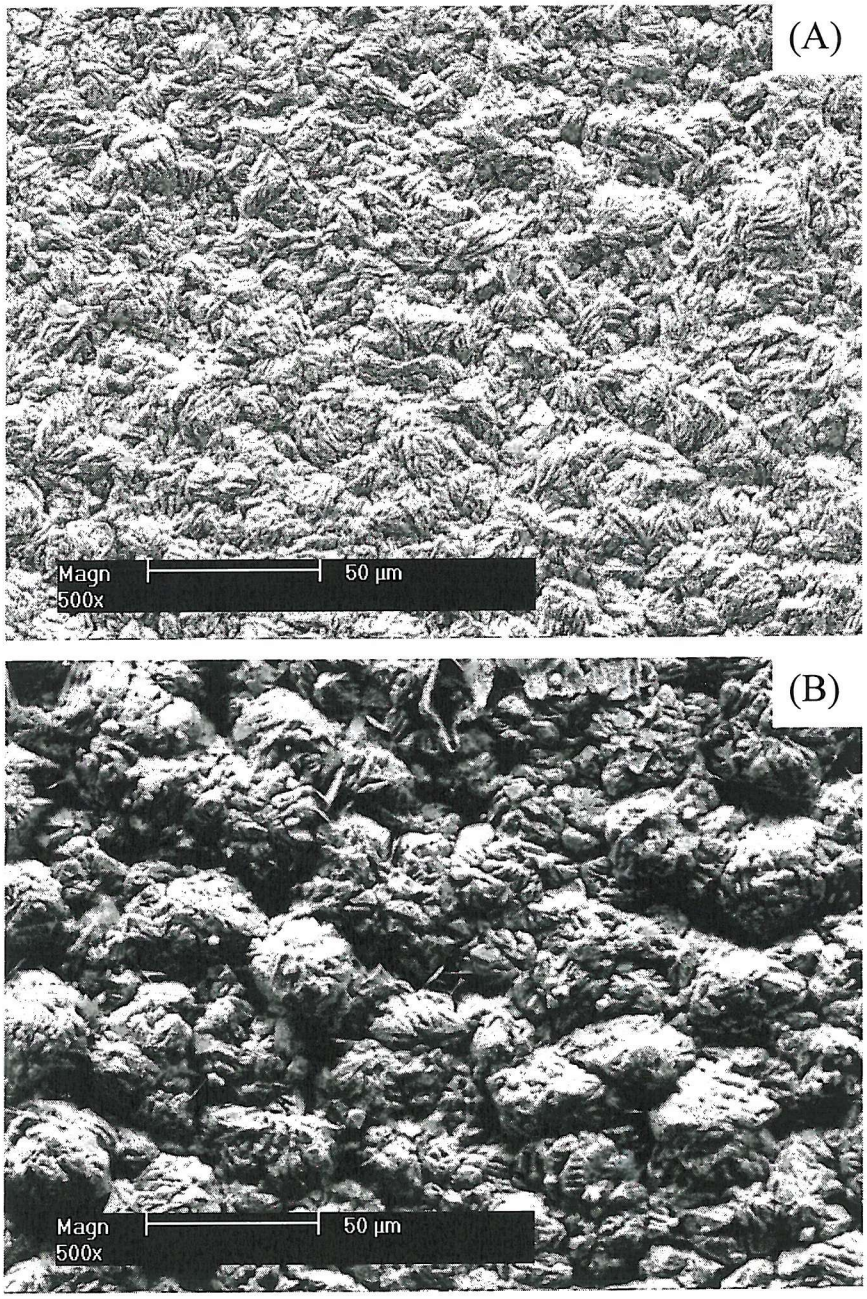

Figure 3.7: *SEM images of lead layers deposited on nickel (A) and vitreous carbon (B) rotating disc electrodes. Both layers were deposited using a current density of 40 mA* cm^{-2} *for 1800 s. Electrolyte:* $Pb(CH_3SO_3)_2$ *(0.3 mol* dm^{-3}*) in aqueous* CH_3SO_3H *(2.0 mol* dm^{-3}*). Rotation rate 900 rpm. Temperature 298 K.*

Figure 3.7 shows SEM images of lead deposits, on nickel (A) and vitreous carbon (B) rotating disc electrodes, using a current density of 40 mA cm^{-2}. Plating was carried out over a 1800 s period (theoretical thickness, 66 μm) from an electrolyte containing 0.3 mol dm^{-3} $Pb(CH_3SO_3)_2$ in aqueous CH_3SO_3H (2.0 mol dm^{-3}). On both vitreous carbon and nickel, the deposited layers were compact and uniform, with no features larger than 30 μm diameter.

3.4.3 Chronopotentiometric Deposition / Dissolution of Lead: A preliminary assessment of the suitability of the Pb^{2+}/Pb couple to be used in a battery was obtained through experiments in which Pb was deposited and re-dissolved several times. Deposition and dissolution correspond respectively to modelling of the charging and discharging of the negative electrode in the envisaged battery system. Each cycle consisted of a deposition at a constant current for a fixed period of time, followed by the discharge of the layer under the same current density until fully removed and the potential rapidly changed, at this point the next cycle was initiated. These experiments were performed at a vitreous carbon RDE and were used to explore the charge / discharge efficiencies and the overpotentials associated with the reaction. Current density, deposition time, temperature and electrolyte composition were all experimental variables.

Figure 3.8 shows a typical set of data from such experiments, obtained from an electrolyte containing 1.5 mol dm^{-3} $Pb(CH_3SO_3)_2$ in 0.9 mol dm^{-3} aqueous CH_3SO_3H. The experiment was recorded at 298 K with a rotation rate of 900 rpm and deposition time of 120 s. The current density used was 25.6 mA cm^{-2}.

A small nucleation peak is visible at the start of the first and second depositions, however on subsequent cycles no overpotential due to the nucleation of lead particles is seen. Both the charge (deposition) and discharge (dissolution) take place at constant potentials and the potentials do not alter during the 5 cycles. The difference in potential between charge and discharge is circa 30 mV and the charge ratio is circa 0.9 throughout.

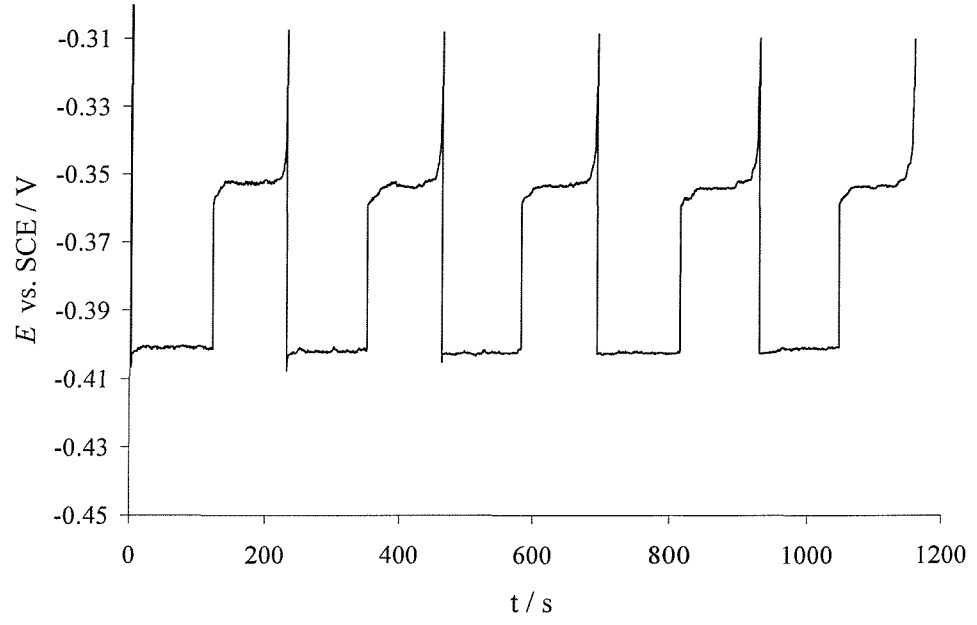

Figure 3.8: *Voltage vs. time plots for five consecutive Pb depositions / dissolutions at a vitreous carbon rotating disc electrode. Each deposition carried out at 25.6 mA cm^{-2} for 120 s. Electrolyte: $Pb(CH_3SO_3)_2$ (1.5 mol dm^{-3}) in aquoeous CH_3SO_3H (0.9 mol dm^{-3}). Temperature: 298 K.*

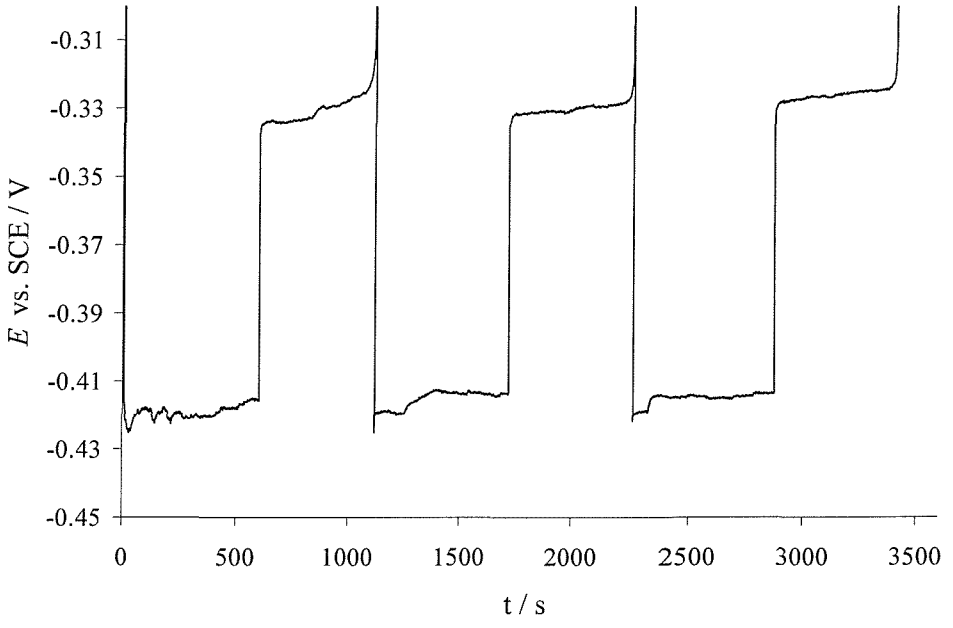

Figure 3.9: *A series of 3 Pb deposition / dissolution cycles. Each cycle consisted of a 600 s charge, at 51.3 mA cm-2, followed by dissolution at the same current density until the voltage reached -0.30 V vs. SCE. Electrolyte: $Pb(CH_3SO_3)_2$ (1.5 mol dm^{-3}) in aquoeous CH_3SO_3H (0.9 mol dm^{-3}). Temperature: 313 K.*

Figure 3.9 shows the charge / discharge profile for three cycles carried out at a current density of 51.3 mA cm^{-2}. The electrolyte comprised 1.5 mol dm^{-3} $Pb(CH_3SO_3)_2$ in 0.9 mol dm^{-3} aqueous CH_3SO_3H. The temperature was 313 K, the rotation rate was 900 rpm and the deposition time was 600 s. As with cycles performed at lower current densities and short deposition times, the charge and discharge potentials are constant and do not vary between cycles. However the difference in potential between charge and discharge is circa 90 mV, which probably contains a contribution from uncompensated IR drop incurred due to the relatively high current density. Despite this the charge / discharge ratios are circa 0.95, showing that the increase in current density and quantity of lead deposited does not adversely effect the charge/discharge profile for this couple at the RDE.

Current Density, j_L / mA cm^{-2}	Deposition Potential, E_c / mV vs. SCE	Stripping Potential, E_d / mV vs. SCE	$\lvert E_c - E_d \rvert$ / mV	Charge Efficiency, $\frac{Q_d}{Q_c}$ / %
6.4	-380	-370	10	84
12.8	-390	-360	30	90
25.6	-400	-350	50	93
51.3	-420	-330	90	92

Table 3.1: *Influence of current density on the constant current charge / discharge cycles for the Pb^{2+}/Pb reaction at the vitreous carbon RDE. Data from the 5th continuous cycle. The charging period was 120 s and the discharge was continues until a sharp change in potential. The electrolyte was $Pb(CH_3SO_3)_2$ (1.5 mol dm^{-3}) in aqueous CH_3SO_3H (0.9 mol dm^{-3}). Rotation rate 900 rpm. Temperature 313 K.*

Table 3.1 shows the influence of current density on the deposition and stripping of lead at current densities between 6.4 mA cm^{-2} and 51.3 mA cm^{-3}. A deposition time of 120 s was used with a rotation rate for the vitreous carbon RDE of 900 rpm. The cell was held in a thermostated bath at a temperature of 313 K and the table gives data from the 5th consecutive cycle. The deposition and stripping potentials become more negative and positive respectively, with increasing current density. The difference between stripping and deposition potentials, $|E_c - E_d|$, increases by circa 20 mV for each twofold increase in current density, within the range tested. This effect is due to the increase in uncompensated

IR drop associated with the higher current densities. Despite this undesirable effect on the potentials, the charge efficiency is not affected.

Similar experiments were performed at 298 K and, at both temperatures, with an electrolyte comprising $Pb(CH_3SO_3)_2$ (0.3 mol dm^{-3}) in aqueous CH_3SO_3H (2.0 mol dm^{-3}) with no significant difference in the potentials or efficiencies.

3.5 PbO_2/Pb^{2+} Electrode Couple

3.5.1 PbO_2/Pb^{2+} Voltammetry: Figures 3.10 and 3.11 show cyclic voltammograms recorded at vitreous carbon and gold rotating disc electrodes respectively. The electrolyte solution consisted of $Pb(CH_3SO_3)_2$ (0.3 mol dm^{-3}) in aqueous CH_3SO_3H (2.0 mol dm^{-3}). The cell was held in a thermostated bath (298 K) and the rotation rate of the electrode was 400 rpm. Potential limits of 0.0 V vs. SCE to 1.85 V vs. SCE for the vitreous carbon electrode and 0.90 V vs. SCE to 1.80 V vs. SCE for the gold electrode were used. These are typical voltammograms for the Pb^{2+}/PbO_2 couple and it should be noted that there are no features associated with mass transfer control. On the positive scan nucleation commences at 1.82 V vs. SCE and 1.77 V vs. SCE at the vitreous carbon and gold electrodes respectively. The voltage is greater on the negative scan and a symmetrical stripping peak commences at circa 1.25 V vs. SCE for both electrode materials. At both the gold and vitreous carbon electrodes there is a significant overpotential associated with the deposition of PbO_2 and the PbO_2/Pb^{2+} couple shows only moderate kinetics.

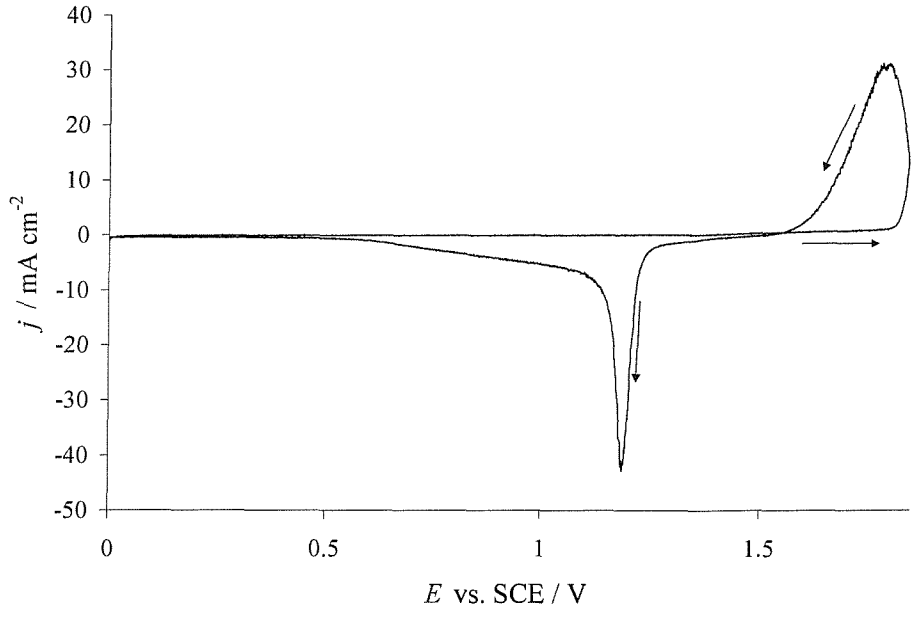

Figure 3.10: *PbO_2 cyclic voltammogram recorded between potential limits of 0 V vs. SCE and 1.85 V vs. SCE at a vitreous carbon RDE. Electrolyte: $Pb(CH_3SO_3)_2$ (0.3 mol dm^{-3}) in aqueous CH_3SO_3H (2.0 mol dm^{-3}). Temperature: 298 K.*

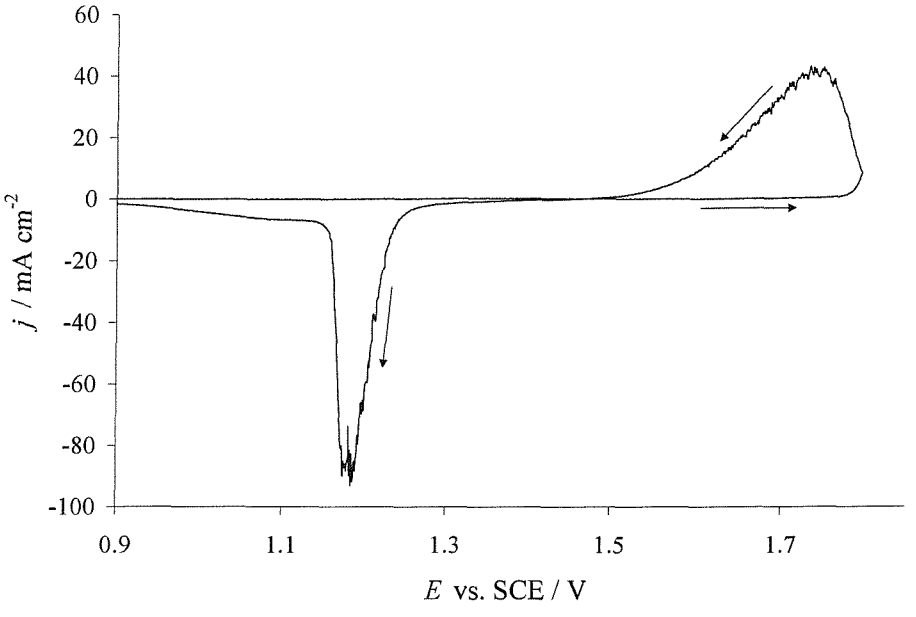

Figure 3.11: *PbO_2 cyclic voltammogram recorded between potential limits of 0.90 V vs. SCE and 1.80 V vs. SCE at a gold RDE. Electrolyte: $Pb(CH_3SO_3)_2$ (0.3 mol dm^{-3}) in aqueous CH_3SO_3H (2.0 mol dm^{-3}). Temperature: 298 K.*

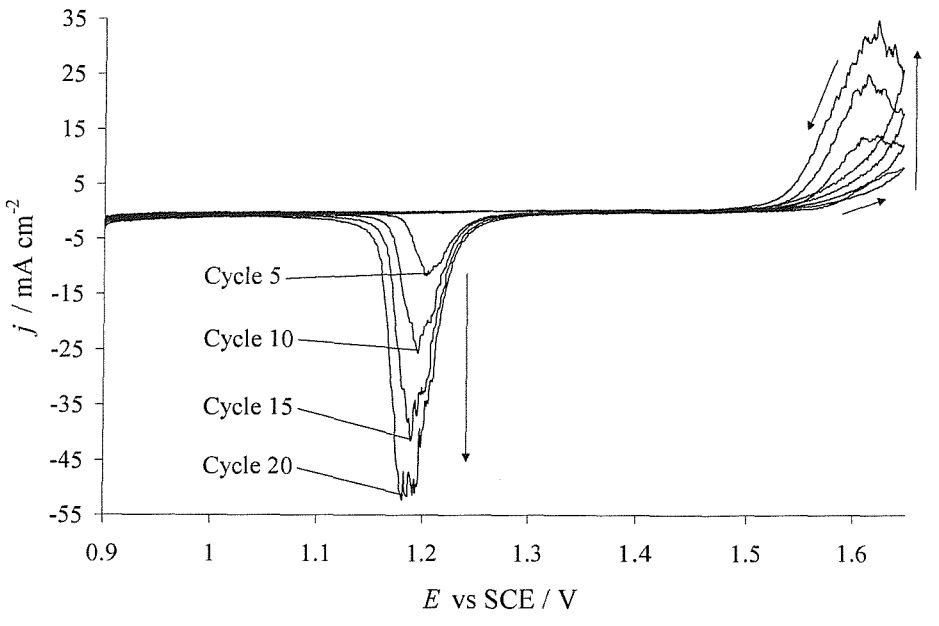

Figure 3.12: *PbO_2 cyclic voltammograms recorded between potential limits of 0.9 V vs. SCE and 1.65 V vs. SCE at a gold RDE. Electrolyte: $Pb(CH_3SO_3)_2$ (0.3 mol dm^{-3}) in aqueous CH_3SO_3H (2.0 mol dm^{-3}). Temperature: 298 K.*

These voltammograms are characteristic of the nucleation and growth of a solid phase on the electrode surface during the positive scan and subsequent dissolution of the deposited layer during the reverse scan. Indeed, the voltammograms are consistent with those reported by several workers for the deposition and stripping of PbO_2 in other acidic media[53-55, 60, 62, 63, 70, 75] and results previously presented in methanesulfonic acid solutions.[76, 85]

It should be noted that the large nucleation overpotential, observed with the deposition of PbO_2, is significantly reduced if voltammograms are recorded consecutively, without polishing the electrode between each scan. Indeed Figure 3.12 shows the 5th, 10th, 15th and 20th cycles of a set of consecutive cyclic voltammograms at a vitreous carbon RDE (ω = 400 rpm) in an aqueous solution containing $Pb(CH_3SO_3)_2$ (0.3 mol dm^{-3}) and CH_3SO_3H (2.0 mol dm^{-3}). The temperature was thermostated at 298 K. The first scan was performed between potential limits of 0.90 vs. SCE and 1.85 V vs. SCE (see figure 3.11), while subsequent scans had an upper limit of 1.65 V vs. SCE. All the voltammograms show the characteristic response for the deposition and dissolution of PbO_2, however it is clear

that as cycling proceeds the deposition of PbO_2 commences at a significantly lower potential (1.54 V vs. SCE for cycle 20) than during the first cycle (1.77 V vs. SCE). In fact, this improvement in the overpotential for the deposition of PbO_2 is seen from the second cycle onwards and is due to the incomplete removal of PbO_2, during the reverse scan of the previous cycle. A small quantity of material remains on the surface of the electrode, even following the potential scan to 0.90 V vs. SCE. During these consecutive cycles, the current densities and charges for both PbO_2 deposition and dissolution are relatively large. The charge balance is also good, $Q_d/Q_c > 0.9$, indicating that the majority of the anodic current is for the oxidation of Pb^{2+} to PbO_2, however if the potential is held above 1.7 V vs. SCE the appearance of O_2 bubbles on the electrode surface is eventually observed.

3.5.2 Deposition of Lead Dioxide: Lead dioxide layers of varying thickness were deposited onto gold and vitreous carbon RDE's. Aqueous electrolytes containing $Pb(CH_3SO_3)_2$ and CH_3SO_3H in various concentrations were used along with current densities from 10 mA cm^{-2} to 60 mA cm^{-2}. Smooth, highly compact deposits were readily obtainable at both the vitreous carbon and gold rotating discs. However adhesion of the PbO_2 layer was much improved on the gold compared to the vitreous carbon. The deposited PbO_2 layers were formed from overlapping hemispherical growth centres and figure 3.13 shows an SEM image of a typical sample, deposited from an electrolyte containing $Pb(CH_3SO_3)_2$ (1.5 mol dm^{-3}) and CH_3SO_3H (0.9 mol dm^{-3}). The cell was thermostated to 298 K, a rotation rate for the RDE of 900 rpm was used and a deposition time of 600 s with current density of 10 mA cm^{-2} applied. The structural appearance of the deposits was unaffected by any of the experimental variables, although at higher current densities and with thicker deposits the adhesion of the layers became more problematic at the vitreous carbon RDE. The PbO_2 disc was prone to detaching from the electrode surface and in effect being forced off the electrode by oxygen evolution or stress in the PbO_2 layer.

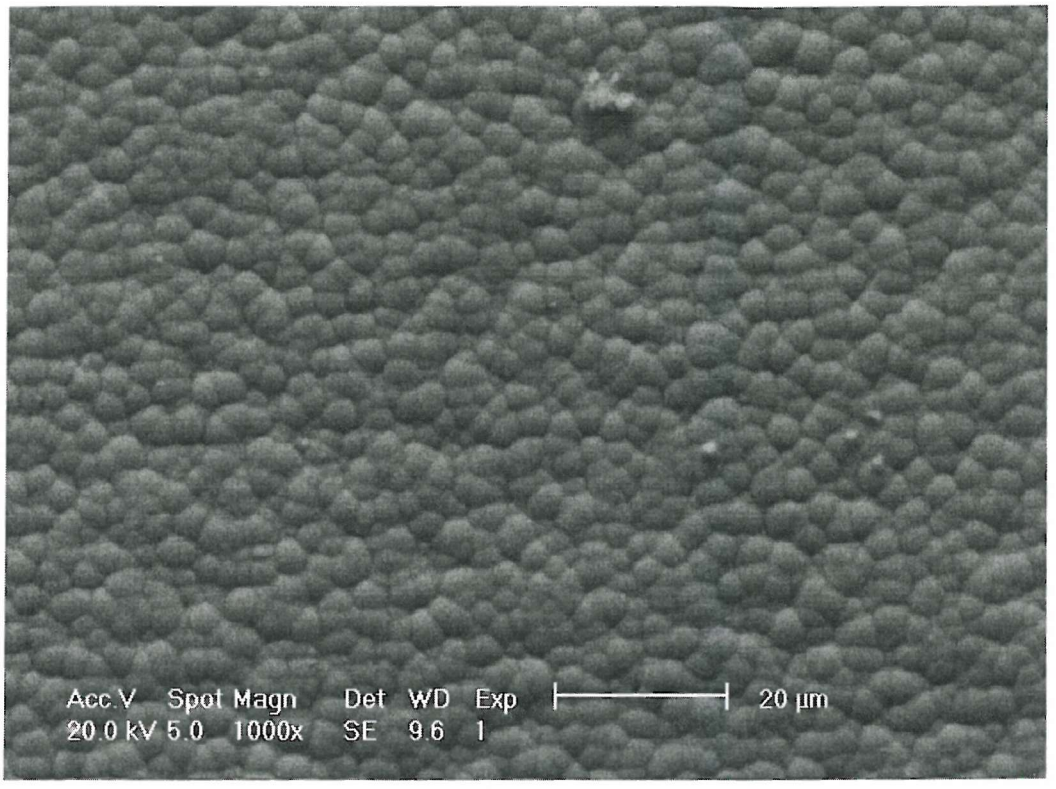

Figure 3.13: *SEM image of a PbO_2 layer deposited on a vitreous carbon rotating disc electrodes. The layer was deposited using a current density of 40 mA cm^{-2} for 600 s. Electrolyte: $Pb(CH_3SO_3)_2$ (1.5 mol dm^{-3}) in aqueous CH_3SO_3H (0.9 mol dm^{-3}). Rotation rate 900 rpm. Temperature 298 K.*

3.5.3 Chronopotentiometric Deposition / Dissolution of Lead Dioxide: As with the Pb^{2+}/Pb couple (section 3.4.3), constant current deposition and dissolution, consecutive cycle experiments were performed at a vitreous carbon RDE and temperature, current density, deposition time, rotation rate and electrolyte composition were all experimental variables.

Figure 3.14 shows a typical set of data from such experiments, with an electrolyte solution containing $Pb(CH_3SO_3)_2$ (1.5 mol dm^{-3}) in aqueous CH_3SO_3H (0.9 mol dm^{-3}) at 313 K. The deposition time was 600 s and the current density 51.3 mA cm^{-2}. During the first cycle, deposition and dissolution occur at constant potentials (1.65 V vs. SCE and 1.18 V vs. SCE for deposition and dissolution respectively). The difference between deposition and stripping potentials of circa 470 mV reflects the large overpotentials associated with this couple. On subsequent cycles, however, deposition of PbO_2 commences at below 1.45

V vs. SCE, but after a period, the potential increases to 1.65 V vs. SCE, the value during the first scan. This is a reproducible phenomenon observed under all experimental conditions used and has been noted for other acid media.[82, 99] A probable explanation for this is the incomplete conversion of PbO_2 to Pb^{2+} during dissolution and the formation of small quantities of PbO. During discharge the reaction layer at the electrode surface has high Pb^{2+} concentration and low H^+ concentration compared to the bulk solution and precipitation of lead oxide / lead hydroxide becomes possible. On the subsequent deposition, PbO_2 is formed at a lower potential by the oxidation of PbO back to PbO_2. A tetragonal form of PbO having a red colour is well known[100] and it has been observed that if the electrodes are inspected following a dissolution experiment, there remains a deep red coloured residue.

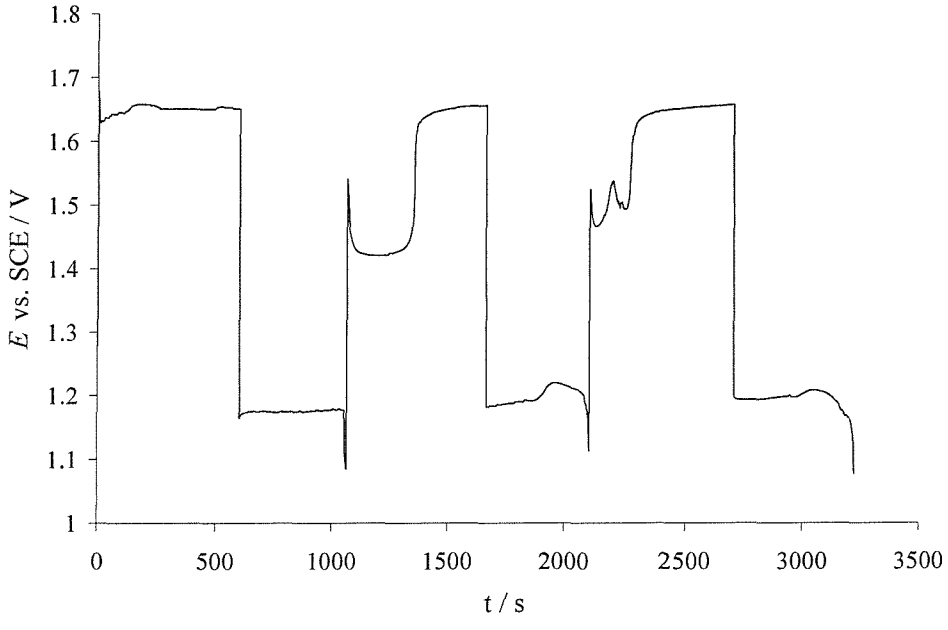

Figure 3.14: *A series of 3 PbO_2 deposition / dissolution cycles. Each cycle consisted of a 600 s charge, at 51.3 mA cm^{-2}, followed by dissolution at the same current density until the voltage reached -0.30 V vs. SCE. Electrolyte: $Pb(CH_3SO_3)_2$ (1.5 mol dm^{-3}) in aquoeous CH_3SO_3H (0.9 mol dm^{-3}). Temperature: 313 K.*

Figure 3.15 shows an SEM image of an electrode following an experiment in which PbO_2 was deposited at 10 mA cm^{-2} for 600 s from a solution containing $Pb(CH_3SO_3)_2$ (1.5 mol dm^{-3}) and CH_3SO_3H (0.9 mol dm^{-3}) and then re-dissolved using a current density of

100 mA cm^{-2}, until the voltage dropped to 0 V vs. SCE. Clearly visible is a deposit with a quite different appearance to the PbO_2 deposits (figure 3.13) and EDAX analysis gives the ratio of lead to oxygen as 1:1, confirming it to be PbO. Despite this phenomenon, the charge discharge ratio is above 0.9 during each of the cycles.

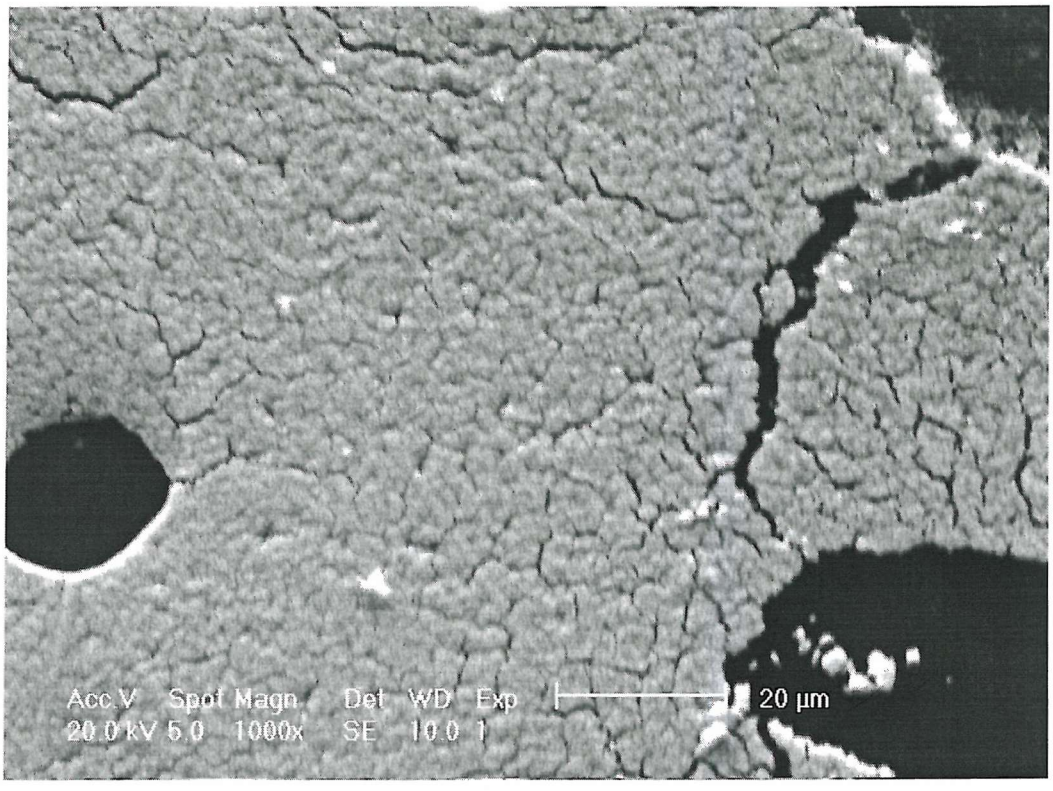

Figure 3.15: *SEM image of the residue deposit, left when a PbO_2 layer deposited and then stripped from a vitreous carbon rotating disc electrodes. The layer was deposited using a current density of 10 mA cm^{-2} for 600 s and stripped by applying a current density of 100 mA cm^{-2} until the voltage reached 0.0 V vs. SCE. Electrolyte: $Pb(CH_3SO_3)_2$ (1.5 mol dm^{-3}) in aqueous CH_3SO_3H (09 mol dm^{-3}). Rotation rate 900 rpm. Temperature 298 K.*

Table 3.2 shows the influence of current density on the deposition and stripping of PbO_2 at current densities between 6.4 mA cm^{-2} and 51.3 mA cm^{-3}. A deposition time of 120 s was used with a rotation rate for the vitreous carbon RDE of 900 rpm. The cell was held in a thermostated bath at a temperature of 313 K and the table gives data from the 5^{th} consecutive cycle. The deposition and stripping potentials become more positive and negative respectively, with increasing current density. This effect is due to the increase in

overpotential and uncompensated IR drop associated with the higher current densities. Despite this undesirable effect on the potentials, the charge efficiency is best at the higher current densities.

Current Density, j_L / mA cm^{-2}	Deposition Potential, E_c / mV vs. SCE	Stripping Potential, E_d / mV vs. SCE	$\lvert E_c - E_d \rvert$	Charge Efficiency, $\frac{Q_d}{Q_c}$ / %
6.4	1.52	1.28	0.24	79
12.8	1.53	1.25	0.28	88
25.6	1.51	1.22	0.29	96
51.3	1.58	1.20	0.38	97

Table 3.2: *Influence of current density on the constant current charge / discharge cycles for the Pb^{2+}/PbO_2 reaction at the vitreous carbon RDE. Data from the 5th continuous cycle. The charging period was 120 s and the discharge was continues until a sharp change in potential. The electrolyte was $Pb(CH_3SO_3)_2$ (1.5 mol dm^{-3}) in aqueous CH_3SO_3H (0.9 mol dm^{-3}). Rotation rate 900 rpm. Temperature 313 K.*

Experiments performed with varying temperature and electrolyte composition gave essentially the same responses with slight variations in the cell voltages obtained, in accordance with the Nernst equation for the PbO_2/Pb^{2+} couple in acidic media. The potentials for PbO_2 deposition and dissolution shifted positive with increasing acid concentration and decreasing Pb^{2+} concentration.

3.6 Chapter 3 Summary

The high solubility of lead(II) methanesulfonate and good conductivity values for the resulting electrolyte solutions suggest that the proposed electrolyte has the desired properties for a battery system. Although a high initial Pb^{2+} concentration limits the conductivity, it should be noted that during charging of the battery [Pb^{2+}] decreases and [H^+] increases and as a result the conductivity rises.

It has been shown that, in the chosen media, the overpotentials associated with the deposition and dissolution of Pb are relatively small (at nickel and vitreous carbon RDE's) and the kinetics associated with the Pb^{2+}/Pb couple are rapid.

The kinetics of the Pb^{2+}/PbO_2 couple (at vitreous carbon and gold RDE's) are significantly slower than with the Pb^{2+}/Pb couple and the overpotentials associated with deposition and stripping of PbO_2 much larger. However the nucleation overpotential for PbO_2 reduces to a great extent with repeated depositions.

Evidence has also been presented supporting the theory that the reduction of PbO_2 in acidic solution does not proceed to completion and a PbO residue is formed. This is not necessarily a detriment to the proposed battery. In fact with subsequent PbO_2 deposition the PbO layer is oxidised at lower overpotentials than Pb^{2+}, giving a reduced cell voltage for this during this period. Clearly this has implications for the energy efficiency of the battery, which is dependent on cell voltage as well as the amount of charge passed.

Chapter 4: The Flow Cell and Flow Cell Electrodes

4.1 Introduction

Data were presented, in chapter 3, on the individual electrode couples (Pb^{2+}/Pb and Pb^{2+}/PbO_2) which demonstrated that, at a rotating disc electrode, the deposition / dissolution of Pb and PbO_2 from aqueous methanesulfonic acid solutions was readily achievable. This chapter extends the investigation to other electrode materials and with the use of a model flow cell combines the two electrode couples into a single, two electrode cell.

This project was supported by Regenesys Ltd and the intention was to employ their electrode materials and to scale up within their cells. They were able to supply a number of different electrodes fabricated by pressing materials into their carbon / polymer composite core. In this thesis the materials are denoted:

- Type I: Core plate.
- Type II: Ni foam.
- Type III: RVC foam.
- Type IV: Scraped RVC.
- Type V: Carbon 500.
- Type VI: Carbon 4500.
- Type VII: Cloth.
- Type VIII: AC 7.

More details of the electrode materials and manufacturing details are given in chapter 2.

4.2 Flow Cell Electrodes

4.2.1 Voltammetry of the Electrodes: Cyclic voltammograms of the Pb^{2+}/Pb couple were performed at stationary Regenesys electrodes of various types. In general, voltammograms obtained from solutions with low Pb^{2+} concentrations were of poor quality with the Regenesys electrodes. The reason was probably the large charging currents associated with the high surface area materials. The exception was the type II (Ni foam) electrode which performed well over a wide range of Pb^{2+} concentrations. Most of the electrode materials produced recognisable voltammograms with solutions having high Pb^{2+} concentrations.

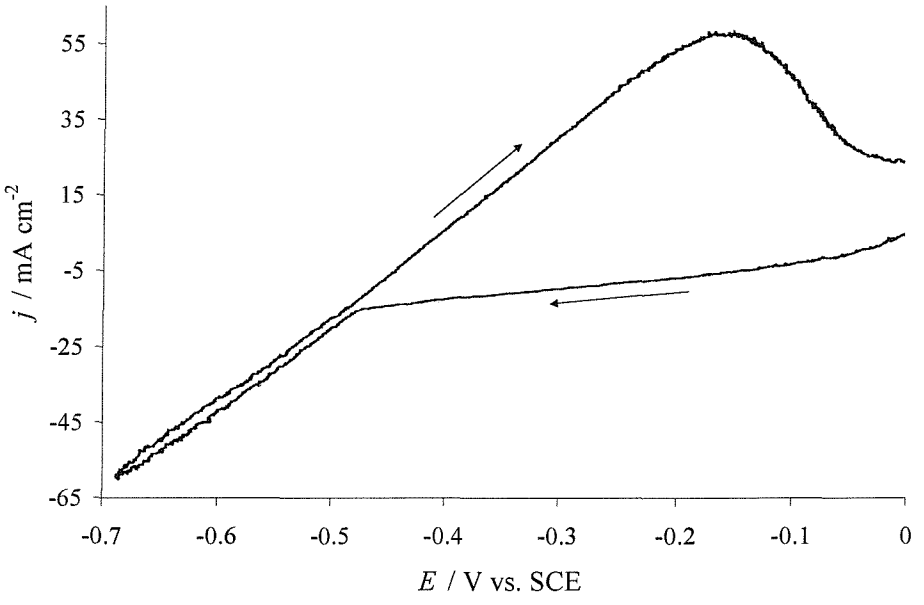

Figure 4.1: *Voltammogram of the Pb^{2+}/Pb couple, performed at a type VI electrode (area = 0.25 cm^2) from a solution consisting of $Pb(CH_3SO_3)$ (0.3 mol dm^{-3}) in aqueous CH_3SO_3H (2.0 mol dm^{-3}). The potential was scanned at 50 mV s^{-1} between 0 V vs. SCE and -0.65 V vs SCE. Temperature: 298 K.*

The electrodes were cut into strips 0.5 cm in width and the exposed core insulated with epoxy resin. The strips were then dipped into the electrolyte solution, held in the same cell used for rotating disc studies, to a depth of 0.5 cm, thus giving an effective electrode

area of 0.25 cm^2. The potential was scanned at a rate of 50 mV s^{-1}. The electrolyte consisted of $Pb(CH_3SO_3)_2$ (0.3 mol dm^{-3}) in aqueous CH_3SO_3H (2.0 mol dm^{-3}) and was maintained at 298 K.

Figure 4.1 shows the voltammogram obtained at the type VI (Carbon 4500) electrode. A cathodic current wave is visible on the negative scan, corresponding to the deposition of Pb and commencing circa -490 mV vs. SCE. However the plot is dominated by IR_u drop. On the reverse scan the voltage vs. potential plot is linear, passing through zero current at -490 mV vs. SCE, and continuing until the majority of the Pb is oxidised before the current decreases towards zero. The voltammograms for type I (core plate) and type V (Carbon 500) electrodes were very similar in appearance to that of the type VI electrode.

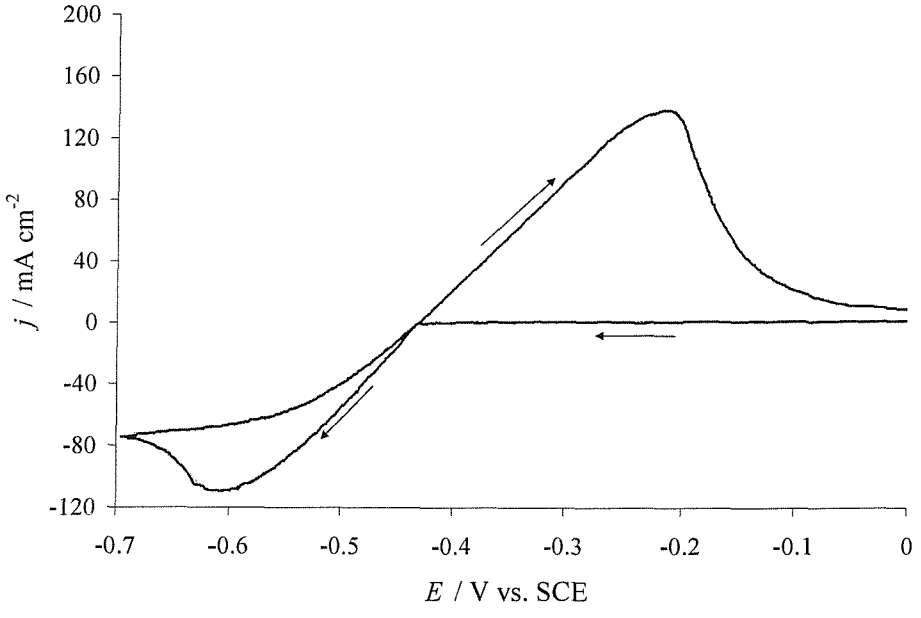

Figure 4.2: *Voltammogram of the Pb^{2+}/Pb couple, performed at a type III (RVC foam) electrode (area = 0.25 cm^2) from a solution consisting of $Pb(CH_3SO_3)$ (0.3 mol dm^{-3}) in aqueous CH_3SO_3H (2.0 mol dm^{-3}). The potential was scanned at 50 mV s^{-1} between 0 V vs. SCE and -0.65 V vs SCE. Temperature: 298 K.*

Figures 4.2 and 4.3 show the voltammograms obtained at type III (RVC foam) and type II (Ni foam) electrodes respectively. Both plots show typical characteristics of voltammograms in which a soluble species is deposited onto and then stripped from a

stationary electrode. However, due to the high $Pb(CH_3SO_3)_2$ concentration in the electrolyte solution, both voltammograms are again distorted by IR_u drop.

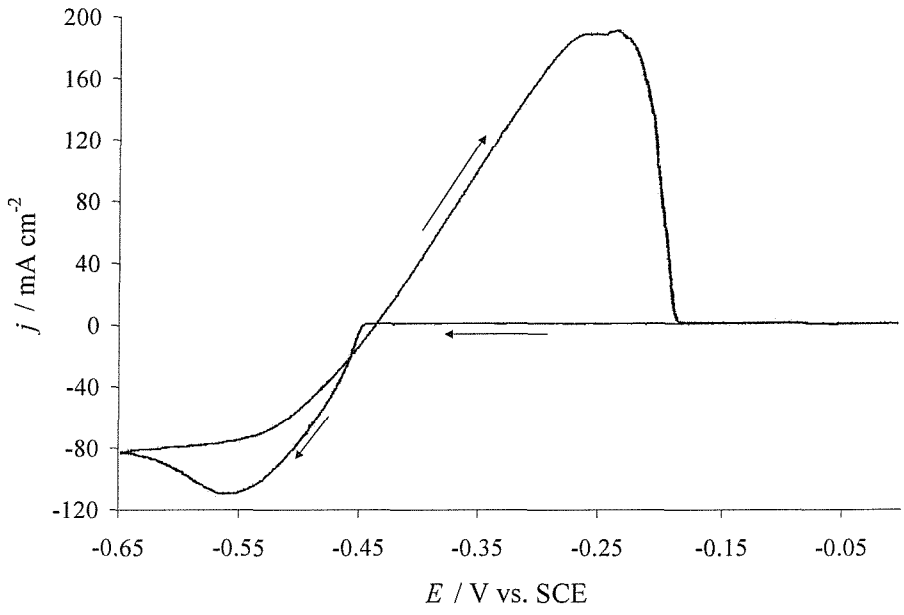

Figure 4.3: *Voltammogram of the Pb^{2+}/Pb couple, performed at a type II (Ni foam) electrode (area = 0.25 cm^2) from a solution consisting of $Pb(CH_3SO_3)$ (0.3 mol dm^{-3}) in aqueous CH_3SO_3H (2.0 mol dm^{-3}). The potential was scanned at 50 mV s^{-1} between 0 V vs. SCE and -0.65 V vs SCE. Temperature: 298 K.*

With the type II electrode the potential was scanned between 0 mV vs. SCE and -700 mV vs. SCE. On the negative scan, the voltammogram shows a sharp cathodic reduction wave, corresponding to Pb deposition, commencing at -445 mV vs. SCE. The current rapidly increases to a maximum before reducing towards a plateau current density (j = -80 mA cm^{-2}). On the reverse scan the deposition of Pb continued to -440 mV vs. SCE before the current became anodic and a stripping peak was observed. With the type III electrode the potential was cycled between 0 mV vs. SCE and -650 mV vs. SCE. The plot obtained had the same form as the voltammogram at the type II electrode. The reduction wave associated with Pb deposition commenced at -450 mV vs. SCE and was more drawn out than the wave produced with the type II electrode, although a plateau region of current density (j = -78 mA cm^{-2}) was again reached after a small peak in current density. On the

reverse scan the deposition of Pb continued to a potential of -440 mV vs. SCE at which point the current became anodic and a stripping peak observed.

Of the electrodes tested, it is clear that the type II and type III electrodes display the most favourable voltammograms.

Figure 4.4 presents a cyclic voltammogram, performed at a type III electrode between potential limits of 0 V vs. SCE and 1.8 V vs. SCE. The response is typical of PbO_2 deposition and stripping in aqueous CH_3SO_3H; on the positive scan, an anodic reduction wave, corresponding to PbO_2 deposition, commences at 1.71 V vs. SCE. The current continues to increase during the initial stages of the reverse scan, before dropping to zero and becoming cathodic at 1.52 V vs. SCE. There is an initial region of low cathodic current density before a sharp stripping peak is observed. The charge balance is circa 90 %.

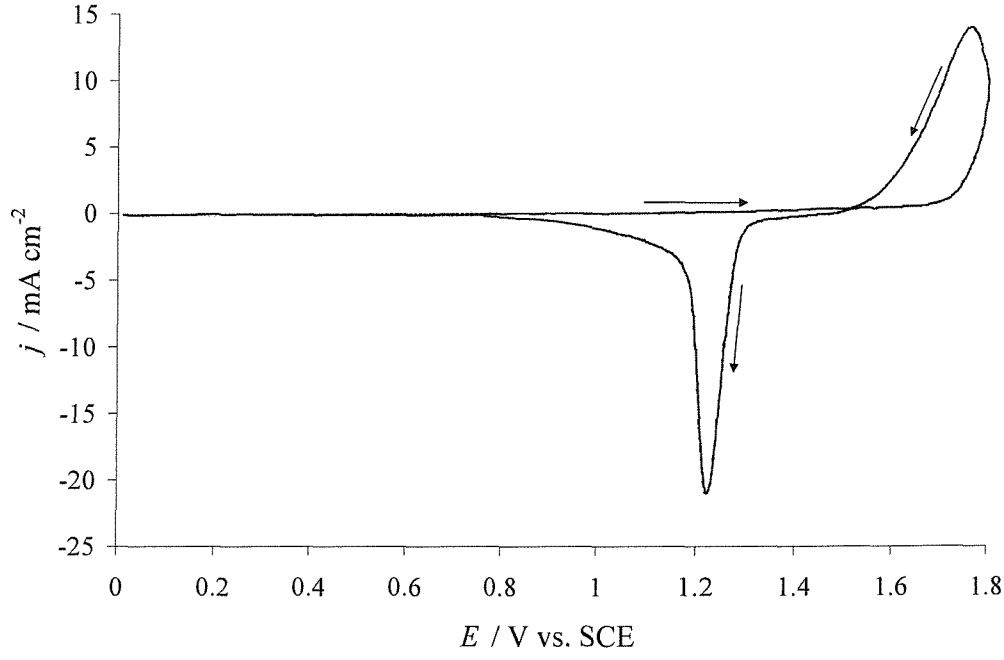

Figure 4.4: *Voltammogram of the Pb^{2+}/PbO_2 couple, performed at a type VI electrode (area = 0.25 cm^2) from a solution consisting of $Pb(CH_3SO_3)$ (0.3 mol dm^{-3}) in aqueous CH_3SO_3H (2.0 mol dm^{-3}). The potential was scanned at 50 mV s^{-1} between 0 V vs. SCE and -0.65 V vs SCE. Temperature: 298 K.*

4.2.2 Deposition onto Type II and Type V (carbon powder) Electrodes: Pb was deposited onto a section of type II electrode (A = 0.25 cm^2). The electrolyte solution comprised $Pb(CH_3SO_3)_2$ (0.3 mol dm^{-3}) in aqueous CH_3SO_3H (2.0 mol dm^{-3}) and was maintained at 298 K. A current density of 160 mA cm^{-2} was applied for 15 seconds. The deposits were analysed using SEM imaging and EDX elemental analysis. Figure 4.5 presents an SEM image (4.5 A) and an image obtained using the EDX software (4.5 B), specifically recording Pb nuclei. The EDX elemental analysis for Pb nuclei clearly shows that Pb is deposited over the majority of the Ni surface and throughout the foams' structure.

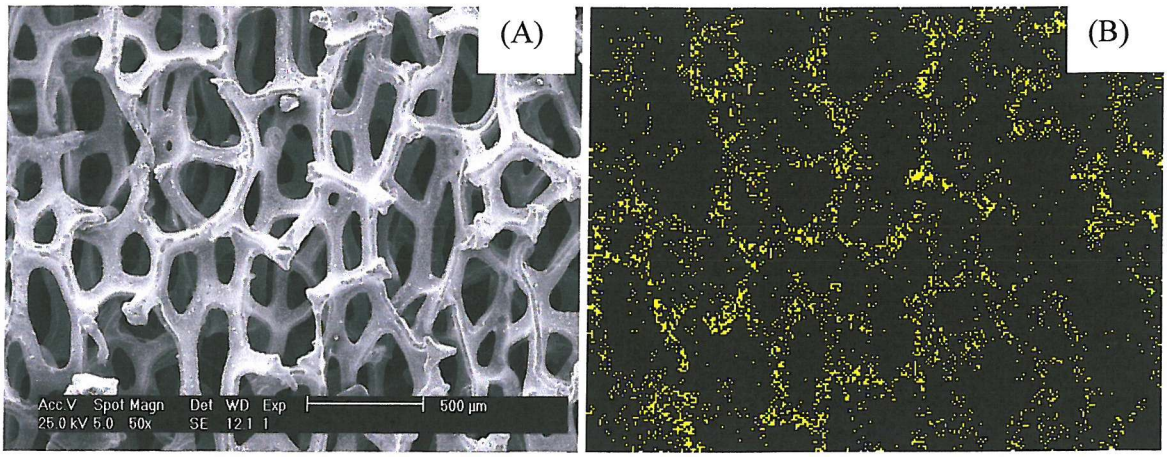

Figure 4.5: *Images taken of a type II electrode following Pb deposition at 160 mA cm^{-2} for 15 s from a solution initially consisting of $Pb(CH_3SO_3)_2$ (0.3 mol dm^{-3}) in aqueous CH_3SO_3H (2.0 mol dm^{-3}).* ***(A)*** *SEM image.* ***(B)*** *EDX elemental analysis for Pb nuclei.*

An identical deposition was performed on a 0.25 cm^2 section of type V electrode. Figure 4.6 presents an SEM image (4.6 A) and the combined EDX elemental analysis for Pb and F nuclei.

The polymer used in the manufacture of the commercial Regenesys (e.g. Type V) electrodes contains fluorine. It can be seen from the overlaid elemental maps of Pb and F nuclei that:

♦ Firstly, there is a large quantity of fluorine present on the outer surface of the granules making up the active tile of the electrode. This shows that the distribution of polymer and carbon is non-ideal and perhaps that the polymer content is too high.

♦ Secondly, Pb preferentially deposits on areas free from fluorine. This lack of Pb deposition onto fluorine containing areas effectively reduces the active area of type I, type V and type VI electrodes.

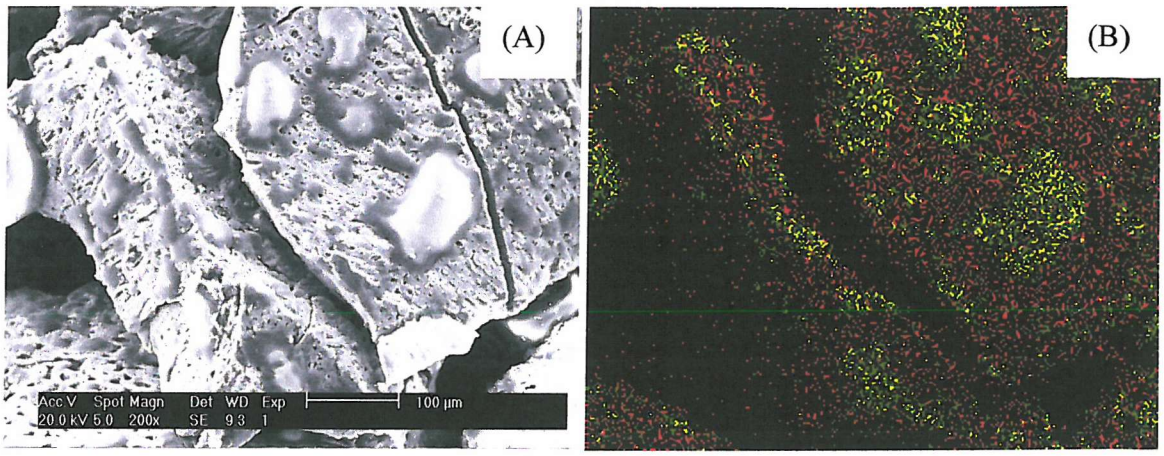

Figure 4.6: *Images taken of a type II electrode following Pb deposition at 160 mA cm^{-2} for 15 s from a solution initially consisting of $Pb(CH_3SO_3)_2$ (0.3 mol dm^{-3}) in aqueous CH_3SO_3H (2.0 mol dm^{-3}).* ***(A)*** *SEM image.* ***(B)*** *Overlaying EDX elemental analysis for Pb (red) and F (yellow) nuclei.*

Various current densities and time periods were used to deposit Pb onto a selection of Regenesys electrode materials (A = 0.25 cm^2). Depositions were carried out from a solution containing $Pb(CH_3SO_3)_2$ (0.3 mol dm^{-3}) in aqueous CH_3SO_3H (2.0 mol dm^{-3}) at a temperature of 298 K. Following the experiments each electrode was analysed using the SEM and EDAX elemental mapping. Data were recorded from the exposed surface of the active tile (Top view), the base of the electrode following removal of a section of the active tile (Base view) and of the cross section, at 70° to horizontal, exposed during scraping off of the active layer (Side view). Table 4.1 presents the data showing the percentage of each surface covered by Pb nuclei.

With all the electrode types, Pb nuclei are observed throughout the porous structure of the active tile however, a visible layer of Pb forms on the top surface before complete filling of the cavities occurs. Although it is clear that Pb deposition occurs throughout the electrode structure it should be noted that, especially with the side views being taken at 70°, there is likely to be some experimental error associated with the percentages and the ratio

of base:top:side. This is inherent from using the EDAX method of analysis with samples with uneven surfaces.

Electrode Type	Deposition Time, t / s	Current Density, j_d / mA cm^{-2}	Base Pb / %	Side Pb / %	Top Pb / %
VI	600	160	0.73	26.0	4.37
VI	60	160	1.47	1.09	0.00
V	3600	160	3.97	18.4	20.4
V	45	160	0.46	1.03	0.29
V	15	160	0.35	0.71	0.29
II	15	160	0.59	5.76	8.44
V	180	80	0.16	5.10	3.19

Table 4.1: *Table showing Pb coverage data from a series of depositions onto various electrode materials.*

Figure 4.7 gives SEM and EDAX (Pb nuclei) images from the cross sectional (side) view of the active tile of a type V electrode, following a 15 s deposition at 160 mA cm^{-2}. Pb nuclei are uniformly distributed throughout the porous structure, from the base to the top, of the active tile.

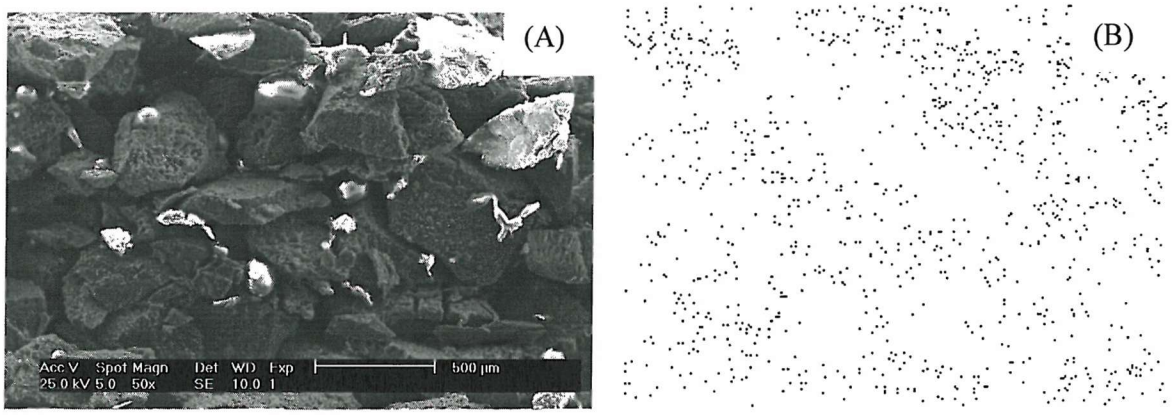

Figure 4.7: *SEM (A) and EDAX (B) images of a type V electrode following Pb deposition for 15 s at 160 mA cm^{-2}. The electrolyte initially contained Pb(CH3SO3)2 (0.3 mol dm-3) in aqueous CH3SO3H (2.0 mol dm-3). Temperature: 298 K. EDAX image shows Pb nuclei.*

4.3 Flow Cell

4.3.1 Sample Electrodes: A series of experiments was performed using the flow cell fitted with various types of electrode. In each experiment the same electrode material was used for both the positive and negative plates. The cell was charged for 19 minutes, at 20 mA cm^{-2} before being discharged for 3 minutes at the same current density. The electrolyte initially comprised $Pb(CH_3SO_3)_2$ (0.3 mol dm^{-3}) in aqueous CH_3SO_3H (2.0 mol dm^{-3}) and was pumped from a reservoir maintained at 298 K. The flow rate across the electrodes was set at 2.5 cm s^{-1} and electrical connection was made via a screw contact to the rear of the electrode. Figure 4.8 presents voltage vs. time plot for the charge / discharge cycles obtained using type III and type VIII electrodes. With the type III electrodes, there is a small nucleation peak in the voltage at the start of the charge, following which the voltage rapidly reaches a plateau value of 2.19 V, at which it stays for the remainder of the charge. During discharge the voltage is steady at 1.55 V for the full three minutes. This is a typical profile expected for a battery system. However, the voltage vs. time profile obtained with the type VIII electrodes shows a slow increase in the cell voltage, following the application of the charging current, leading to a plateau voltage of 1.52 V. On discharge the voltage immediately begins to drop off and at the end of the 3 minute period reaches a value of 0.8 V. The voltage vs. time profiles obtained using type V, type VI and type VII electrodes were similar in form to the type VIII electrodes. It is thought that the positive electrode is initially acting as a super-capacitor, with no PbO_2 being deposited. Indeed when the cell is dismantled no PbO_2 deposit is seen. It is clear, that from this initial set of experiments (at short times, anyway), the RVC material shows the most reasonable characteristics for a battery system.

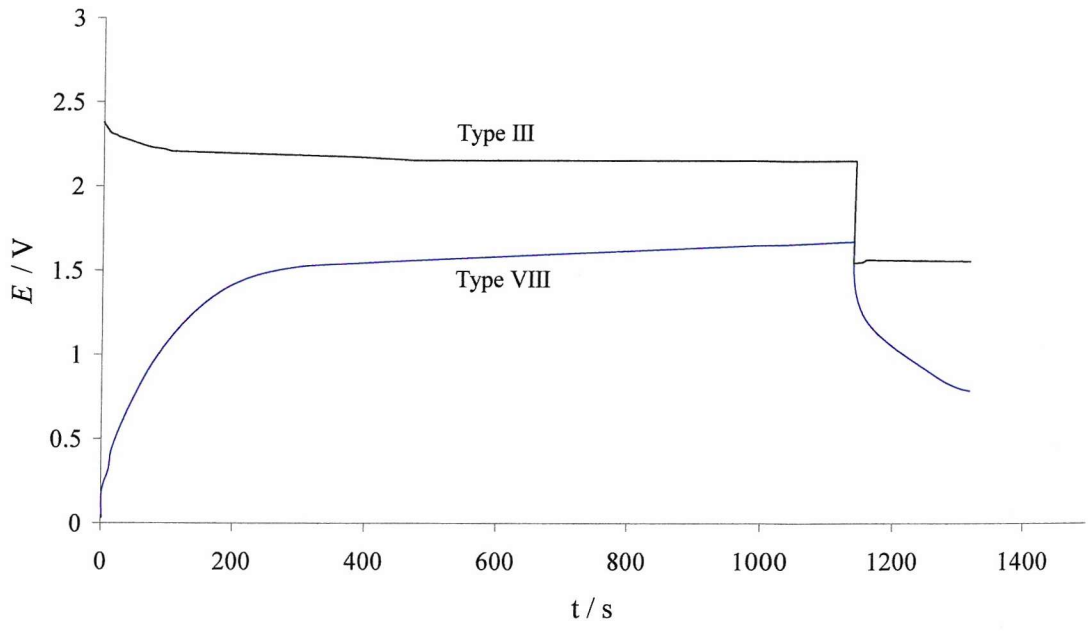

Figure 4.8: *Voltage vs. time profile for charge and discharge of the flow cell, fitted with various electrode materials. The interelectrode gap was 1.6 cm and the mean linear flow rate across the electrodes' surface was 2.5 cm s^{-1}. The electrolyte (30 cm^3) was pumped from a thermostated reservoir (298 K) and initially consisted of $Pb(CH_3SO_3)_2$ (0.3 mol dm^{-3}) in CH_3SO_3H (2.0 mol dm^{-3}).*

4.3.2 Charging and Discharging the Cell: The flow cell was fitted with two, new type III (RVC foam) electrodes. The interelectrode gap was 0.4 cm and the linear flow rate across the electrodes surfaces was 10 cm s^{-1}. Electrical connection was made via a screw contact to the reverse of the electrode. The electrolyte (0.04 dm^3) was held in a thermostated reservoir (298 K) and initially consisted of $Pb(CH_3SO_3)_2$ (1.5 mol dm^{-3}) in aqueous CH_3SO_3H (0.9 mol dm^{-3}). A series of 6 consecutive charge / discharge cycles were applied to the cell. Each cycle consisted of a 900 s charge (j = 20 mA cm^{-2}) followed by discharge, at the same current density, until the cell voltage dropped to 1.20 V.

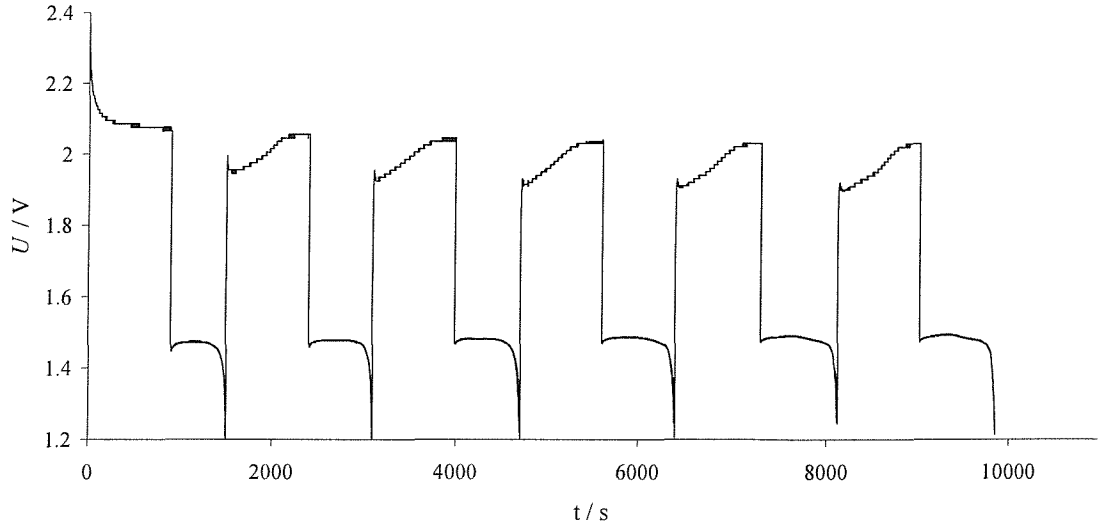

Figure 4.9: *Voltage vs. time profile for 6 charge discharge cycles performed with the flow cell (fitted with two, new type III electrodes). The interelectrode gap was 0.4 cm and the mean linear flow rate across the electrodes' surface was 10 cm s^{-1}. The electrolyte (40 cm^3) was pumped from a thermostated reservoir (298 K) and initially consisted of $Pb(CH_3SO_3)_2$ (1.5 mol dm^{-3}) in CH_3SO_3H (0.9 mol dm^{-3}).*

Figure 4.9 presents the voltage vs. time plot for the 6 cycles. Following a small nucleation overvoltage, the initial charge takes place at a relatively steady voltage of circa 2.08 V. This is followed by a steady voltage for discharge of circa 1.47 V until one of the reactants, probably PbO_2 is fully consumed, at which point the voltage rapidly drops. The coulombic efficiency of this first cycle is 67 %. On the second and subsequent cycles, the voltage during initial stages of charging is significantly lower (circa 1.96 V) than observed for the first cycle. However over the course of the cycle the voltages rise to circa 2.06 V. This behaviour has been noted previously, when examining the individual electrode reactions, and is associated with the Pb^{2+}/PbO_2 electrode couple. The coulombic efficiency of these cycles varied between 67 and 92 %. This experiment clearly shows that, over a limited number of short cycles, the cell can be fully discharged and recharged without significant problems.

Table 4.2 gives the charge voltages (initial value and after rising to a plateau), discharge voltage and coulombic efficiency for the 6 cycles.

Cycle	U_c / V	U_d / V	$U_c - U_d$ / V	Q_d/Q_c / %
1	2.08	1.47	0.61	67
2	1.96 – 2.06	1.48	0.48 – 0.58	77
3	1.95 – 2.05	1.48	0.47 – 0.57	80
4	1.91 – 2.04	1.49	0.42 – 0.55	88
5	1.92 – 2.03	1.48	0.44 – 0.55	91
6	1.91 – 2.03	1.49	0.42 – 0.54	92

Table 4.2: *Data from 6 charge / discharge cycles in the flow cell, with two type III electrodes. Each cycle consisted of a 900 s charge (j = 20 mA cm^{-2}) followed by discharge to 1.20 V at the same current density. The electrolyte (0.03 dm^{-3}) initially consisted of $Pb(CH_3SO_3)_2$ (1.5 mol dm^{-3}) in aqueous CH_3SO_3H (0.9 mol dm^{-3}) and was pumped through the cell with a linear flow rate of 10 cm s^{-1} from a thermostated reservoir (298 K).*

Another type of cycling is presented in figure 4.10. Here the cell was again fitted with two new, type III electrodes and supplied with an electrolyte (0.03 dm^{-3}) initially containing $Pb(CH_3SO_3)_2$ (1.5 mol dm^{-3}) in aqueous CH_3SO_3H (0.9 mol dm^{-3}). The electrolyte reservoir was thermostated at 298 K, the interelectrode gap was 1.6 cm and the linear flow rate through the cell was 2.5 cm s^{-1}. The cell was initially charged for 1 hour before being subjected to a series of 17 partial discharge / charge cycles. Each mini cycle consisted of a 300 s discharge followed by a 300 s charge cycles, both at a current density of 20 mA cm^{-2}. Finally the cell was fully discharged until the voltage dropped to 1.20 V. A current density of 20 mA cm^{-2} was used throughout. Method B (Pt mesh) was used to make electrical contact to the electrodes within the cell.

During the initial charge there is a small nucleation overvoltage before the voltage gradually falls from 2.05 V to 2.01 V over time. During each of the partial discharges the voltage remains relatively steady at circa 1.49 V in throughout the seventeen discharges. As noted previously with the full charge / discharge cycles, each of the 300 s charges show an increase in voltage over the course of the charge. There is also a slight improvement in the voltages between the first of the short charges (1.89 V rising to 1.97 V) and the seventeenth charge (1.85 V rising to 1.91 V). During the full discharge, at the end of the cycling, the voltage is initially 1.49 V and gently drops to circa 1.43 V before sharply dropping off. The overall coulombic efficiency is 93 %, demonstrating that no loss of performance is observed when the cell is subjected to a series of incomplete discharge / charge cycles. It is

important that good efficiencies are obtainable during partial cycling as such a regime would be implemented during operation of a load levelling system.

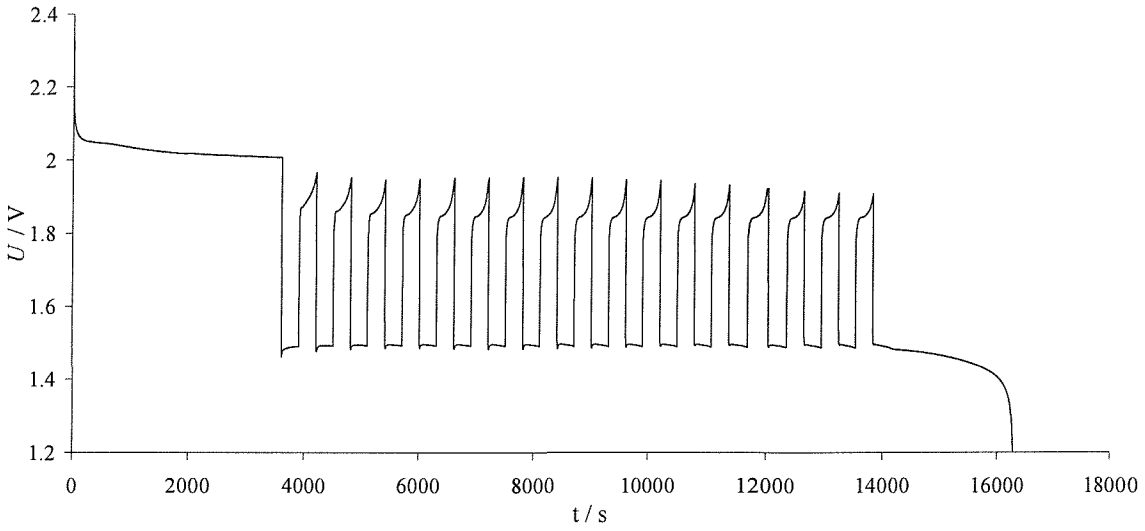

Figure 4.10: *Voltage vs. time profile for charge/discharge cycles performed with the flow cell (fitted with two, new type III electrodes). The interelectrode gap was 1.6 cm and the mean linear flow rate across the electrodes' surface was 2.5 cm* s^{-1}*. The electrolyte (40* cm^3*) was pumped from a thermostated reservoir (298 K) and initially consisted of* $Pb(CH_3SO_3)_2$ *(1.5 mol* dm^{-3}*) in* CH_3SO_3H *(0.9 mol* dm^{-3}*).*

4.4 Flow Cell Configuration

4.4.1 Interelectrode Spacing: Two cycling experiments were performed in which the flow cell was fitted with two, new type IV (Scraped RVC foam) electrodes. The interelectrode gap was either 0.4 cm or 1.6 cm and the linear flow rate across the electrodes' surface was 2.5 cm s^{-1}. Electrical connection was made via a screw contact to the reverse of the electrode. The electrolyte (0.03 dm^3) was held in a thermostated reservoir (298 K) and initially consisted of $Pb(CH_3SO_3)_2$ (1.5 mol dm^{-3}) in aqueous CH_3SO_3H (0.9 mol dm^{-3}). A series of 6 consecutive charge / discharge cycles were applied to the cell. Each cycle consisted of a 900 s charge (j = 20 mA cm^{-2}) followed by discharge, at the same current density, until the cell voltage dropped to 1.20 V. Table 4.3 presents the charge

voltage, discharge voltage and coulombic efficiency for each of the 6 cycles from the two experiments. It is clear to see that reducing the interelectrode gap and hence reducing IR drop from the electrolyte has a marked effect on the cell performance. The charge and discharge voltages reduce and increase, respectively, by up to 100 mV and the coulombic efficiency increases by up to 10 %.

Interelectrode Gap / cm	Cycle	U_c / V	U_d / V	$\frac{Q_d}{Q_c}$ / %
1.6	1	2.24	1.32	74
	2	2.06 – 2.24	1.31	77
	3	2.04 – 2.22	1.32	80
	4	2.04 – 2.19	1.32	81
	5	2.01 – 2.12	1.34	80
	6	2.01 – 2.08	1.33	77
0.4	1	2.13	1.44	84
	2	1.93 – 2.13	1.44	84
	3	1.94 – 2.12	1.45	87
	4	1.93 – 2.10	1.46	89
	5	1.91 – 2.07	1.47	89
	6	1.90 – 2.03	1.47	88

Table 4.3: *Data from two experiments performed in the flow cell, each consisting six charge/discharge cycles, varying the interelectrode gap between 0.4 and 1.6 cm.*

4.4.2 Electrical Connection: The flow cell was subjected to a series of three experiments, with each experiment utilising a different method for making electrical contact to the electrodes. In the first case, electrical connection was made via a screw contact to the reverse of the electrode (Method A). In the second case, electrical contact to the back of the electrode was improved with the use of a platinum mesh (Method B), to spread electrical contact across the entire back face of the electrodes. In the third case, the electrical connection was made by stripping the insulating sleeve from a section of multi-core wire, spreading the untwisted individual strands across the rear face of the electrode and melting these strands into the carbon polymer core with the use of a soldering iron. The rear of the electrode was then sealed with epoxy resin (Method C).

The electrodes used were type II (negative) and type IV (positive), with each experiment using a fresh set. The interelectrode gap was 0.4 cm and the linear flow rate across the electrodes' surface was 10 cm s^{-1}. The electrolyte (0.04 dm^3) was held in a thermostated reservoir (298 K) and initially consisted of $Pb(CH_3SO_3)_2$ (1.5 mol dm^{-3}) in aqueous CH_3SO_3H (0.9 mol dm^{-3}). The individual experiments comprised a series of 6 consecutive charge / discharge cycle. Each cycle consisted of a 900 s charge (j = 20 mA cm^{-2}) followed by discharge, at the same current density, until the cell voltage dropped to 1.20 V.

Electrical Connection	Cycle	U_c / V	U_d / V	U_c - U_d / V	$\frac{Q_d}{Q_c}$ / %
Method A	1	2.21	1.34	0.87	79
	2	2.08 – 2.12	1.44	0.64 – 0.68	86
	3	1.97 – 2.10	1.46	0.51 – 0.64	89
	4	1.93 – 2.09	1.47	0.46 – 0.62	89
	5	1.92 – 2.08	1.48	0.44 – 0.60	87
	6	1.93 – 2.09	1.48	0.45 – 0.61	86
Method B	1	2.09	1.48	0.61	88
	2	1.92 – 2.09	1.50	0.42 – 0.59	87
	3	1.92 – 2.08	1.50	0.42 – 0.58	92
	4	1.92 – 2.09	1.49	0.43 – 0.60	92
	5	1.91 – 2.09	1.49	0.42 – 0.60	92
	6	1.91 – 2.08	1.49	0.42 – 0.59	93
Method C	1	2.04	1.54	0.50	86
	2	1.85 – 2.03	1.56	0.29 – 0.47	86
	3	1.84 – 2.03	1.55	0.29 – 0.48	92
	4	1.84 – 2.03	1.55	0.29 – 0.48	92
	5	1.83 – 2.01	1.55	0.28 – 0.46	92
	6	1.83 – 1.99	1.55	0.28 – 0.44	92

Table 4.4: *Data from charge / discharge cycles in the flow cell with various methods of making electrical contact to the electrodes. The cell was charged for 900 s at 20 mA cm^{-2} and then discharged at the same current density until the voltage dropped to 1.20 V. Interelectrode gap: 0.4 cm. Electrolyte initially $Pb(CH_3SO_3)_2$ (1.5 mol dm^{-3}) in aqueous CH_3SO_3H (0.9 mol dm^{-3}), linear flow rate 10 cm s^{-1}. Temperature 298 K.*

Table 4.4 shows the charge voltage, discharge voltage, difference between voltages and coulombic efficiency for the three experiments. It is clear that the resistance associated with the carbon/polymer composite, which makes up the electrodes core plate, is not inconsiderable. Immediately apparent is a reduction in IR drop, and hence an improvement in the charge/discharge voltages as the electrical connection is improved. With the screw

connection the difference between charge and discharge voltages is between 0.42 V and 0.61 V during the final cycle. However this drops to between 0.28 V and 0.44 V using the mesh connection. Also worth noting is the increase in coulombic efficiency as the current is more evenly distributed across the back of the electrode when using the Pt mesh and wire connection methods.

4.4.3 Electrode Material: Table 4.5 reports data from a series of charge / discharge cycles using various types of electrode. Each cycle consisted of a 900 s charge (j = 20 mA cm^{-2}) followed by discharge at the same current density until the voltage dropped to 1.20 V. In each case the electrolyte initially consisted of $Pb(CH_3SO_3)_2$ (1.5 mol dm_{-3}) in aqueous CH_3SO_3H (0.9 mol dm^{-3}) and was pumped from a thermostated reservoir (298 K) through the cell with a linear flow rate of 10 cm s^{-1}. The interelectrode gap was set at 0.4 cm and electrical connection was made with the use of a platinum mesh pressed against the reverse of the electrode.

It should be noted that the current density in each experiment was calculated using the planar geometric area of the electrode. Consequently the IR_u component of the overpotentials at the positive and negative electrodes will be larger for the type I and IV electrodes than the type II and III electrodes. However the effect on the observed voltages is thought to be relatively small and the voltage trends follow those observed for the overvoltages obtained from cyclic voltammograms on the various electrode materials.

As expected the coulombic efficiency obtained with the smooth, type I electrodes was relatively low. Using type I and type III electrodes it was observed that during the course of cycling a significant quantity of red / black, particulate sediment accumulated in the reservoir. It was thought that this originated from the PbO_2 electrode, indeed when the cell was dismantled and the electrodes examined, a loose residue was visible on the positive plates. The formation of sediment was greatly reduced with the use of type IV electrodes as the positive plate and combined with either type II or type III electrodes as the negative plate and there is a significant increase in the value and consistency of the coulombic efficiencies.

Electrode		Cycle	$\frac{Q_d}{Q_c}$ / %	U_c / V	U_d / V	U_c - U_d / V
Positive	Negative					
Type I	Type I	1	74	2.14	1.45	0.69
		2	69	1.94 – 2.14	1.45	0.49 – 0.69
		3	69	1.93 – 2.14	1.45	0.48 – 0.69
		4	71	1.95 – 2.13	1.45	0.50 – 0.68
		5	75	1.95 – 2.12	1.45	0.50 – 0.67
		6	86	1.89 – 1.96	1.46	0.43 – 0.50
Type III	Type III	1	67	2.04	1.50	0.54
		2	83	1.92 – 2.02	1.51	0.41 – 0.51
		3	91	1.89 – 1.98	1.51	0.38 – 0.47
		4	92	1.89 – 1.97	1.51	0.38 – 0.46
		5	87	1.89 – 1.96	1.50	0.39 – 0.46
		6	87	1.89 – 1.96	1.51	0.38 – 0.45
Type IV	Type IV	1	82	2.10	1.47	0.63
		2	85	1.95 – 2.09	1.48	0.47 – 0.61
		3	85	1.94 – 2.09	1.47	0.47 – 0.62
		4	89	1.92 – 2.09	1.48	0.44 – 0.61
		5	86	1.93 – 2.09	1.48	0.45 – 0.61
		6	86	1.93 – 2.09	1.47	0.46 – 0.62
Type IV	Type III	1	85	2.15	1.42	0.73
		2	88	1.98 – 2.15	1.45	0.53 – 0.70
		3	92	1.97 – 2.15	1.45	0.52 – 0.70
		4	91	1.97 – 2.14	1.45	0.52 – 0.69
		5	91	1.96 – 2.14	1.45	0.51 – 0.69
		6	91	1.97 – 2.14	1.45	0.52 – 0.69
Type IV	Type II	1	88	2.09	1.48	0.61
		2	87	1.92 – 2.09	1.50	0.42 – 0.59
		3	92	1.92 – 2.08	1.50	0.42 – 0.58
		4	92	1.92 – 2.09	1.49	0.43 – 0.60
		5	92	1.92 – 2.09	1.49	0.43 – 0.60
		6	93	1.91 - 2.08	1.49	0.42 – 0.59

Table 4.5: *Data from 6 charge / discharge cycles in the flow cell with various electrodes. The cell was charged for 900 s at 20 mA cm^{-2} and then discharged at the same current density until the voltage dropped to 1.20 V. Interelectrode gap: 0.4 cm. Electrolyte initially $Pb(CH_3SO_3)_2$ (1.5 mol dm^{-3}) in aqueous CH_3SO_3H (0.9 mol dm^{-3}), linear flow rate 10 cm s^{-1}. Temperature 298 K. Electrical contact made via platinum mesh.*

4.4.4 Electrolyte Flow Rate: Two experiments were performed in which the flow cell was fitted with two, new type IV electrodes. The interelectrode gap was 0.4 cm and the linear flow rate across the electrodes' surface was either 2.5 cm s^{-1} or 10 cm s^{-1}. Electrical connection was made via a screw contact to the reverse of the electrode. The electrolyte (0.04 dm^3) was held in a thermostated reservoir (298 K) and initially consisted of

$Pb(CH_3SO_3)_2$ (1.5 mol dm^{-3}) in aqueous CH_3SO_3H (0.9 mol dm^{-3}). A series of 6 consecutive charge / discharge cycles were applied to the cell. Each cycle consisted of a 900 s charge (j = 20 mA cm^{-2}) followed by discharge, at the same current density, until the cell voltage dropped to 1.20 V.

Electrolyte flow rate / cm s^{-1}	Cycle	U_c / V	U_d / V	$\frac{Q_d}{Q_c}$ / %
10	1	2.14	1.45	69
	2	1.97 – 2.13	1.45	71
	3	1.94 – 2.12	1.46	78
	4	1.92 – 2.12	1.46	80
	5	1.91 – 2.11	1.47	85
	6	1.90 – 2.10	1.47	87
2.5	1	2.13	1.44	84
	2	1.93 – 2.13	1.44	84
	3	1.94 – 2.12	1.45	87
	4	1.93 – 2.10	1.46	89
	5	1.91 – 2.07	1.47	89
	6	1.90 – 2.03	1.47	88

Table 4.6: *Data from two experiments performed in the flow cell, each consisting six charge/discharge cycles, the interelectrode gap was 0.4 and the electrolyte initially consisted of $Pb(CH_3SO_3)_2$ (1.5 mol dm^{-3}) in aqueous CH_3SO_3H (0.9 mol dm^{-3}). The temperature was maintained at 298 K.*

Data from the two sets of cycles is presented in table 4.6. As would be expected, changing the linear flow rate has a negligible effect on the charge and discharge voltages. The coulombic efficiency during the first cycle is 15 % lower with the higher flow rate, however the efficiency gradually recovers during subsequent cycles and by the sixth cycle is comparable to the slower flow rate. The low efficiency during the initial cycles may be attributed to an increased difficulty for nuclei formation with the higher flow rate.

4.5 Chapter 4 Summary

It has been shown that some electrode materials, such as RVC and nickel foam, are preferential for Pb and PbO_2 deposition / stripping and hence battery cycling. In fact the fluorinated polymer used in the manufacture of the Regenesys core plates and some active tiles inhibits the formation of deposits. Electrodes made using these materials do not perform well in the flow cell and it is believed, under charging / discharging conditions, act as supercapacitors.

It was demonstrated that the flow cell could be operated as a battery system and, over a limited number of short cycles, it was successfully operated both with full discharging before recharge and with partial discharge / charge cycles.

Encouraging voltage vs. time profiles were produced with the flow cell, using electrodes of type II through IV and constant charge / discharge currents. In fact coulombic efficiencies of circa 90 % were readily achievable.

It was also found that significant improvements to the cells' performance could be gained by varying the cell configuration. Notably, improving electrical connection and current distribution to the electrodes along with reducing the interelectrode separation considerably enhanced the cell voltages and coulombic efficiency.

Chapter 5: Further Flow Cell Studies

5.1 Introduction

Chapter 4 showed that the flow cell could be operated successfully as a battery under complete and partial charge/discharge regimes. This chapter presents results demonstrating that the charge/discharge cycles may be extended in length or repeated many more times, with similar coulombic efficiencies and high energy efficiencies. Repeated cycling and long charge discharge times are both required if the battery system is to be used as a utility scale device.

The Nernst equation, applied to the soluble lead acid system to give equation 44, predicts that the cell potential is dependent on the concentrations of Pb^{2+} and H^{+} in the electrolyte as well as temperature. It is also likely that the overpotentials for each of the electrode couples will be increased with the use of higher current densities. Consequently, the effect of temperature, current density and state of charge on the cell performance were investigated.

Also addressed is the potential problem of excess deposit building up on one of the electrode plates due to imbalance between efficiencies of the reactions taking place at the positive and negative electrodes. It has been observed that when the cells are dismantled following extensive cycling, some lead metal remains on the negative electrode. Clearly, if either Pb or PbO_2 deposition/dissolution proceed with a greater efficiency than the other, a build up of this material will occur on the electrode surface. From preliminary studies it has been noted that Pb deposition and subsequent oxidation occur with greater efficiency when studying the individual electrode couples. An investigation of methods for removing any excess lead is undertaken in this chapter.

Unless otherwise stated the cell was assembled according to a standard specification. New, type II (Ni foam) and type IV (scraped RVC) electrodes were used as the positive and negative plates respectively. A thermostated reservoir (298 K) containing an electrolyte, initially comprising $Pb(CH_3SO_3)_2$ (1.5 mol dm^{-3}) in aqueous CH_3SO_3H (0.9

mol dm^{-3}), supplied the cell. The interelectrode spacing within the flow cell was set at 0.4 cm and the electrolyte pumped such that the linear flow rate across the electrodes' surface was 10 cm s^{-1}. Electrical contact to the electrodes was made using *Method C*: wire strands melted into the core plate and sealed with epoxy resin.

5.2 Extended Cycling

5.2.1 Number of Cycles: The cell was subjected to a series of 84 charge/discharge cycles. Each cycle consisted of a 900 s charge, at 20 mA cm^{-2}, followed by discharge to 1.20 V at the same current density. Due to operational constraints the flow cell was operated during the day only and left on open circuit, in the charged state with the pump switched off (electrolyte remaining in the cell) during the night.

Figure 5.1 presents the voltage vs. time profiles for A: the $1^{st} - 6^{th}$ cycles, B: $43^{rd} - 48^{th}$ cycles and C: $79^{th} - 84^{th}$ cycles. During the initial cycles the voltages are characteristic for the flow cell: a constant voltage during the first charge ($\bar{U}$ = 2.03 V) and discharge ($\bar{U}$ = 1.54 V) with a period of reduced voltage appearing during the second ($\bar{U}$ = 1.93 V) and subsequent charges. Over the 84 cycles the period of reduced voltage during charge spreads, resulting in the lowering of the average voltage, although it never completely encompasses the whole charge period.

It is worth noting that the shape of the voltage vs. time plot gradually approaches a reproducible form during the course of cycling. In fact the final 15 cycles were indistinguishable in appearance. The reduced voltage effect during charging leads to the difference between minimum and maximum voltages being 62 mV (84^{th} cycle), compared to 178 mV for the 2^{nd} cycle. The discharge voltage remains steady for the majority of the discharging period with a gradual and smooth decline in the final stages of discharge before a sharp drop at the point when one or both of the electrode materials is exhausted.

Clearly, having such reproducible voltage vs. time characteristics would be very useful in a scaled up system and would enable the batteries' state of charge to be assessed by voltage measurements.

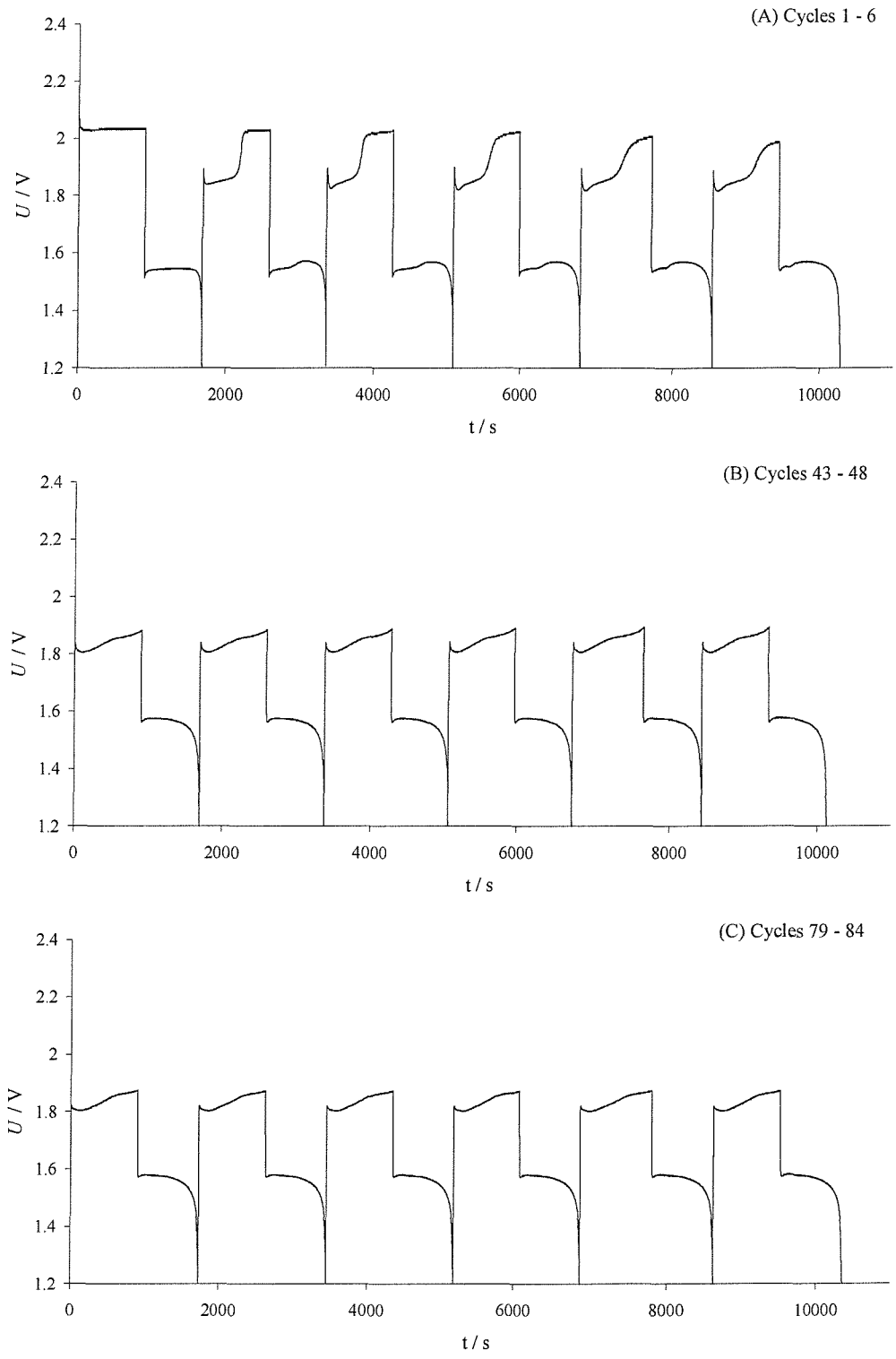

Figure 5.1: *Cell voltage vs. time profiles for a series of charge discharge cycles in the flow cell; (A) cycles 1 – 6, (B) cycles 43 – 48 and (C) cycles 79 – 84.*

Cycle	$\bar{U}_c$ / V	$\bar{U}_d$ / V	$\frac{Q_d}{Q_c}$ / %	$\frac{W_d}{W_c}$ / %
1	2.03	1.54	86	66
2	1.93	1.56	86	70
3	1.94	1.55	92	74
4	1.93	1.55	93	75
5	1.91	1.55	93	75
6	1.90	1.55	93	76
7	1.89	1.55	92	76
8	1.89	1.55	92	76
9	1.88	1.55	92	76
10	1.87	1.55	91	75
24	1.87	1.55	88	73
44	1.84	1.56	88	74
64	1.84	1.56	90	76
84	1.84	1.56	92	78

Table 5.1: *Date from a series of 84 charge / discharge cycles performed in the flow cell. Electrodes: type II (negative plate) and type IV (positive plate). Temperature: 298 K. Interelectrode gap: 0.4 cm, flow rate: 10 cm s^{-1}. Electrolyte: $Pb(CH_3SO_3)_2$ (1.5 mol dm^{-3}) in aqueous CH_3SO_3H (0.9 mol dm^{-3}).*

Voltage and efficiency data for a selection of the cycles is presented in table 5.1. It can be seen that over the course of the 84 cycles the average charge voltage gradually decreases to a stable 1.84 V, circa 100 mV lower than during the initial cycles. The average discharge voltage increases slightly, from the first few cycles, to a steady 1.56 V during the last 40 cycles. The coulombic efficiency increases over the first half dozen cycles but then slowly drops from 93 % (cycle 6) to 88 % (cycle 44). However, from the half way point in the series of cycles the coulombic efficiency steadily increases to 92 % for the final few cycles. This pattern is repeated with the energy efficiency with the final few cycles returning a steady value of 78 %. In fact constant values were recorded for the average

voltages, coulombic and energy efficiencies over the final 15 cycles. This further confirms that with repeated cycling, using a constant current, the cell performance reaches equilibrium, giving repeatable and reliable responses.

5.2.2 Extending the Charge/Discharge Time Periods: The flow cell was fitted with two type III electrodes and assembled with an interelectrode spacing of 1.6 cm. Electrical connection was made via *Method A* (screw contact). A charging current density of 20 mA cm^{-2} was then applied for 6 hours. Figure 5.2 gives the voltage vs. time profile. Following a slight overvoltage peak the voltage drops off and remains steady throughout the charge.

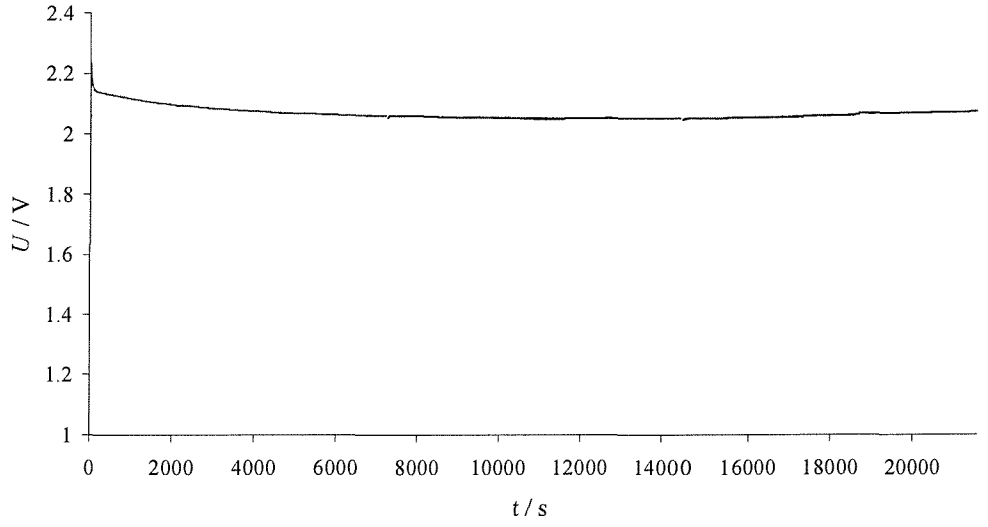

Figure 5.2: *Voltage vs. time profile for a 6 hour charge within the flow cell. Both electrodes were type III and the interelectrode gap was 1.6 cm. Temperature: 298 K. Interelectrode gap: 0.4 cm, flow rate: 10 cm* s^{-1}*. Electrolyte:* $Pb(CH_3SO_3)_2$ *(1.5 mol* dm^{-3}*) in aqueous* CH_3SO_3H *(0.9 mol* dm^{-3}*).*

The flow cell was assembled using the standard procedure (see 5.1 introduction) and a series of 4 charge / discharge cycles performed. Each cycle consisted of a 1 hour charge at 20 mA cm^{-2} followed by discharge, at the same current density, until the voltage reached 1.20 V. The voltage vs. time plot is presented in figure 5.3. The form of the plot is essentially the same as with cycles of shorter length; a steady voltage during the initial

charge (2.04 V) followed by a discharge period in which the voltage is 1.54 V. Each subsequent discharge is the same. The second and subsequent charges, however, have a period of lower voltage (circa 1.81 V) before the voltage gradually rises to 1.97 V. This has been previously discussed although it is interesting to note that the period of lowered voltage extends to cover approximately half of the total charge time. This can be seen as an advantage as the lowered voltage gives a better energy efficiency than would be expected if the voltage was at the higher level throughout the charge. The coulombic efficiencies for the 4 cycles are 90 %, 88%, 91% and 86 % respectively. This is encouraging as it shows that even though much thicker layers of Pb / PbO_2 are being deposited / stripped and hence a larger quantity of energy stored/released, there is no deterioration in the efficiency of the two electrode reactions.

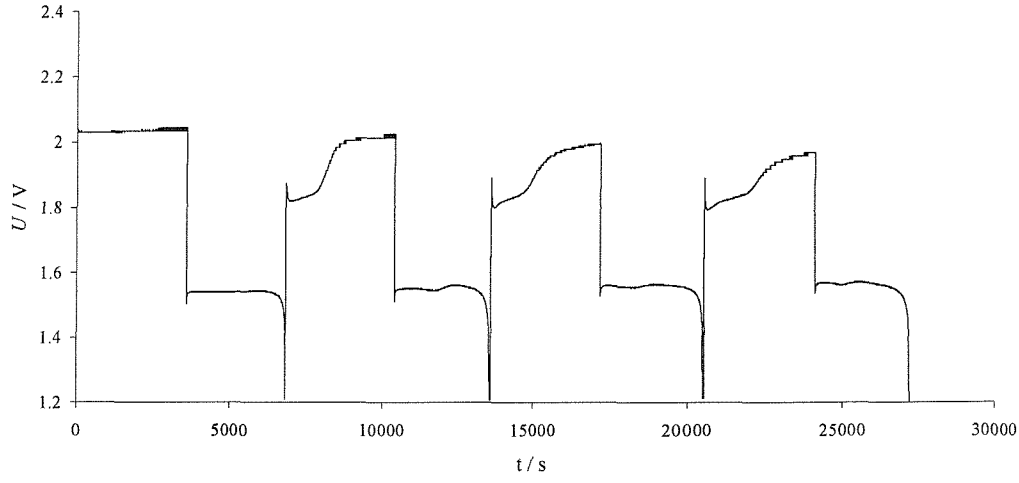

Figure 5.3: *Voltage vs. time plot for 4 cycles of the flow cell. Each cycle consisted of a 1 hour charge at 20 mA* cm^{-2} *followed by discharge, at the same current density, until the voltage reached 1.20 V. Electrodes: type II (negative plate) and type IV (positive plate). Temperature: 298 K. Interelectrode gap: 0.4 cm, flow rate: 10 cm* s^{-1}*. Electrolyte:* $Pb(CH_3SO_3)_2$ *(1.5 mol* dm^{-3}*) in aqueous* CH_3SO_3H *(0.9 mol* dm^{-3}*).*

The cell, with a 4 mm interelectrode gap was assembled with the intention of performing a 4 hour charge at 20 mA cm^{-2} followed by discharge, at the same current density. However, partway through the charge, abnormal cell voltages were observed. The charge was halted and the cell discharged. The abnormal voltage response was attributed to

dendritic lead growths forming and bridging the interelectrode gap, shorting the cell. The voltage vs. time plot is presented in figure 5.4. Discounting the region of irregular voltages, the coulombic efficiency for the discharge is 88 %, showing that when shorting occurs no long term damage is done to the Pb / PbO_2 deposits or battery performance (other than the energy lost during the period in which shorting occurs).

It seams that charging the flow cell over extended periods of time presents the risk of Pb dendrites forming. This is expected to be more problematic with narrow intereclectrode gaps, such as the 0.4 cm gap used in this experiment and with high charging currents. If the battery system is to be operated on a large scale the formation of rough or dendritic deposits must be minimised. This is dealt with in chapter 6.

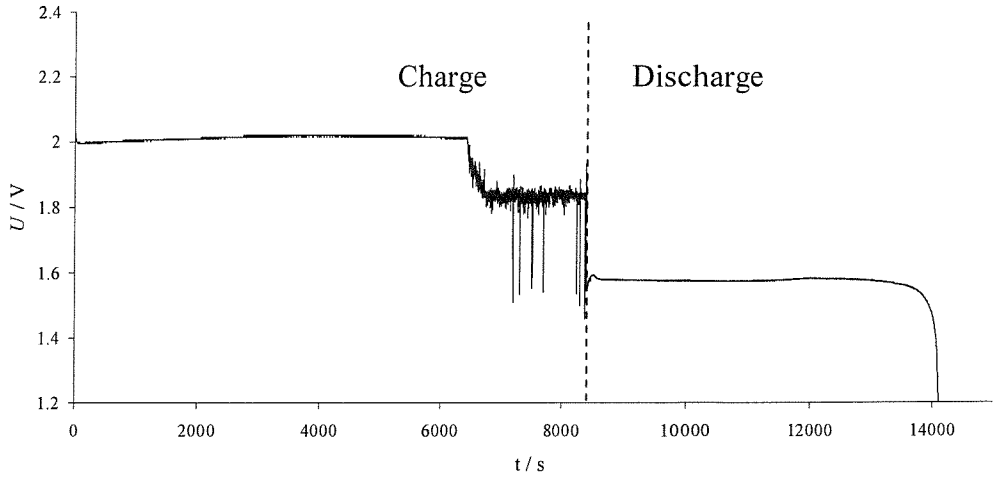

Figure 5.4: *Voltage vs. time data for a charge / discharge (j = 20 mA cm^{-2}) of the flow cell. Electrodes: type II (negative plate) and type IV (positive plate). Temperature: 298 K. Interelectrode gap: 0.4 cm, flow rate: 10 cm s^{-1}. Electrolyte: $Pb(CH_3SO_3)_2$ (1.5 mol dm^{-3}) in aqueous CH_3SO_3H (0.9 mol dm^{-3}).*

5.3 Current Density

A series of experiments were performed within the flow cell in which the same current density was used for charge and discharge. The flow cell was assembled as set out

in section 5.1 at the beginning of this chapter. Each experiment consisted of 6 charge/discharge cycles, with each cycle comprising a 900 s charge followed by discharge to 1.20 V. Table 5.2 presents average voltage and efficiency data for each experiment. It can be seen that increases in the rate of charge / discharge are at the expense of higher overpotentials and lower energy efficiencies. The coulombic efficiency is relatively unaffected as it is only dependent on the length of time that the charging and discharging currents are applied for and independent of the cell voltage.

j / mA cm^{-2}	Cycle	$\bar{U}_c$ / V	$\bar{U}_d$ / V	$\frac{Q_d}{Q_c}$ / %	$\frac{W_d}{W_c}$ / %
20	1	2.03	1.54	86	66
	2	1.93	1.56	86	70
	3	1.93	1.55	92	74
	4	1.93	1.55	93	75
	5	1.91	1.55	93	75
	6	1.90	1.55	93	76
40	1	2.08	1.49	84	60
	2	1.99	1.50	84	63
	3	1.98	1.51	89	67
	4	1.97	1.51	90	69
	5	1.95	1.51	89	69
	6	1.93	1.51	89	70
60	1	2.20	1.42	71	46
	2	2.09	1.43	85	59
	3	2.07	1.43	87	60
	4	2.05	1.44	88	62
	5	2.02	1.44	89	63
	6	1.99	1.46	91	67

Table 5.2: *Cycling data for the flow cell, operated at various current densities. Each cycle involved a 900 s charge followed by discharge to 1.20 V. Electrodes: type II (negative plate) and type IV (positive plate). Temperature: 298 K. Interelectrode gap: 0.4 cm, flow rate: 10 cm s^{-1}. Electrolyte: $Pb(CH_3SO_3)_2$ (1.5 mol dm^{-3}) in aqueous CH_3SO_3H (0.9 mol dm^{-3}).*

Three experiments were performed in the flow cell, using current densities of 10 mA cm^{-2}, 20 mA cm^{-2} and 40 mA cm^{-2}. Each experiment consisted of 4 cycles, each cycle comprising a 1 hour charge followed by discharge to 1.20 V. Figure 5.5 gives the voltage vs. time profiles for the cycles carried out at 10 mA cm^{-2} and 40 mA cm^{-2}. Table 5.3 gives cell voltage and efficiency data for the three current densities. As expected, the results mirror those obtained with shorter cycle lengths: increasing the current density leads to

increased overpotentials associated with the electrode couples and a lowering in the energy efficiency.

j / mA cm^{-2}	Cycle	$\bar{U}_c$ / V	$\bar{U}_d$ / V	$\frac{Q_d}{Q_c}$ / %	$\frac{W_d}{W_c}$ / %
10	1	1.95	1.60	88	73
	2	1.92	1.59	85	70
	3	1.91	1.60	88	74
	4	1.90	1.60	90	76
20	1	2.04	1.54	90	68
	2	1.95	1.55	88	70
	3	1.92	1.56	91	74
	4	1.89	1.56	86	71
40	1	2.13	1.50	84	59
	2	1.99	1.51	92	70
	3	2.00	1.51	88	66
	4	1.96	1.52	90	70

Table 5.3: *Efficiency and average voltage data for cycling of the cell at various current densities. Each cycle involved a 1 hour charge followed by discharge to 1.20 V. Electrodes: type II (negative plate) and type IV (positive plate). Temperature: 298 K. Interelectrode gap: 0.4 cm, flow rate: 10 cm s^{-1}. Electrolyte: $Pb(CH_3SO_3)_2$ (1.5 mol dm^{-3}) in aqueous CH_3SO_3H (0.9 mol dm^{-3}).*

The form of the Pb / PbO_2 deposits and the energy efficiency should be directly linked to the current density during charge, indeed poorer quality deposits (powdery and dendritic) were observed at current densities above 40 mA cm^{-2} and constant current charging/discharging of the cell led to the accumulation of significant quantities of particulate sediment in the reservoir. This is believed to be primarily from the PbO_2 electrode due to its deep red / black colouring. However the current density during discharge would be expected to have a lesser effect on the cell performance. To test this, the cell was assembled as set out in section 5.1 and subjected to a series of 1 hour charges (j = 20 mA cm^{-2}) followed by discharge at various current densities. Figure 5.6 presents the voltage vs. time profiles for the discharges along with a table giving voltage and efficiency data for each of the cycles. As expected, the average discharge voltage drops with increasing current density. Encouragingly though, even with a rate of discharge up to 60 mA cm^{-2}, the coulombic and energy efficiencies of the discharges only deteriorate slightly.

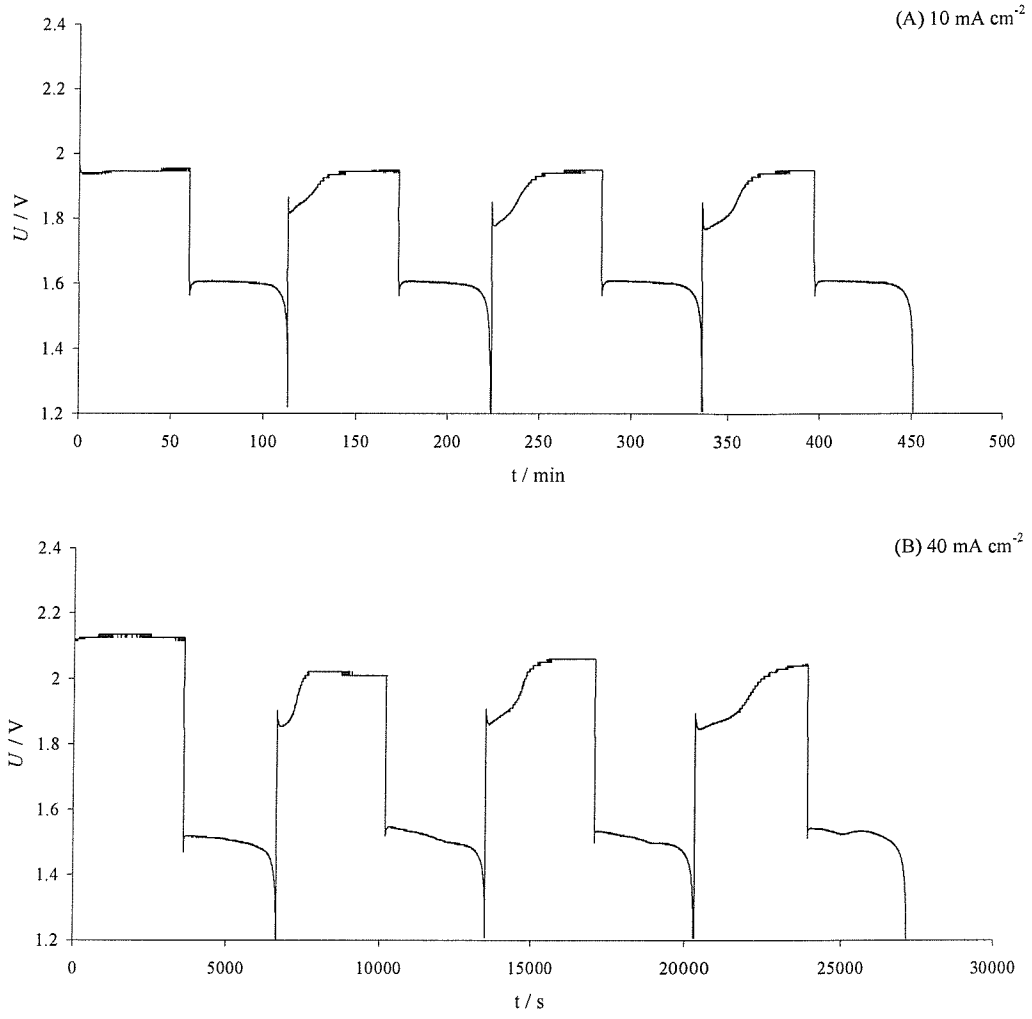

Figure 5.5: *Voltage vs. time data for cycling of the cell using current denisites of (A) 10 mA cm^{-2} and (B) 40 mA cm^{-2}. Each cycle consisted of a 1 hour charge followed by discharge until the voltage reached 1.20 V. Electrodes: type II (negative plate) and type IV (positive plate). Temperature: 298 K. Interelectrode gap: 0.4 cm, flow rate: 10 cm s^{-1}. Electrolyte: $Pb(CH_3SO_3)_2$ (1.5 mol dm^{-3}) in aqueous CH_3SO_3H (0.9 mol dm^{-3}).*

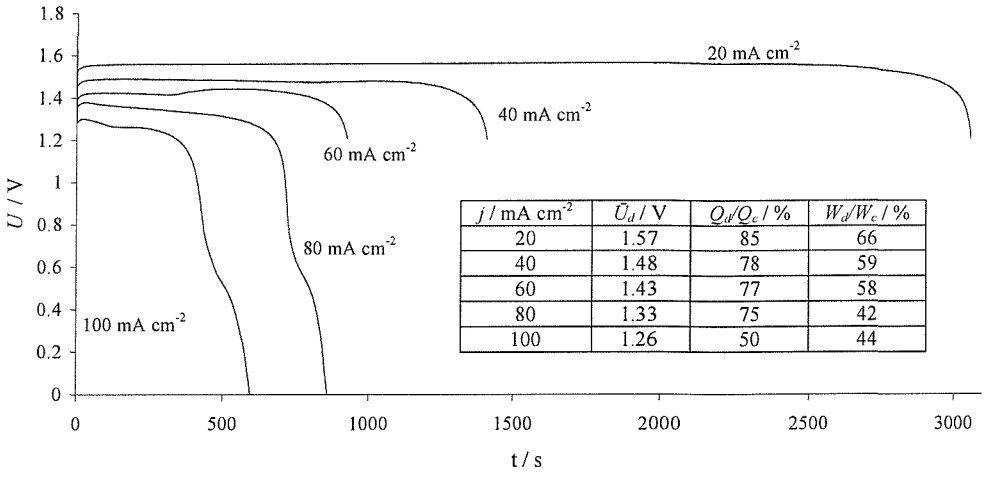

j / mA cm^{-2}	$\bar{U}_d$ / V	Q_d/Q_c / %	W_d/W_c / %
20	1.57	85	66
40	1.48	78	59
60	1.43	77	58
80	1.33	75	42
100	1.26	50	44

Figure 5.6: *Cell voltage vs. time plots during discharge as a function of current density. In each case the cell was charged at 20 mA cm^{-2} for 1 hour. Flow cell fitted with type II (negative plate) and type IV (positive plate) electrodes. Interelctrode gap: 0.4 cm. Temperature: 298 K. Linear flow rte of electrolyte: 10 cm s^{-1}. Electrolyte: $Pb(CH_3SO_3)_2$ (1.5 mol dm^{-3}) in aqueous CH_3SO_3H (0.9 mol dm^{-3}).*

5.4 Temperature

A series of experiments was performed in the flow cell at various temperatures between 273 K and 333 K. Each experiment was carried out using a charge/discharge current density of 20 mA cm^{-2} and comprised 6 cycles. Each cycle consisted of a 900 s charge followed by discharge to 1.20 V. Table 5.4 presents the cell voltage and efficiency data from the 6th cycle at each temperature. With increasing temperature there is a significant decrease in the overpotential during charging and a slight decrease in the overpotential during discharging of the cell. In the range 237 K to 313 K there is little change in the charge and energy efficiencies. However, at higher temperatures there is a considerable decrease in the charge efficiencies and this may be due to some soluble Pb^{4+} species at the higher temperatures.

Figure 5.7 shows the voltage vs. time profiles for the experiments carried out at 273 K, 313 K and 333 K.

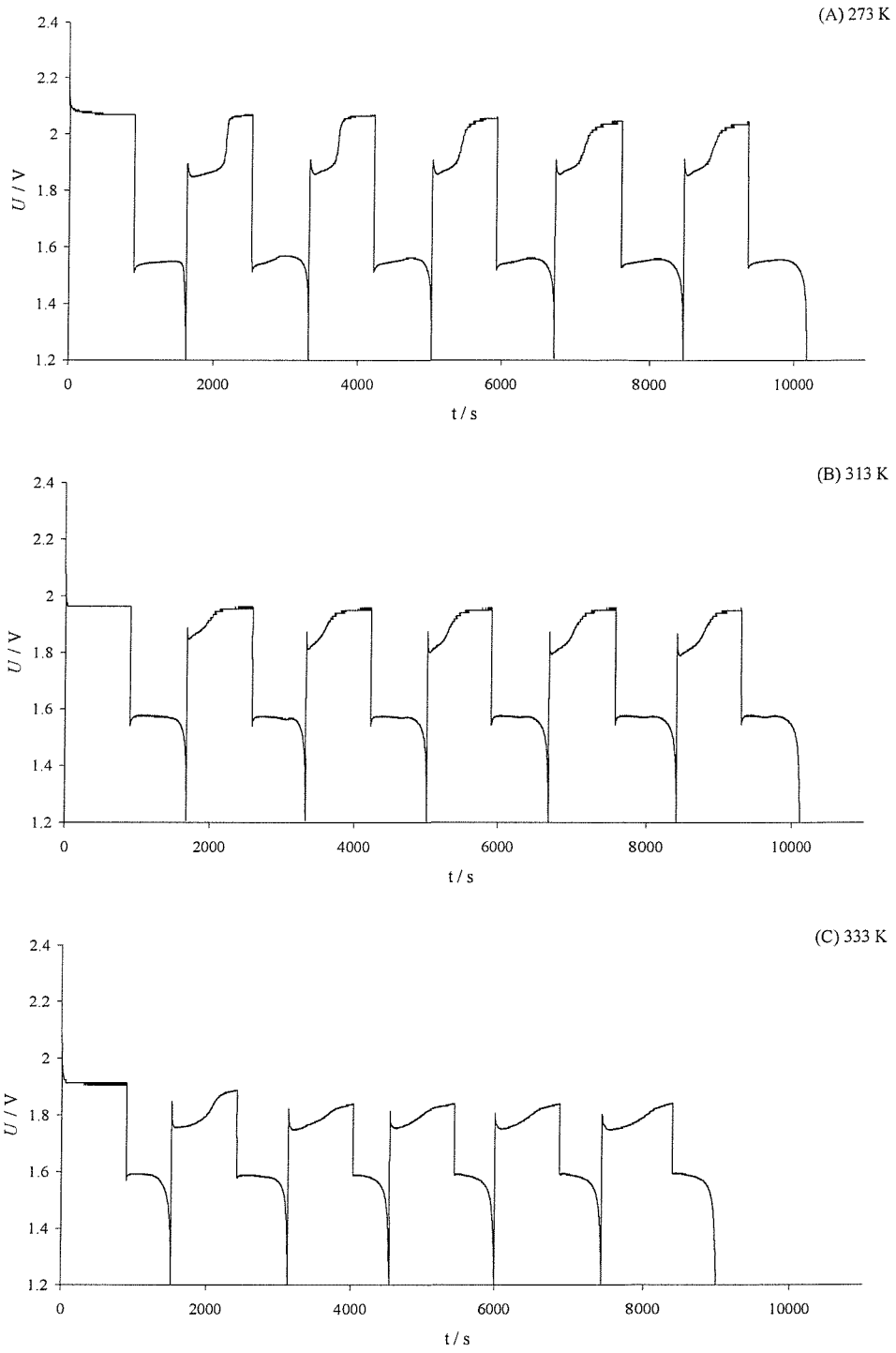

Figure 5.7: *Voltage vs. time data for cycling of the cell at temperatures of (A) 273 K, (B) 313 K and (C) 333 K. Each cycle consisted of a 900 s charge followed by discharge until the voltage reached 1.20 V. Electrodes: type II (negative plate) and type IV (positive plate). Temperature: 298 K. Interelectrode gap: 0.4 cm, flow rate: 10 cm s^{-1}. Electrolyte: $Pb(CH_3SO_3)_2$ (1.5 mol dm^{-3}) in aqueous CH_3SO_3H (0.9 mol dm^{-3}).*

T / K	$\bar{U}_c$ / V	$\bar{U}_d$ / V	$\frac{Q_d}{Q_c}$ / %	$\frac{W_d}{W_c}$ / %
273	2.04	1.54	91	72
298	2.01	1.54	93	76
313	1.95	1.56	90	74
323	1.89	1.57	77	67
333	1.84	1.57	67	59

Table 5.4: *Cell performance as a function of temperature. Data from the 6th cycle. Electrodes: type II (negative plate) and type IV (positive plate). Temperature: 298 K. Interelectrode gap: 0.4 cm, flow rate: 10 cm s^{-1}. Electrolyte: $Pb(CH_3SO_3)_2$ (1.5 mol dm^{-3}) in aqueous CH_3SO_3H (0.9 mol dm^{-3}).*

5.5 State of Charge

5.5.1 Current Density as a Function of Cell Voltage: The influence on the state of charge of the battery was investigated by carrying out experiments using 5 electrolytes of varying composition, see table 5.5. The composition of each electrolyte was calculated assuming that the initial electrolyte consisted of: $Pb(CH_3SO_3)_2$ (1.5 mol dm^{-3}) in aqueous CH_3SO_3H (0.9 mol dm^{-3}), and that the concentrations varied according to equation *43* during charging.

Electrolyte	Concentration / mol dm^{-3}	
	$Pb(CH_3SO_3)_2$	CH_3SO_3H
A	1.5	0.9
B	0.5	2.9
C	0.1	3.7
D	0.05	3.8
E	0.01	3.8

Table 5.5: *Concentration of $Pb(CH_3SO_3)_2$ and CH_3SO_3H in various electrolyte solutions.*

$$2H_2O + 2Pb^{2+} \rightarrow Pb + PbO_2 + 4H^+ \qquad (43)$$

The cell was assembled according to the procedure in section 5.1 and charged for 2 hours (j = 20 mA cm^{-2}) using solution *A*. The initial electrolyte was then drained and in turn replaced with each of the electrolytes *A* to *E*. With each solution the cell charge characteristic was measured by ramping the current from zero to 100 mA cm^{-2} at a scan rate of 0.5 mA cm^{-2} s^{-1} while monitoring the voltage. The discharge characteristic was recorded in the same manner, with the direction of current flow reversed. Figure 5.8 presents the current vs. voltage plots for each solution. It can be seen that the open circuit potential (when j = 0) for the cell shifts significantly to more positive potentials as the cell approaches a higher state of charge i.e. as the Pb^{2+} concentration decreases and the acidity increases from electrolyte *A* to *E*. This is to be expected from the Nernst equation for the cell (equation *44*)

$$E_{Cell} = E^0_{Pb^{2+}/PbO_2} - E^0_{Pb^{2+}/Pb} - \frac{2.3RT}{F}(\log c_{Pb^{2+}}) + \frac{4.6RT}{F}(\log c_{H^+}) \qquad (44)$$

where $E^0_{Pb^{2+}/PbO_2}$ and $E^0_{Pb^{2+}/Pb}$ are the formal potentials for the two electrode couples. It has been assumed that the solid phases and water are in their standard states and that the concentrations of the aqueous species are equal to their activities. The increase in open circuit potential as the battery is "charged" does not affect the efficiency of energy storage. It is the coulombic efficiency and overpotential associated with each electrode reaction along with *IR* drop through the cell that determines the energy efficiency.

With each of the electrolyte solutions, the overpotential associated with charging the battery increases as the current is ramped to higher values. A significant contribution arises from the *IR* drop through the electrolyte. In fact, using conductivity values reported in chapter 3: figure 3.2, the *IR* drop due to the electrolyte is circa 100 mV at a current density of 100 mA cm^{-2}. Electrolyte solution *E* showed particularly high overpotentials and even at low current densities the potential was significantly higher than the open circuit value. It should be noted that mass transport of Pb^{2+} to the electrode surfaces is likely to become a factor for the low $Pb(CH_3SO_3)_2$ containing electrolytes. It is therefore probable that a

portion of the current is being used in unwanted reactions such as O_2 and H_2 production, indeed at high current densities gas evolution was evident with solutions having low $Pb(CH_3SO_3)_2$ concentrations.

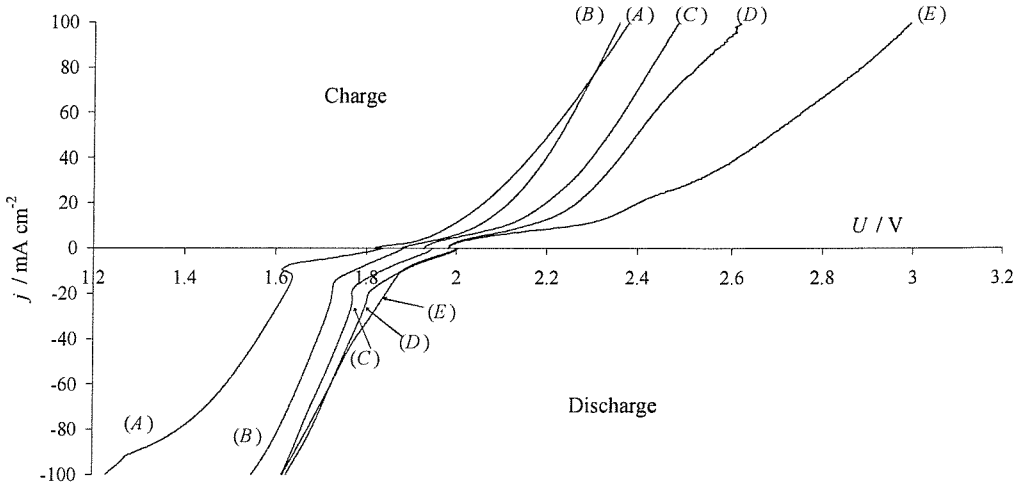

Figure 5.8: *Current density vs. cell voltage characteristics as a function of electrolyte composition. Cell charged for 1 hour at 20 mA cm^{-2}. using electrolyte A. Electrolyte then changed, I turn, to that shown. Curves recorded by ramping the current at 0.5 mA cm^{-2} s^{-1} from the open circuit potential. Temperature: 298 K. Electrolyte flow rate: 10 cm s^{-1}.*

Applying discharge currents there are only relatively small differences between the overpotentials of the electrolytes *B* to *E*. This is expected due to there being no mass transport limitations associated with the solid reactants at the electrode plates. The overpotentials are higher with the high $Pb(CH_3SO_3)_2$, low CH_3SO_3H containing solutions, most notably electrolyte *A*. This is likely to be caused by a combination of higher *IR* drop (lower conductivity of the high $Pb(CH_3SO_3)_2$, low CH_3SO_3H containing electrolytes) and proton depletion at the surface and in pores within the PbO_2 deposit.

In summary, electrolyte solutions *A* to *C* produced quite reasonable current vs. voltage characteristics within the flow cell and it should be possible to charge the battery until the $Pb(CH_3SO_3)_2$ concentration in the electrolyte has dropped to at least 0.1 mol dm^{-3}. The ability to deplete the $Pb(CH_3SO_3)_2$ concentration by 1.4 mol dm^{-3} gives a maximum energy storage capacity for the battery of 38 Ah dm^{-3}.

5.5.2 Cell Cycling: A further characterisation of battery performance at different states of charge was performed using electrolyte solutions *A*, *B* and *C*. Each experiment involved a series of ten charge / discharge cycles. Each cycle consisted of a 900 s charge at 20 mA cm^{-2} followed by discharge at the same current density until the voltage reached 1.20 V. Following the ten cycles a final 900 s charge was applied to the battery and the open circuit potential recorded. Figure 5.9 presents the voltage vs. time profiles for the three experiments.

As with the current ramping experiment, the open circuit potential of the cell increases as the proton concentration in the electrolyte increases and the $Pb(CH_3SO_3)_2$ concentration decreases. Table 5.6 gives performance data, for the three electrolyte solutions, from the 6^{th} cycle (when the cell response has reached a steady state).

The efficiency of the cell only drops slightly with solution *B*, and only moderately with solution *C*. It is also interesting to note that the period of reduced voltage during sequential charges becomes shorter with electrolytes *B* and *C*. The open circuit potentials given in table 5.6 are significantly lower than would be read from figure 5.8. In the current ramping experiment the open circuit potentials were observed immediately following charging of the cell. The values in table 5.6 were recorded after the cell had been left on open circuit for a period of time. It has been found that following charging or discharging the batteries open circuit potential takes time to reach a steady value. This is can be explained if, close to the electrode surface or in solution filled pores within the deposited layers, the electrolyte is of slightly different composition to the bulk solution. Diffusion, which is a slow process, is needed to equilibrate these areas with the bulk electrolyte solution.

Electrolyte	Open Circuit Voltage after Charge / V	$\frac{Q_d}{Q_c}$ / %	$\frac{W_d}{W_c}$ / %
A	1.71	93	76
B	1.78	86	72
C	1.83	63	54

Table 5.6: *Cell performance data (from the 6^{th} cycle) with three electrolytes modelling different states of charge for the battery. Temperature: 298 K. Electrolyte flow rate: 10 cm s^{-1}.*

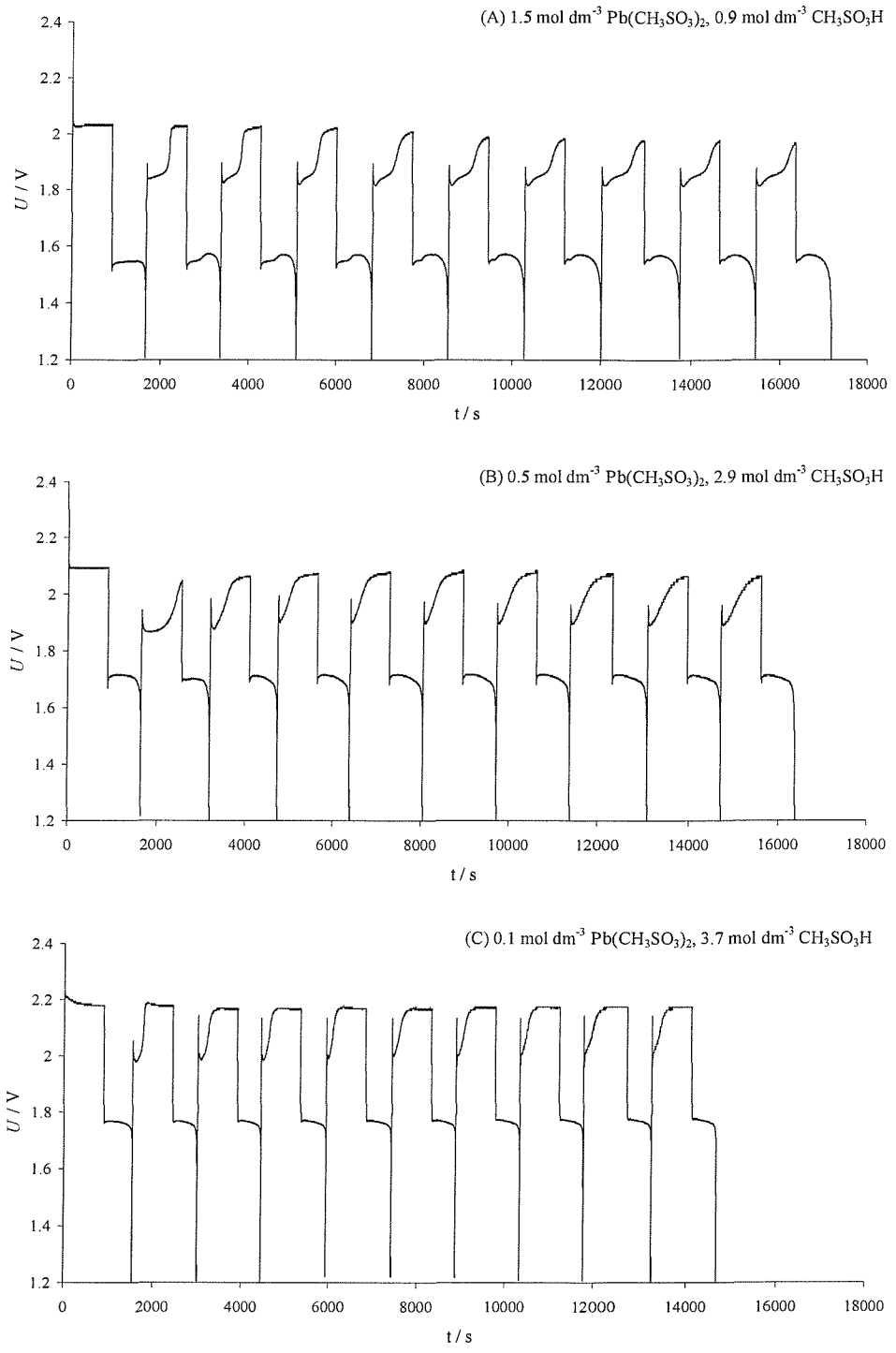

Figure 5.9: *Cell voltage vs. time profiles for a series of charge discharge cycles in the flow cell; (A) Electrolyte: $PbCH_3SO_3)_2$ (1.5 mol dm^{-3}) CH_3SO_3H (0.9 mol dm^{-3}), (B) Electrolyte: $PbCH_3SO_3)_2$ (0.5 mol dm^{-3}) CH_3SO_3H (2.9 mol dm^{-3}) and (C) Electrolyte: $Pb(CH_3SO_3)_2$ (0.1 mol dm^{-3}) CH_3SO_3H (3.7 mol dm^{-3}).*

Using each of the electrolytes, *A*, *B* and *C*, the cell was assembled as set out in section 5.1. A 1 hour charge (j = 20 mA cm^{-2}) was applied following which the battery was left on open circuit and the potential recorded as a function of time. The electrolyte flow rate was maintained at 10 cm s^{-1} through the open circuit period. Figure 5.10 compares the open circuit potentials for each of the electrolytes. Switching form electrolyte solution *A* to solution *B* results in an increase in open circuit potential of 80 mV (c.f. 76 mV calculated with equation 5:1) while switching between solutions *A* and *B* results in an increase in open circuit potential of 120 mV (c.f. 126 mV calculated using equation 5:1). Clearly the experimental results are close enough to values calculated using equation 5:1 to justify the assumptions made in its derivation.

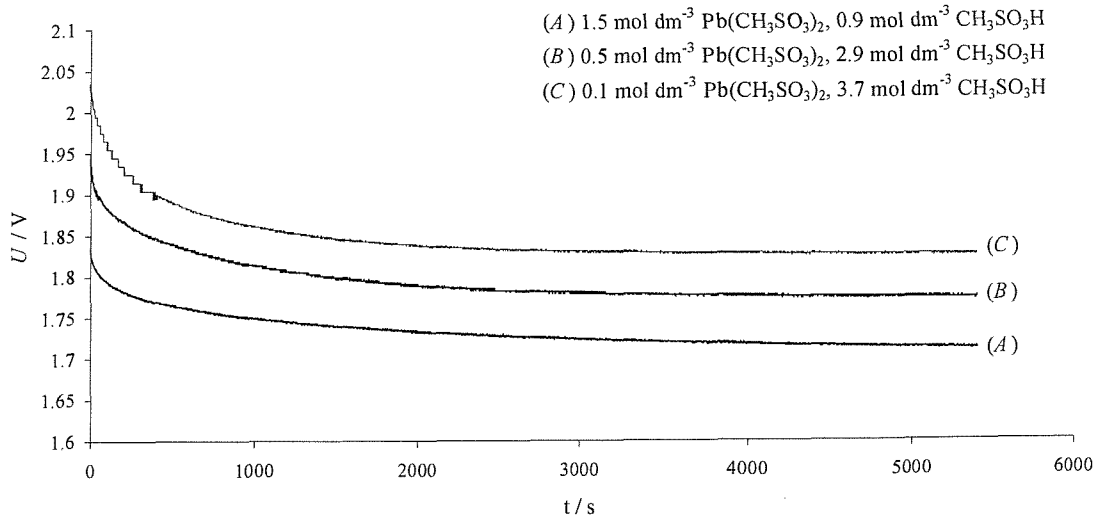

Figure 5.10: *Cell potential vs. time characteristics as a function of electrolyte composition. Cell charged for 1 hour at 20 mA cm^{-2}. Temperature: 298 K. Electrolyte flow rate: 10 cm s^{-1}.*

5.6 Rejuvenating the Electrodes and Balancing the Cell Chemistry

5.6.1 Rejuvenation of Electrodes: The flow cell was fitted with two new, type III electrodes and subjected to a series of 12 charge / discharge cycles. Each cycle consisted of a 900 s charge at 20 mA cm^{-2} followed by discharge to 1.20 V at the same current density. At the end of the 6^{th} complete cycle the electrodes were swapped and a further 6 cycles carried out.

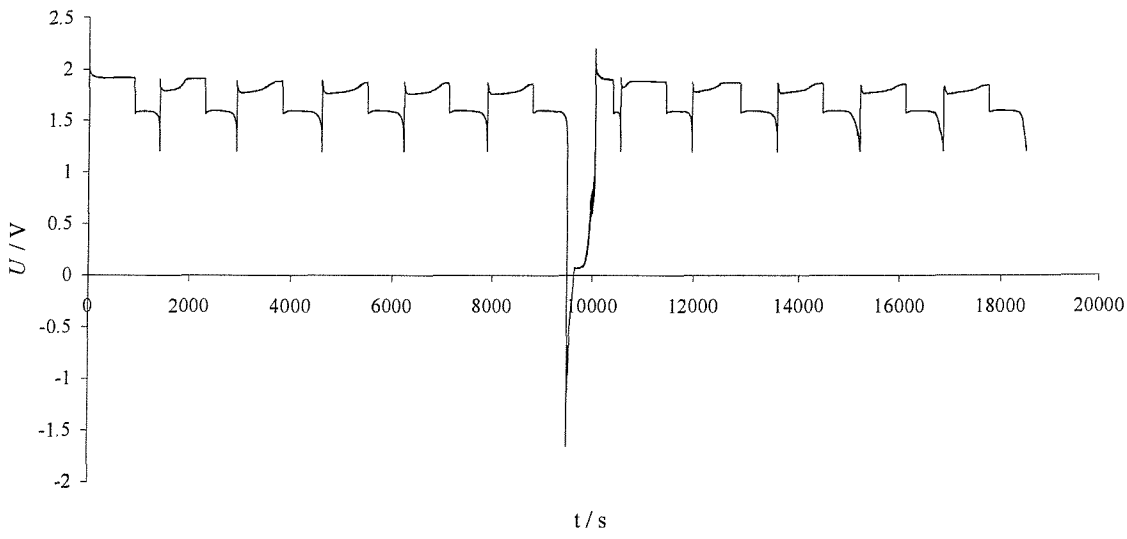

Figure 5.11: *Voltage vs. time profile for twelve charge / discharge cycles of the flow cell. Between the 6^{th} and 7^{th} cycles the electrodes were switched. Type III electrodes were used for both plate. Electrolyte initially $Pb(CH_3SO_3)_2$ (1.5 mol dm^{-3}) in aqueous CH_3SO_3H (0.9 mol dm^{-3}). Temperature: 298 K. Linear flow rate across electrodes' surface: 10 cm s^{-1}.*

Figure 5.11 shows the voltage vs. time profile for the 12 cycles. The characteristics of the first 6 cycles are as expected. During the first charge following reversal of the electrode plates there is a sharp voltage peak to circa -1.5 V before a period of steady voltage (80 mV). During this time there is excess Pb is being stripped from the old negative plate and simultaneously deposited on the new negative plate. After 170 s the voltage

rapidly increases and following an overvoltage peak, the voltage settles at 1.90 V, the expected charge voltage of the battery. The coulombic efficiency of the discharge is very low, however the efficiencies and voltages of subsequent cycles rapidly return to the expected values.

Clearly this experiment does not solve the problem of removing excess Pb deposits, it does however show that the electrodes can be completely stripped and reused without detriment to the long term efficiency of the battery. Also, reversal of the electrodes used in conjunction with other techniques may offer a solution to the removal of excess Pb from the negative electrode. It is also worth noting that the 170 s period in which Pb was being transferred from one electrode to the other corresponds to 3 % of the total Pb deposited in the previous 6 cycles.

5.6.2 Oxidation of Lead: Oxygen is a potential oxidant for Pb in the battery system and dissolution should occur via the reaction:

$$2Pb + 4H^{+} + O_2 \rightarrow 2Pb^{2+} + 2H_2O \qquad (45)$$

Periodic dissolution of excess Pb, using O_2 saturated electrolyte would enable the removal of unwanted deposits without the irreversible addition of chemicals to the battery system.

The cell was assembled according to the procedure set out in section 5.1 and subjected to a 1800 s charge at 40 mA cm^{-2}. After completion of the charge the electrolyte was drained, the PbO_2 electrode removed and the cell supplied with 40 cm^3 of an electrolyte solution comprising aqueous CH_3SO_3H (0.9 mol dm^{-3}). A vigorous stream of O_2 gas was passed through the electrolyte within the reservoir and the solution pumped through the cell using a flow rate of 10 cm s^{-1}. The concentration of Pb^{2+} in the acid solution was monitored as a function of time using a vitreous carbon rotating disc electrode (along with reference and counter electrodes) in the reservoir and a calibration plot of limiting current density vs. Pb^{2+} concentration. The resulting concentration vs. time plot is shown in figure 5.12.

It can be seen that the Pb^{2+} in solution increases smoothly with time and fully dissolves over a period of 230 minutes. The use of initially Pb free electrolyte was to aid the analyses of Pb dissolution and it is not thought that the high levels of Pb in the battery electrolyte will slow down the Pb oxidation process. It is possible that the rate of dissolution could be enhanced by increasing the temperature or supply of oxygen.

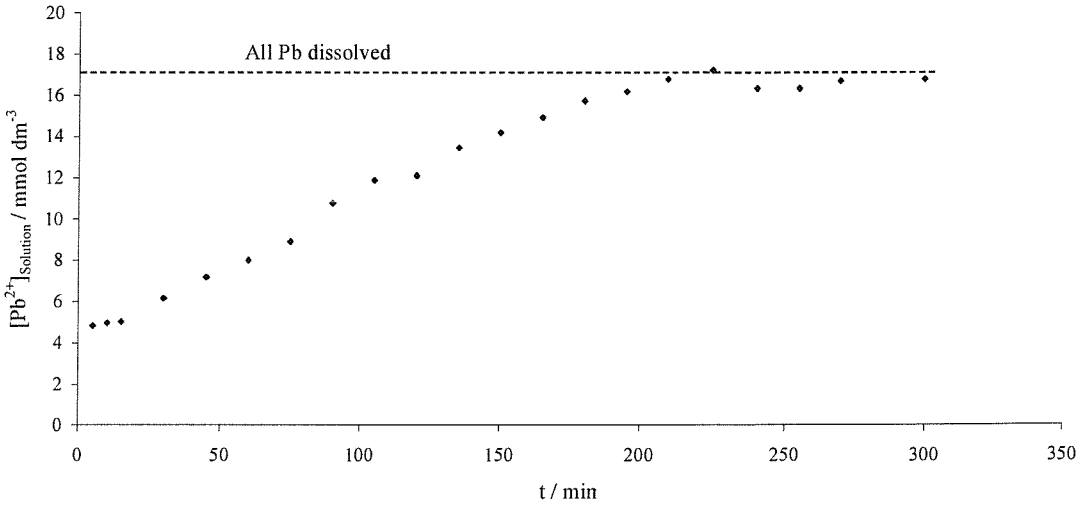

Figure 5.12: *Concentration of Pb^{2+} in solution as a function of time when flowing O_2 saturated aqueous solution of CH_3SO_3H (0.9 mol dm^{-3}) through the cell on open circuit after removal of the PbO_2 electrode. The lead was deposited with a current density of 40 mA cm^{-2} for 1800 s. Temperature 298 K. Electrolyte flow rate 10 cm s^{-1}.*

5.6.3 Self Discharge of the Battery: Of course, during normal operation of the battery, dissolution of Pb by O_2 or any other mechanism of self discharge (for example reduction of PbO_2, forming insoluble Pb^{2+} species) is obviously unwanted. To test for self discharge, the cell was assembled according to the procedure in section 5.1 and charged for 1 hour (j = 20 mA cm^{-2}), left on open circuit for 30 minutes, charged for a further 30 minutes (j = 20 mA cm^{-2}), left on open circuit for 30 minutes and finally discharged at 20 mA cm^{-2} until the voltage reached 1.20 V. The voltage vs. time profile for the charge and discharge periods is presented in figure 5.13.

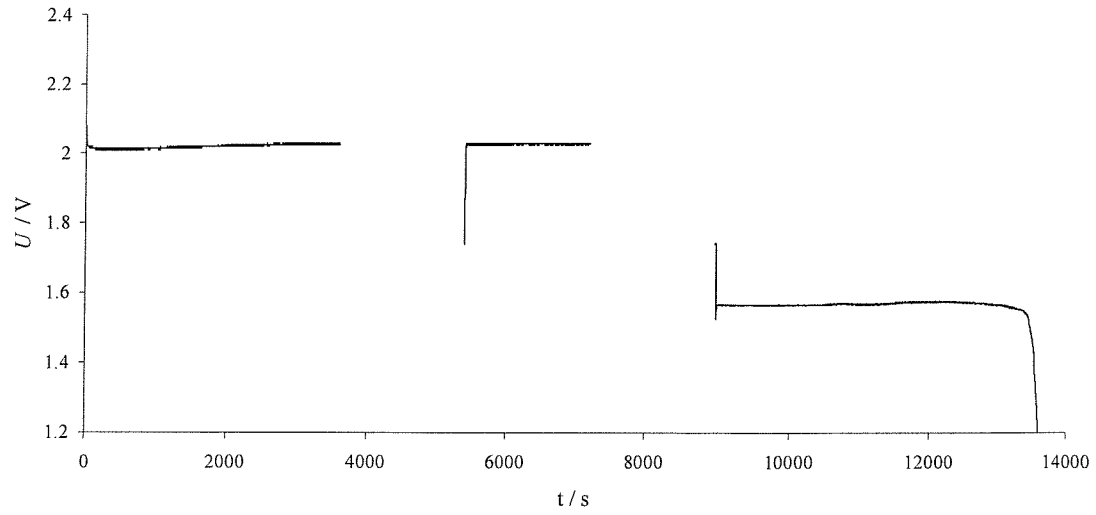

Figure 5.13: *Voltage vs. time profile for charge and discharge of the cell. 1 hour charge, 30 minute open circuit, 30 minute charge, 30 minute open circuit, discharge to 1.20 V. Current density for charge and discharge 20 mA cm^{-2} throughout. Electrolyte initially: $Pb(CH_3SO_3)_2$ (1.5 mol dm^{-3}) in aqueous CH_3SO_3H (0.9 mol dm^{-3}). Temperature: 298 K. Flow rate: 10 cm s^{-1}.*

Following the first open circuit period the voltage vs. time profile for the initial stages of the 30 minute charge showed no sign of reduced voltage, which would have been expected if self discharge at the positive electrode, resulting in formation of insoluble Pb^{4+} species had taken place. Also the coulombic efficiency of the discharge phase was 88 %, the expected value had the cell been discharged immediately following a charge. It can be concluded that no significant self discharge of the battery takes place over time periods up to 30 minutes in length.

Despite no observable self discharge over short time periods, deterioration in cell efficiency is observed when the cell is left on open circuit for long periods of time. The cell was assembled according to the procedure in section 5.1 and subjected to a series of charge/discharge cycles. Each cycle consisted of a 900 s charge at 20 mA cm^{-2} followed by discharge to 1.20 V at the same current density. Following a number of complete cycles, the cell was charged for 900 s at 20 mA cm^{-2} and then left overnight (15 hours) on open circuit, with the electrolyte remaining in the cell but with the pump turned off. After 15 hours the pump was switched back on, the cell discharged and a further series of cycles

performed. The voltage vs. time profiles for: (A) the last discharge before being left on open circuit and (B) the first discharge after being left on open circuit are shown in figure 5.14.

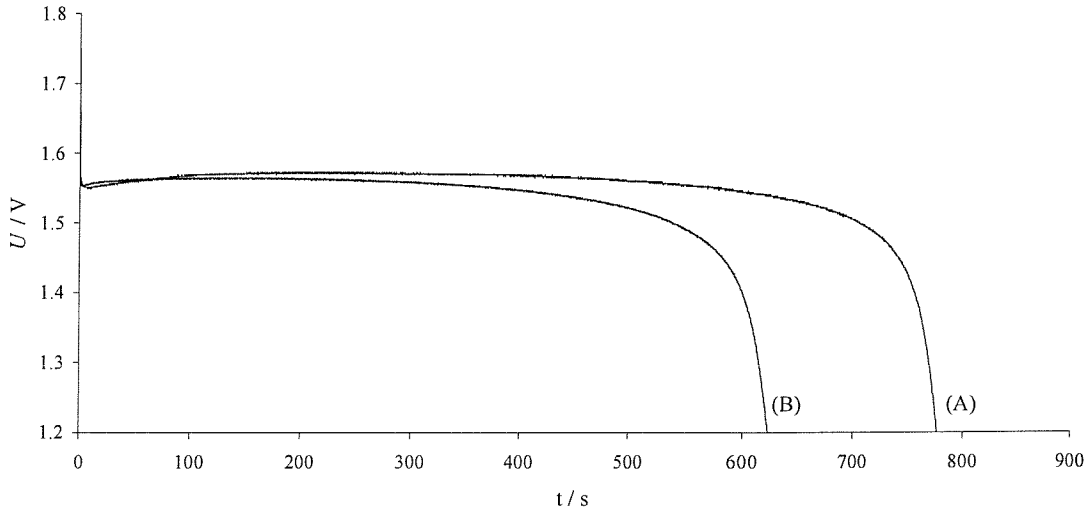

Figure 5.14: *Two discharge profiles form cycles involving a 900 s charge at 20 mA cm^{-2} followed by discharge to 1.20 V at the same current density. (A) Discharge following immediately from the charge. (B) Discharge following 15 hours of open circuit. Electrolyte initially $Pb(CH_3SO_3)_2$ (1.5 mol dm^{-3}) in aqueous CH_3SO_3H (0.9 mol dm^{-3}). Temperature: 298 K. Electrolyte flow rate: 10 cm s^{-1}.*

The coulombic efficiencies for the two discharges are 86 % and 69 % for before and after being left on open circuit respectively. Clearly some self discharge has occurred while the battery was left on open circuit for the extended period of time. However it should be noted that the cell efficiency returned to normal during the second discharge following the open circuit phase.

5.7 Chapter 5 Summary

It has been shown that the flow cell may be repeatedly cycled with high energy efficiency and reproducible and repeatable charge / discharge characteristics. However in

some conditions, over long charge times, dendritic lead growths form which can eventually cause the cell to short.

Further characterisation of battery performance has revealed that favourable energy efficiencies are produced when operating the cell between 273 K and 313 K. Also, lower overpotentials (hence, higher efficiency) are observed when the battery is operated at low rates of charge / discharge. Despite this, there is only slight deterioration with higher current densities and even up to 60 mA cm^{-2}, good performance data is recoded.

State of charge investigations have demonstrated that it is possible to deplete the $Pb(CH_3SO_3)_2$ concentration in the electrolyte to at least 0.1 mol dm^{-3} without significant loss of battery performance.

Self discharge of the battery only occurs on a large time scale and appears to be limited to the dissolution of Pb by reaction with O_2. Indeed, leaving the battery on open circuit and increasing the supply of aqueous O_2 is a possible method for removing excess Pb deposits, built up due to the inequality in the efficiency of the Pb and PbO_2 electrode reactions. However, if this is not permissible, self discharge may easily be avoided by trickle charging the battery.

Chapter 6: Electrolyte Additives

6.1 Introduction

6.1.1 What are Additives: Additives can be defined as chemicals which, when added to the electrolyte solution, preferentially alter the battery performance in some manner. The additives used in this project may be divided into two classes:

♦ Firstly: additives that effect the deposition and stripping of Pb and/or PbO_2, improving the quality of deposits by preventing dendrite growth and facilitating in the formation of compact layers, generally known as grain refining or brightening additives.[101-104]

♦ Secondly: additives which give enhanced cell voltage responses, for example by improving the conductivity of PbO_2 through co-deposition of other metal ions.[82, 105-108]

6.1.2 The need for Additives: It was shown in chapter 3 that there is a significant overvoltage associated with the Pb^{2+}/PbO_2 electrode couple. Furthermore the charge balance between deposition and stripping of PbO_2 layers has been found to be lower than for Pb deposition and stripping. Any additive that decreases the overvoltage and improves charge balancing would be advantageous for the battery system. It should also be noted that the resistance of PbO_2 (10^{-4} Ω cm) is higher than that of Pb (10^{-5} Ω cm). Clearly, any additive that increases the conductivity of PbO_2 would improve the battery performance. A number of inorganic ions, for example Sb^{3+}, Bi^{3+}, Fe^{3+}, Ni^{2+} and Ag^{+}, are known to influence the conductivity and electrocatalytic properties of PbO_2.[46, 109-111] Also, Cu^{2+} is a common additive in electrolytes for the electrodeposition of PbO_2 layers, although its role is not clear.[102, 106] It was therefore decided to investigate the influence on battery performance of three metal ions (Ni^{2+}, Fe^{3+} and Sb^{3+}) when added to the electrolyte solution.

It has been found that the Pb deposits have a tendency to become dendritic and boulderous in nature at high current densities or during long deposition times. Figure 6.1 shows an SEM image of a Pb deposit onto a type III electrode within the flow cell. In fact, this electrode was from a 4 hour deposition experiment which was halted after 3 hours due to the Pb dendrites growing across the interelectrode gap and shorting the cell. The electrolyte consisted of $Pb(CH_3SO_3)_2$ (1.5 mol dm^{-3}) in aqueous CH_3SO_3H (0.9 mol dm^{-3}). The interelectrode gap was 0.4 cm and the linear flow rate across the electrode surface was 9.5 cm s^{-1}. The current density was 20 mA cm^{-2}. Clearly the additive must give the required improvements without degrading the battery performance. For example, an additive used for improving the uniformity of the Pb deposit must not be oxidised at the PbO_2 electrode. There are a large number of additives available for smoothing of lead deposits, however two were chosen (sodium ligninsulfonate and polyethylene glycol-200) for testing within the battery electrolyte.

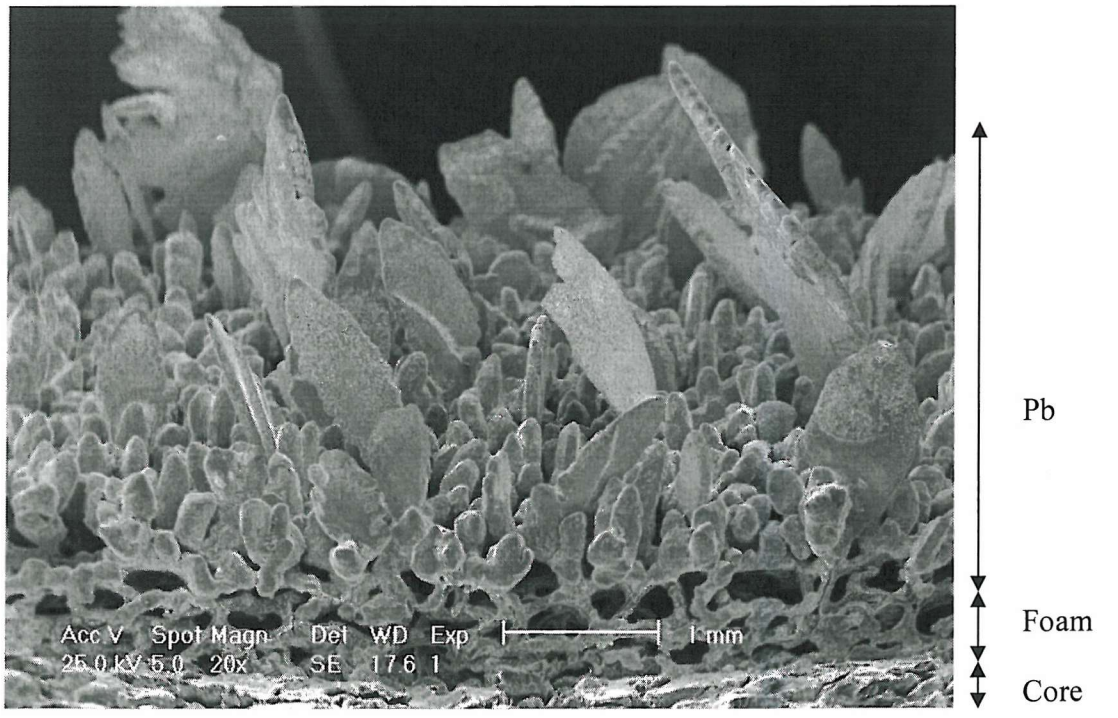

Figure 6.1: *Circa 3 hour Pb deposition, onto a type III electrode, from an electrolyte consisted of $Pb(CH_3SO_3)_2$ (1.5 mol dm^{-3}) in aqueous CH_3SO_3H (0.9 mol dm^{-3}). The interelectrode gap was 0.4 cm and the linear flow rate across the electrode surface was 9.5 cm s^{-1}. The current density was 20 mA cm^{-2}.*

6.2 Sodium Ligninsulfonate

6.2.1 Choosing a Suitable Additive: Brightening and grain refining additives have been extensively investigated, for use in commercial plating baths for the electrodeposition of lead, tin and tin-lead alloys.[103, 104, 112, 113] Consequently, numerous known additives are available for investigation within the battery. Sodium ligninsulfonate has been chosen as it is an additive that shows good grain refining properties, is stable in methanesulfonic acid and is unlikely to be oxidised at the PbO_2 anode.

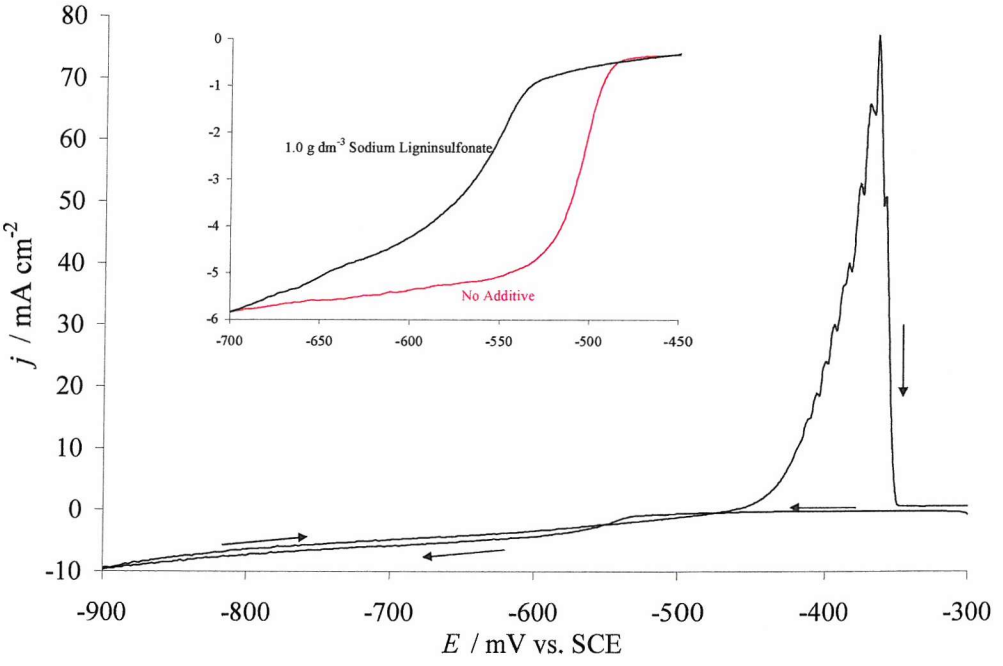

Figure 6.2: *a cyclic voltammogram of the Pb^{2+}/Pb couple performed at a nickel RDE (ω = 1600 RPM) between potential limits of -300 mV vs. SCE and -900 mV vs. SCE at a scan rate of 50 mV s^{-1}. The electrolyte solution contained $Pb(CH_3SO_3)_2$ (4 mmol dm^{-3}) and sodium ligninsulfonate (1 g dm^{-3}) in aqueous CH_3SO_3H (2.0 mol dm^{-3}). The temperature was maintained at 298 K. Inset: enlarged view comparing reduction wave with and without the use of sodium ligninsulfonate.*

Figure 6.2 presents a cyclic voltammogram of the Pb^{2+}/Pb couple performed at a nickel RDE (ω = 1600 RPM) between potential limits of -300 mV vs. SCE and -900 mV vs. SCE at a scan rate of 50 mV s^{-1}. The electrolyte solution contained $Pb(CH_3SO_3)_2$ (4

mmol dm^{-3}) and sodium ligninsulfonate (1 g dm^{-3}) in aqueous CH_3SO_3H (2.0 mol dm^{-3}). The temperature was maintained at 298 K. The response is typical of the results obtained using sodium ligninsulfonate as an additive. On the negative scan a drawn out cathodic reduction wave is observed, commencing at circa -530 mV vs. SCE, leading to a limiting current density. On the reverse scan the deposition of Pb continues to -470 mV vs. SCE, following which the current becomes anodic and a stripping peak is observed. Compared with voltammograms performed without additive, the kinetics of the Pb^{2+}/Pb couple appear slower and the nucleation overpotential is increased from 35 mV vs. SCE to a 60 mV vs. SCE, and the reduction wave is much less steep. Even so, the overpotential associated with the charging and discharging of the Pb electrode is still small. Also, the limiting current is not affected, the charge balance is close to 1 and the overvoltage does not significantly increase with higher additive concentrations. It should also be stressed that the $[Pb^{2+}]$:[sodium ligninsulfonate] ratio in such cyclic voltammograms is quite different from that used in later battery electrolytes.

Sodium Ligninsulfonate Concentration / g dm^{-3}	j_{anodic} / mA cm^{-2}	$j_{cathodic}$ / mA cm^{-2}	$\eta_{nucl.}$ / mV	$\frac{Q_{cathodic}}{Q_{anodic}}$ / %
0.0	85.0	90.7	296	85
0.1	89.5	87.0	316	78
1.0	77.5	67.6	326	71
5.0	62.0	55.4	395	58
10	58.5	59.3	433	52

Table 6.1: *Data from cyclic voltammograms recorded at a vitreous carbon RDE rotating at 900 rpm. The electrolyte comprised $Pb(CH_3SO_3)_2$ (1.5 mol dm^{-3}) in aqueous CH_3SO_3H (0.9 mol dm^{-3}) with various concentrations of sodium ligninsulfonate additive. Voltammograms recorded between potential limits of 0.0 V vs. SCE and 1.90 V vs. SCE, at a scan rate of 50 mV s^{-1}. Temperature 298 K. Current densities at 1.90 V vs. SCE for PbO_2 deposition, peak current densities for PbO_2 dissolution, nucleation overpotential and charge efficiency.*

The Pb^{2+}/PbO_2 couple was also studied. A series of cyclic voltammograms were recorded at a vitreous carbon RDE (ω = 400, 900, 1600 and 2500 rpm) from a solution containing $Pb(CH_3SO_3)_2$ (1.5 mol dm^{-3}) in aqueous CH_3SO_3H (0.9 mol dm^{-3}) and various

amounts of sodium ligninsulfonate (0.1, 1, 5 and 10 g dm^{-3}). The potential was cycled between 0 V vs. SCE and 1.90 V vs. SCE using a scan rate of 50 mV s^{-1}. The voltammograms obtained were all of similar form to those obtained without additive, however in the presence of the additive higher overvoltages and lower current densities were observed. Table 6.1 presents data from cyclic voltammograms recorded at 900 rpm, showing the current densities at 1.90 V vs. SCE for PbO_2 deposition (j_{anodic} / mA cm^{-2}), peak current densities for PbO_2 dissolution ($j_{cathodic}$ / mA cm^{-2}), nucleation overpotential ($\eta_{nucl.}$ / mV) and charge efficiency ($\frac{Q_{cathodic}}{Q_{anodic}}$ / %) for the different concentrations of sodium ligninsulfonate. It can be seen that with increasing additive concentration the current densities and charge efficiency decrease and the nucleation overpotential increases. However at additive concentrations below 1.0 g dm^{-3} these effects are relatively small and should not significantly detriment the battery performance.

Figure 6.3(A,C) shows SEM images of Pb layers, deposited from an electrolyte containing $Pb(CH_3SO_3)_2$ (0.3 mol dm^{-3}) in aqueous CH_3SO_3H (2.0 mol dm^{-3}). Figure 6.3(B,D) shows SEM images of analogous layers, deposited from a similar electrolyte additionally containing 1.0 g dm^{-3} sodium ligninsulfonate. A current density of 50 mA cm^{-2} (6.3 A and B) and 375 mA cm^{-2} (6.3 C and D) applied for 600 s was used to deposit the layers at a vitreous carbon RDE (ω = 900 RPM) with an electrolyte temperature of 298 K. At the lower current density, without additive, the Pb deposit is boulderous, particularly at the edge, with clearly definable Pb grains (circa 20 μm diameter) while by comparison, with additive present, the deposit is smooth and continuous with no individual Pb grains visible on this scale. The effect of the additive is again evident at the higher current density. Without additive the deposit is dendritic and made up of large plates, however with additive present the deposit is more compact and made up of nodular growths without any features extending above the main Pb layer.

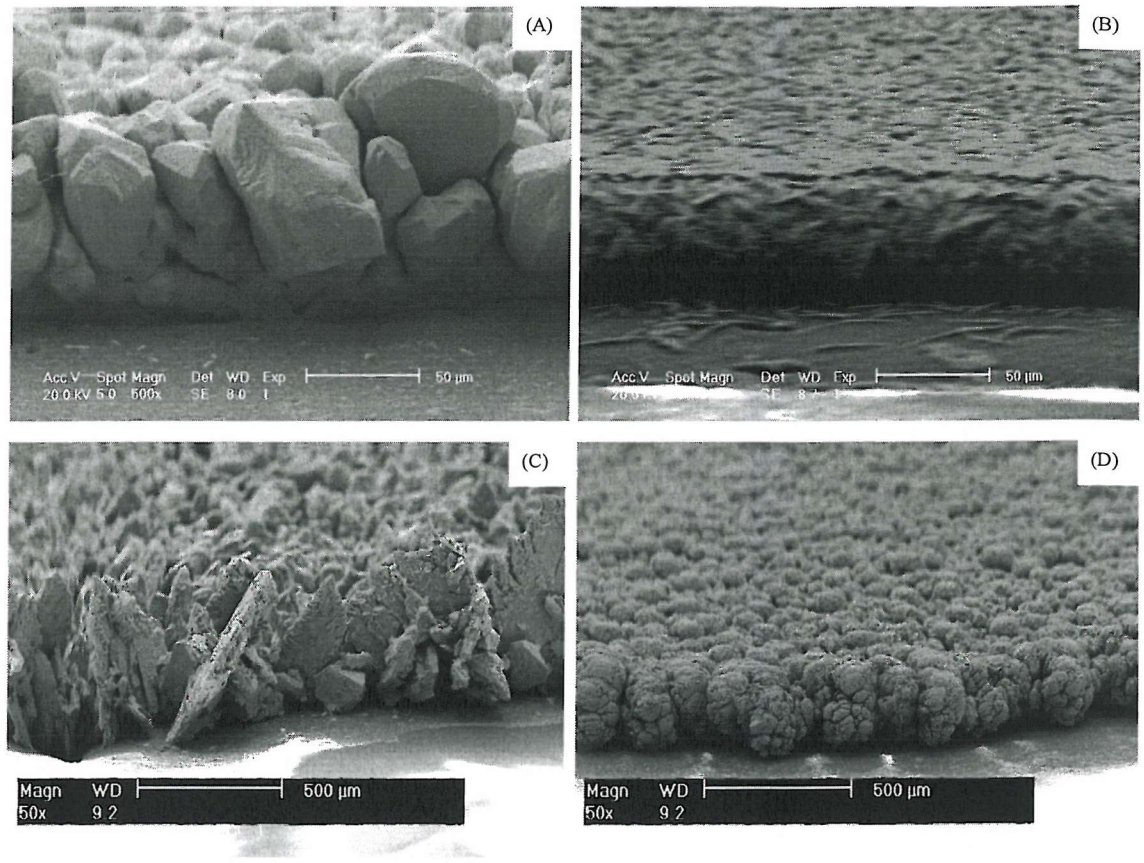

Figure 6.3: *SEM images of Pb deposits on a vitreous carbon RDE (ω = 900 RPM). A current density of 50 mA cm^{-2} (A+B) and 375 mA cm^{-2} (C+D) for 600 s was used to deposit both layers, with an electrolyte temperature of 298 K. The electrolyte consisted of: (A+C) $Pb(CH_3SO_3)_2$ (0.3 mol dm^{-3}) in aqueous CH_3SO_3H (2.0 mol dm^{-3})and (B+D) with the addition of 1.0 g dm^{-3} sodium ligninsulfonate.*

6.2.2 Deposition onto Flow Cell Electrodes: A series of experiments was performed with the flow cell fitted with type I (core plate) electrodes, where the cell was charged at 20 mA cm^{-2} for 1 hour. In each case the electrolyte comprised $Pb(CH_3SO_3)_2$ (1.5 mol dm^{-3}) in aqueous CH_3SO_3H (0.9 mol dm^{-3}) and was held in a water bath thermostated at 298 K. The interelectrode gap was 1.6 cm and the linear flow rate across the electrodes surfaces was 2.5 cm s^{-1}. Electrical contact to the electrodes was made via a single metal screw pressed against the reverse of the electrode. Figure 6.4 shows SEM images of Pb deposits, from experiments in which the electrolyte additionally contained: (A) no additive, (B) 0.2 g dm^{-3} sodium ligninsulfonate, (C) 1 g dm^{-3} sodium ligninsulfonate and (D) 5 g dm^{-3} sodium ligninsulfonate.

Without additive the deposited Pb layer is composed of large Pb grains, circa 80 μm diameter. The grains appear to have grown from individual nucleation points on the electrode surface and do not fully overlap. Indeed significant gaps remain between the grains and areas of the electrode surface are clearly visible through the deposit. With increasing sodium ligninsulfonate concentration the deposit becomes more compact, the Pb growth centres overlap to a greater extent and at the highest additive concentration the Pb deposit is a continueous unbroken layer.

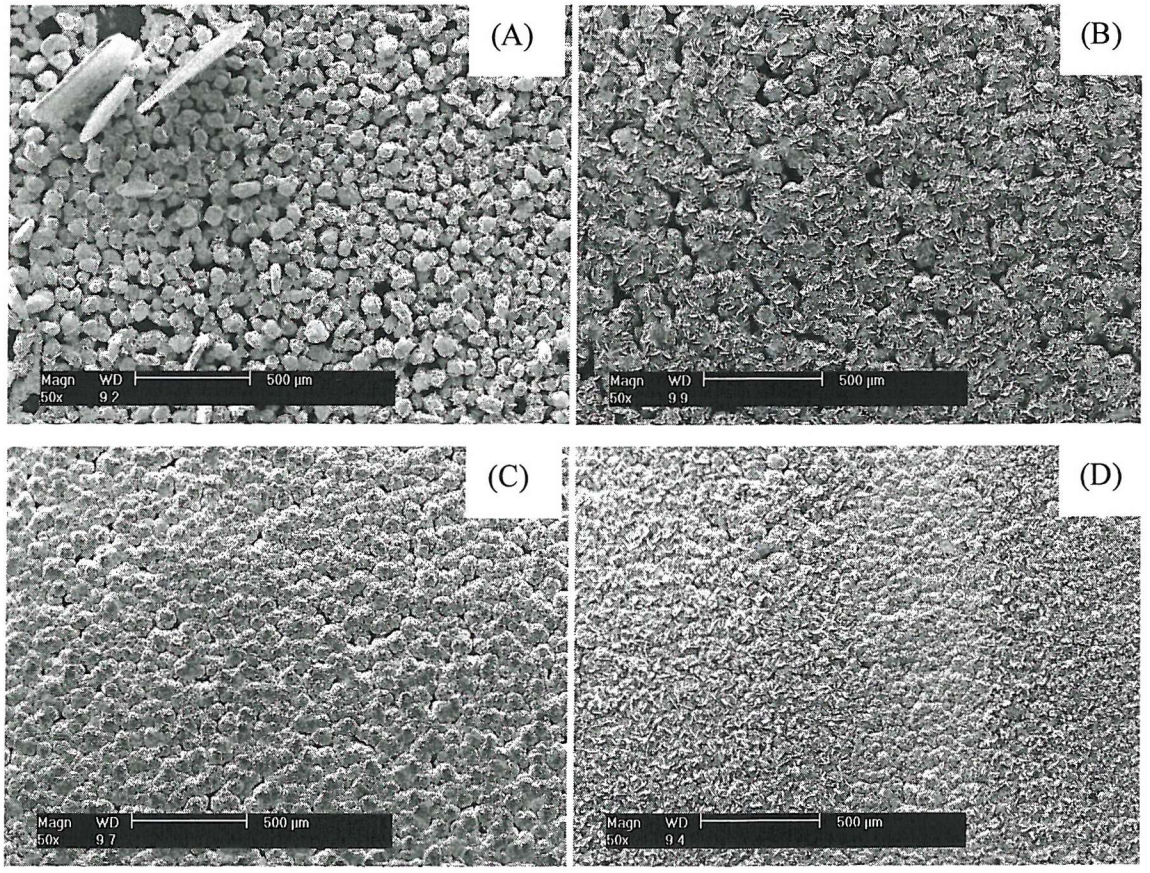

Figure 6.4: *SEM images of Pb layers on type I electrodes, deposited for 1 hour at 20 mA* cm^{-2}*. The reservoir was charged with 40* cm^3 *electrolyte and thermostated at 298 K. The interelectrode gap was set at 1.6 cm and the linear flow rate across the electrode surface was 2.5 cm* s^{-1}*. The electrolyte initially consisted of: (A)* $Pb(CH_3SO_3)_2$ *(1.5 mol* dm^{-3}*) in aqueous* CH_3SO_3H *(0.9 mol* dm^{-3}*), (B) with 0.2 g* dm^{-3} *sodium ligninsulfonate, (C) 1.0 g* dm^{-3} *sodium ligninsulfonate and (D) 5 g* dm^{-3} *sodium ligninsulfonate.*

The smoothing effect of sodium ligninsulfonate is further demonstrated by figure 6.5 which shows the end view of the Pb electrodes from the experiments with no additive

and with the addition of 1 g dm^{-3} sodium ligninsulfonate. The SEM images were taken at an angle of 70°. It can clearly be seen that at the edge of the electrode, without the additive, the deposit is rocky with significant edge effect, while with additive the edge effect is much reduced and the deposit is smoother, having no peaked growths.

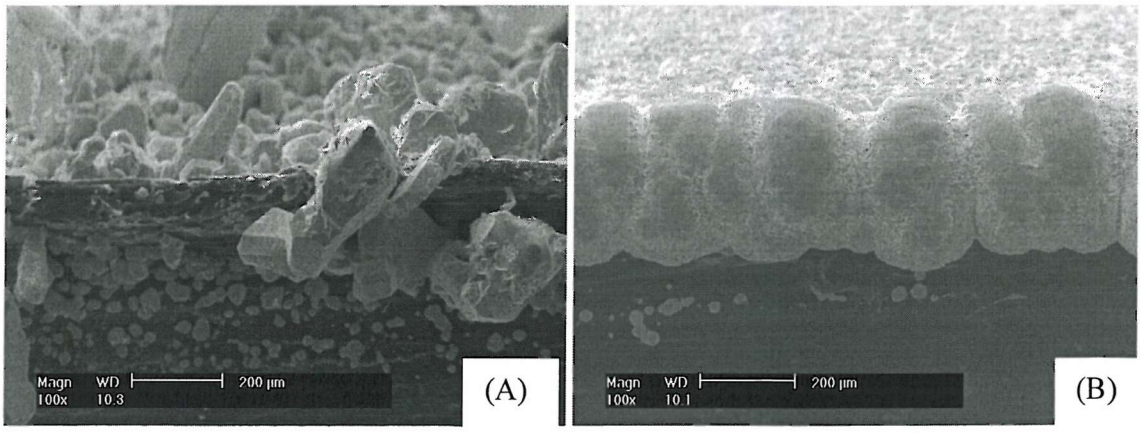

Figure 6.5: *SEM images of Pb layers on type I electrodes, deposited for 1 hour at 20 mA cm^{-2}. The reservoir was charged with 40 cm^3 electrolyte and thermostated at 298 K. The interelectrode gap was set at 1.6 cm and the linear flow rate across the electrode surface was 2.5 cm s^{-1}. The electrolyte initially consisted of: (A) $Pb(CH_3SO_3)_2$ (1.5 mol dm^{-3}) in aqueous CH_3SO_3H (0.9 mol dm^{-3}) and (B) with 1.0 g dm^{-3} sodium ligninsulfonate.*

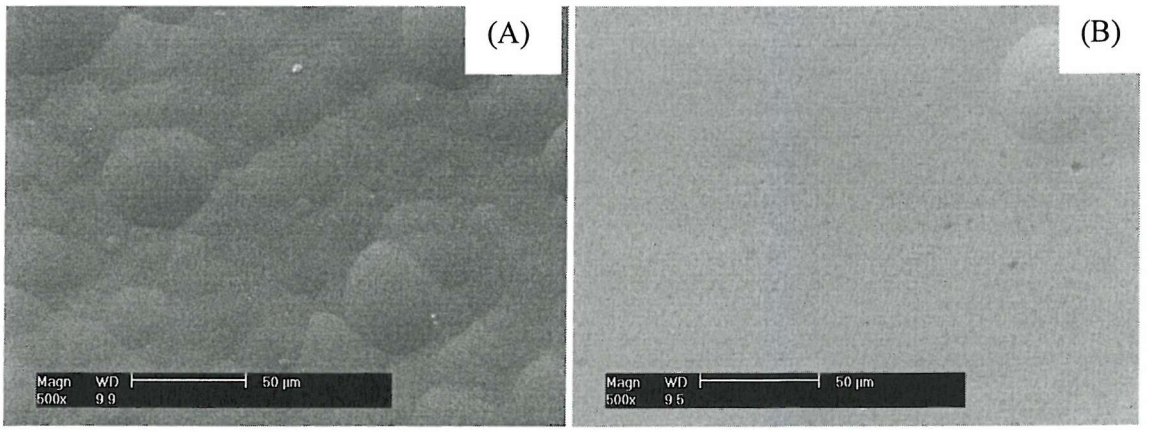

Figure 6.6: *SEM images of PbO_2 layers on type I electrodes, deposited for 1 hour at 20 mA cm^{-2}. The reservoir was charged with 40 cm^3 electrolyte and thermostated at 298 K. The interelectrode gap was set at 1.6 cm and the linear flow rate across the electrode surface was 2.5 cm s^{-1}. The electrolyte initially consisted of: (A) $Pb(CH_3SO_3)_2$ (1.5 mol dm^{-3}) in aqueous CH_3SO_3H (0.9 mol dm^{-3}) and (B) with 1.0 g dm^{-3} sodium ligninsulfonate.*

Figure 6.6 shows SEM images of the PbO_2 deposits taken without additive and with 1 g dm^{-3}. Both deposits are clearly built up from overlapping hemispherical growth centres, however when additive is present the PbO_2 hemispheres are less distinct and the deposit slightly smoother. However it should be noted that even without additive, the PbO_2 deposits are significantly smoother and more compact in comparison with Pb deposits.

With higher additive concentrations, craters in the PbO_2 layer suggest that during charge some of the current is used in oxygen evolution. Figure 6.7 shows an SEM image of the PbO_2 deposit with 5 g dm^{-3} sodium ligninsulfonate added to the electrolyte. Clearly visible are crater marks were bubbles have formed on the surface of the PbO_2 layer and further deposition has occurred around these bubbles.

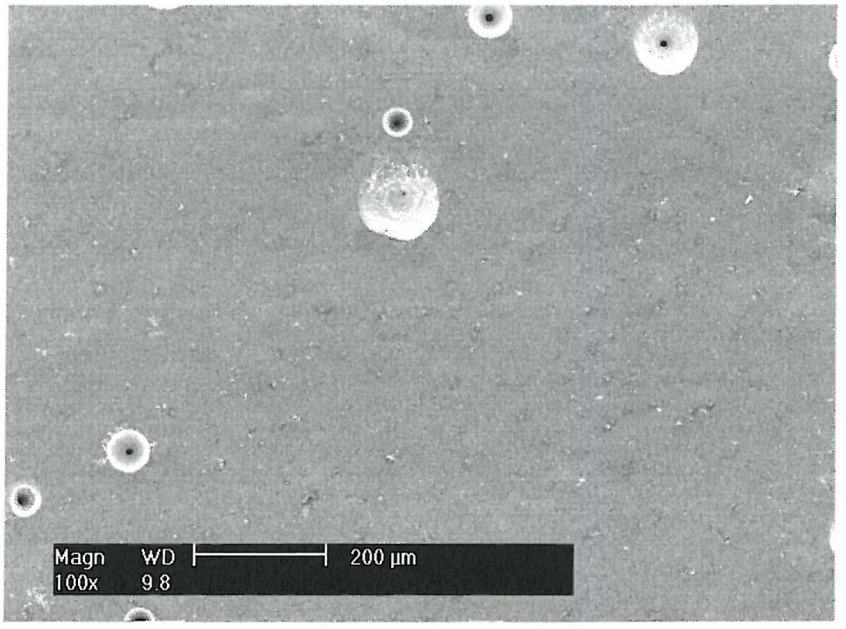

Figure 6.7: *SEM image of PbO_2 layer on a type I electrode, deposited for 1 hour at 20 mA cm^{-2}. The reservoir was charged with 40 cm^3 electrolyte and thermostated at 298 K. The interelectrode gap was set at 1.6 cm and the linear flow rate across the electrode surface was 2.5 cm s^{-1}. The electrolyte initially consisted of $Pb(CH_3SO_3)_2$ (1.5 mol dm^{-3}) in aqueous CH_3SO_3H (0.9 mol dm^{-3}) with the addition of 5.0 g dm^{-3} sodium ligninsulfonate.*

A series of 1 hour depositions were carried out, in the first instance, using only type IV (scraped RVC) and in the second instance, using a combination of type IV (positive) and type II (negative) electrodes within the flow cell. Electrical connection was made via a

screw contact to the reverse of the electrode. The interelectrode distance was set at 1.60 cm and the linear flow rate across the electrode surface was 2.5 cm s^{-1}, with the solution pumped from a thermostated reservoir (298 K) containing 40 cm^3 of electrolyte. The electrolyte initially comprised $Pb(CH_3SO_3)_2$ (1.5 mol dm^{-3}) in aqueous CH_3SO_3H (0.9 mol dm^{-3}) with several different concentrations of sodium ligninsulfonate additive (0.0 g dm^{-3}, 0.2 g dm^{-3}, 1.0 g dm^{-3} and 5.0 g dm^{-3}). The current density for each experiment was 20 mA cm^{-2}.

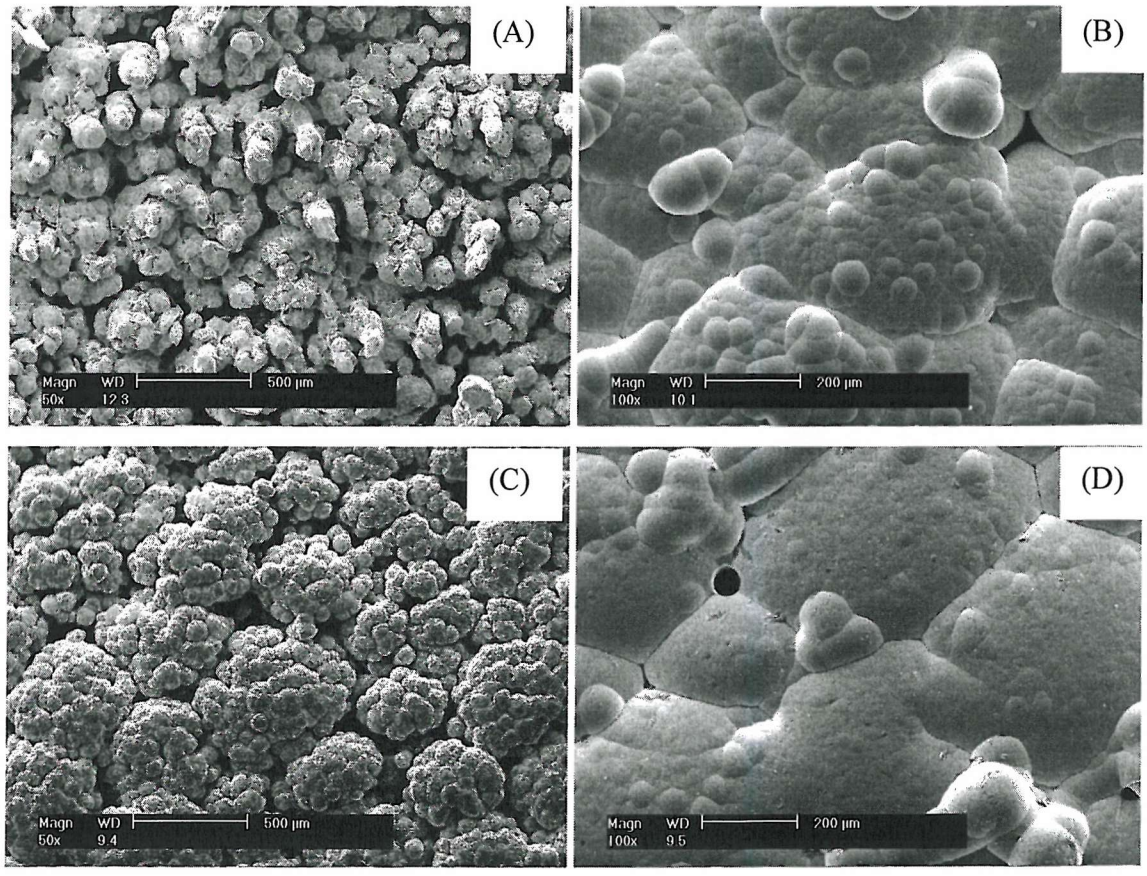

Figure 6.8: *SEM images of Pb and PbO_2 layers on type IV electrodes, deposited for 1 hour at 20 mA cm^{-2}. The reservoir was charged with 40 cm^3 electrolyte and thermostated at 298 K. The interelectrode gap was set at 1.6 cm and the linear flow rate across the electrode surface was 2.5 cm s^{-1}. The electrolyte initially consisted of (A + B) $Pb(CH_3SO_3)_2$ (1.5 mol dm^{-3}) in aqueous CH_3SO_3H (0.9 mol dm^{-3}) and with the addition of 1 g dm-3 sodium ligninsulfonate (C + D). (A) Pb electrode – no additive, (B) PbO^2 electrode – no additive, (C) Pb electrode - with additive, (D) PbO_2 electrode – with additive.*

These experiments confirm the results obtained on the flat, type I, electrodes; with increasing sodium ligninsulfonate the Pb and PbO_2 deposited layers are smoother and more compact. Figure 6.8 shows SEM images of the Pb and PbO_2 electrodes with no additive present and with 5 g dm^{-3} sodium ligninsulfonate. Both with and without the additive the PbO_2 layers are dominated by the form of the electrode surface, with the deposits clearly following the contours of the underlying surface. This is less evident with the Pb deposit without additive, however with increasing additive concentration the deposits become more defined and with 5 g dm^{-3} the Pb layer follows clearly the surface of the electrode.

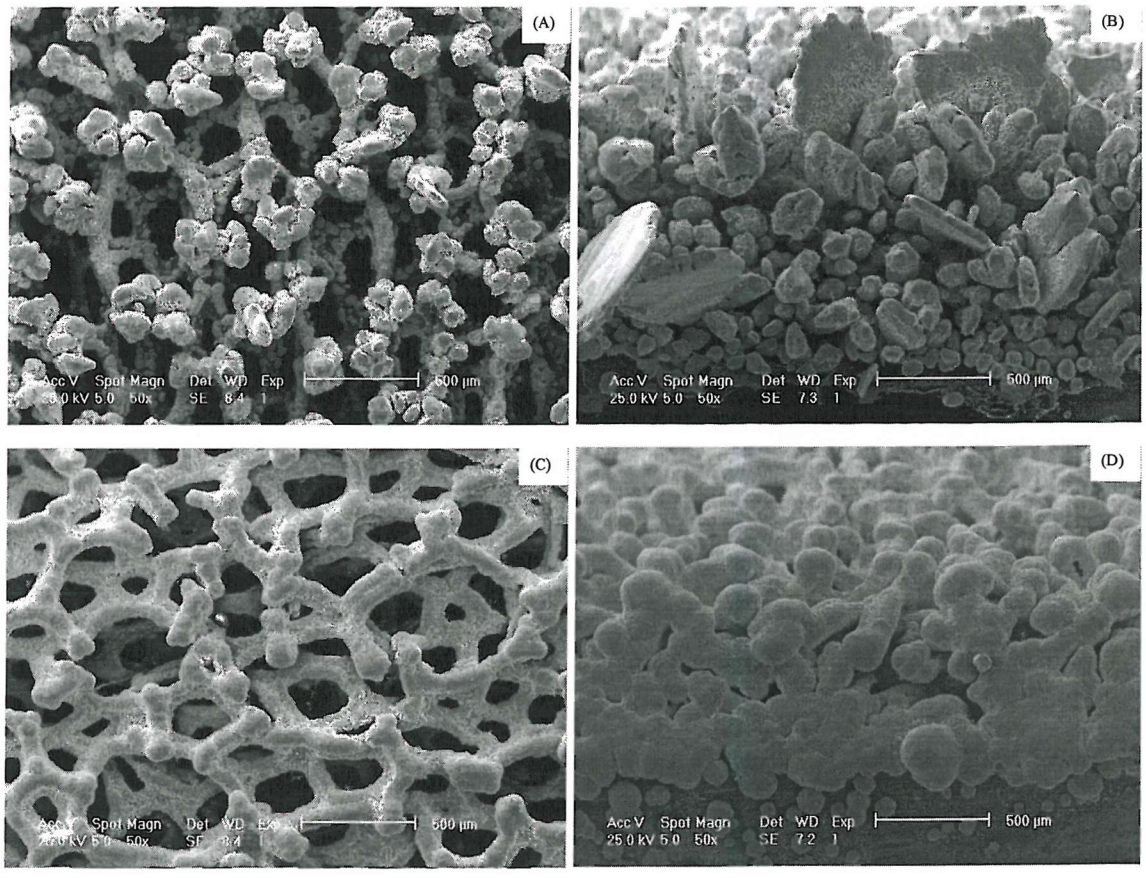

Figure 6.9: *SEM images of Pb on type II electrodes, deposited at 20 mA cm^{-2} for 3600 s. Top view: images A and C, edge view, at 70°: images B and D. Images A and B: No additive, Images C and D: 1 g dm^{-3} sodium ligninsulfonate.*

Figure 6.9 shows the Pb deposit on the type II electrodes with (A + B) no additive and (C + D) 1 g dm^{-3} sodium ligninsulfonate. Images A and C are of the top face of the electrode, while images B and D are of the end of the electrode, exposed to the electrolyte flow, taken at 70°. It is clear to see that without additive present there are considerable Pb deposits outside the Ni foam structure. However with additive present the deposits are smoother, centred around the Ni fragments and completely held within the foams' structure.

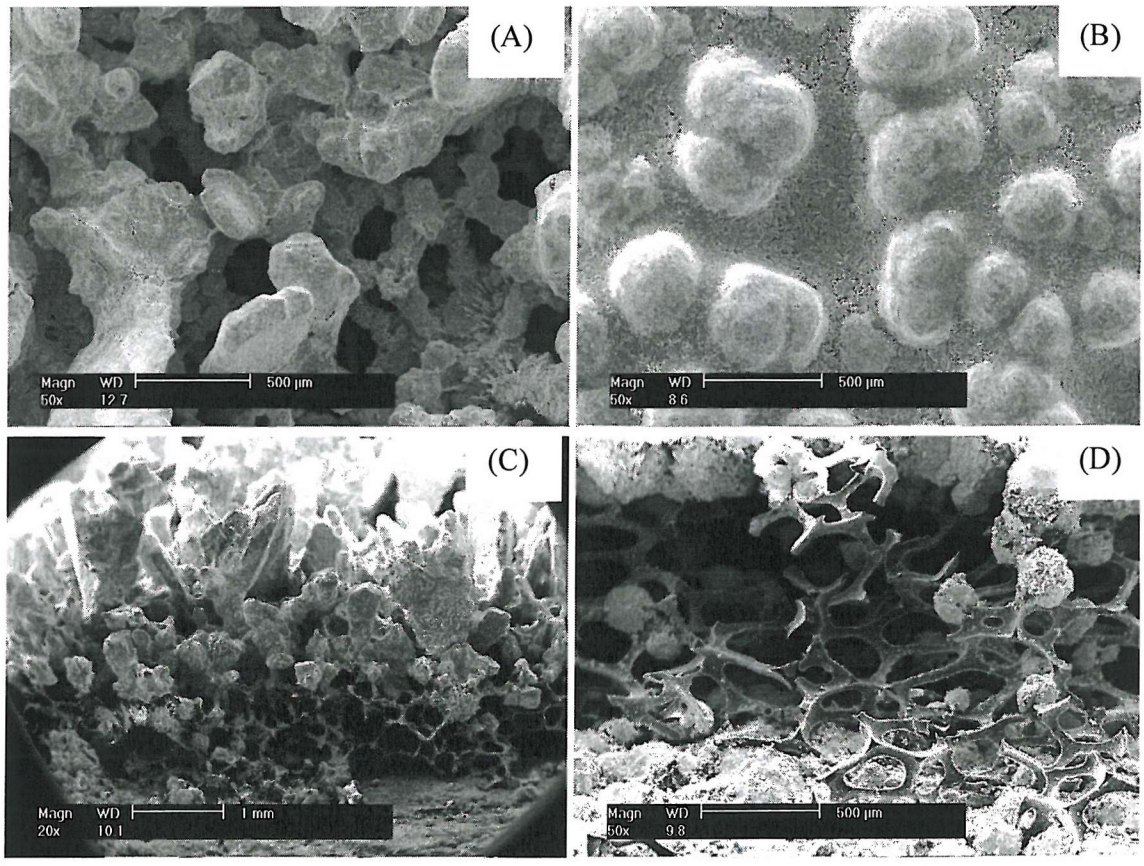

Figure 6.10: *SEM images of Pb layers on type III electrodes, deposited for 6 hours at a current density of 20 mA cm^{-2}. The reservoir was charged with 40 cm^3 electrolyte and thermostated at 298 K. The interelectrode gap was set at 1.6 cm and the linear flow rate across the electrode surface was 2.5 cm s^{-1}. The electrolyte initially consisted of: (A) Top view of deposit from electrolyte containing $Pb(CH_3SO_3)_2$ (1.5 mol dm^{-3}) in aqueous CH_3SO_3H (0.9 mol dm^{-3}), (B)Top view of deposit with 1.0 g dm^{-3} sodium lignin sulfonate, (C) side view without additive and (D) side view of deposit with additive.*

Two six hour deposition experiments were performed on type III (RVC foam) electrodes within the flow cell, one without additive, the other with 1 g dm^{-3} sodium ligninsulfonate added to the electrolyte. The interelectrode distance was set at 1.60 cm and

the linear flow rate across the electrode surface was 2.5 cm s^{-1}, pumped from a thermostated reservoir (298 K) containing 40 cm^3 electrolyte. The electrolyte initially comprised $Pb(CH_3SO_3)_2$ (1.5 mol dm^{-3}) in aqueous CH_3SO_3H (0.9 mol dm^{-3}). A current density of 20 mA cm^{-2} was used for both depositions and electrical connection was made via a screw contact to the reverse of the electrode.

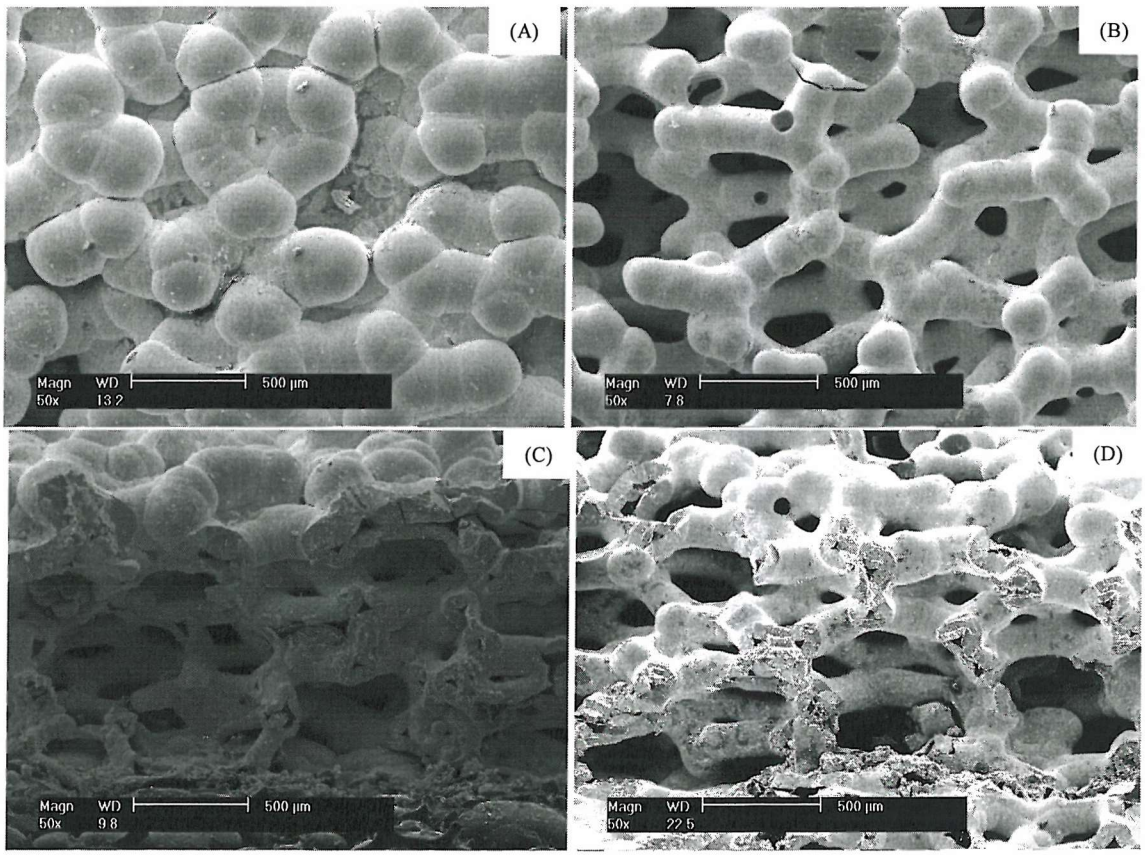

Figure 6.11: *SEM images of PbO_2 layers on type III electrodes, deposited for 6 hours at a current density of 20 mA cm^{-2}. The reservoir was charged with 40 cm^3 electrolyte and thermostated at 298 K. The interelectrode gap was set at 1.6 cm and the linear flow rate across the electrode surface was 2.5 cm s^{-1}. The electrolyte initially consisted of: (A) Top view of deposit from electrolyte containing $Pb(CH_3SO_3)_2$ (1.5 mol dm^{-3}) in aqueous CH_3SO_3H (0.9 mol dm^{-3}), (B)Top view of deposit with 1.0 g dm^{-3} sodium lignin sulfonate, (C) side view without additive and (D) side view of deposit with additive.*

Figure 6.10 presents SEM images of the Pb electrodes with and without the addition of sodium ligninsulfonate. Without additive the Pb deposit consists of an uneven, nodular layer which is predominantly situated on the outer, top surface of the reticulated structure.

In fact very little Pb appears to be deposited within the foams' pores. With sodium ligninsulfonate present a smoother more compact deposit is observed and the foam structure is extensively covered by an overlapping Pb layer. However inspection of the edge of the electrode (figure 6.10 D) reveals that, despite a continuous Pb layer, the deposit is again situated towards the outer surface of the foam, with little Pb present within the electrodes pores.

Figure 6.11 shows SEM images, from above and from the side, of the PbO_2 electrodes. With sodium ligninsulfonate additive, the PbO_2 layer is deposited uniformly throughout the foam structure and clear interconnection of solution between the foams' pores is still evident. Without additive the deposit is less uniform and thicker towards the outer edges of the foam than within the structure, closer to the core plate.

6.2.3 Cell Cycling with Sodium Ligninsulfonate: A series of charge / discharge cycles was performed with the flow cell fitted with type II (Pb) and type IV (PbO_2) electrodes (nickel foam and scraped RVC respectively). Each cycle consisted of a 900 s charge (j = 20 mA cm^{-2}) followed by discharge, at the same current density, until the voltage dropped to 1.20 V. The experiment totalled 84 complete cycles followed by a final 900 s charge. The cell was supplied with an electrolyte initially containing $Pb(CH_3SO_3)_2$ (1.5 mol dm^{-3}) and sodium ligninsulfonate (1.0 g dm^{-3}) in aqueous CH_3SO_3H (0.9 mol dm^{-3}). Figure 6.12 shows the voltage vs. time plots for the $1^{st} - 6^{th}$, $43^{rd} - 48^{th}$ and $79^{th} - 84^{th}$ cycles of the cell. The profile of the plots is consistent with cycles performed without additive; constant voltages for charge and discharge during the first cycle, with a voltage trough appearing in the second and subsequent charges, which gradually enlarges to cover the majority of the charge period. The coulombic efficiency remained relatively constant at circa 80 %, throughout the 84 cycles. The energy efficiency, however, progressively rose from circa 60 % to circa 70 % between the initial and final cycles, as the overpotentials during both charge and discharge can be seen to decrease.

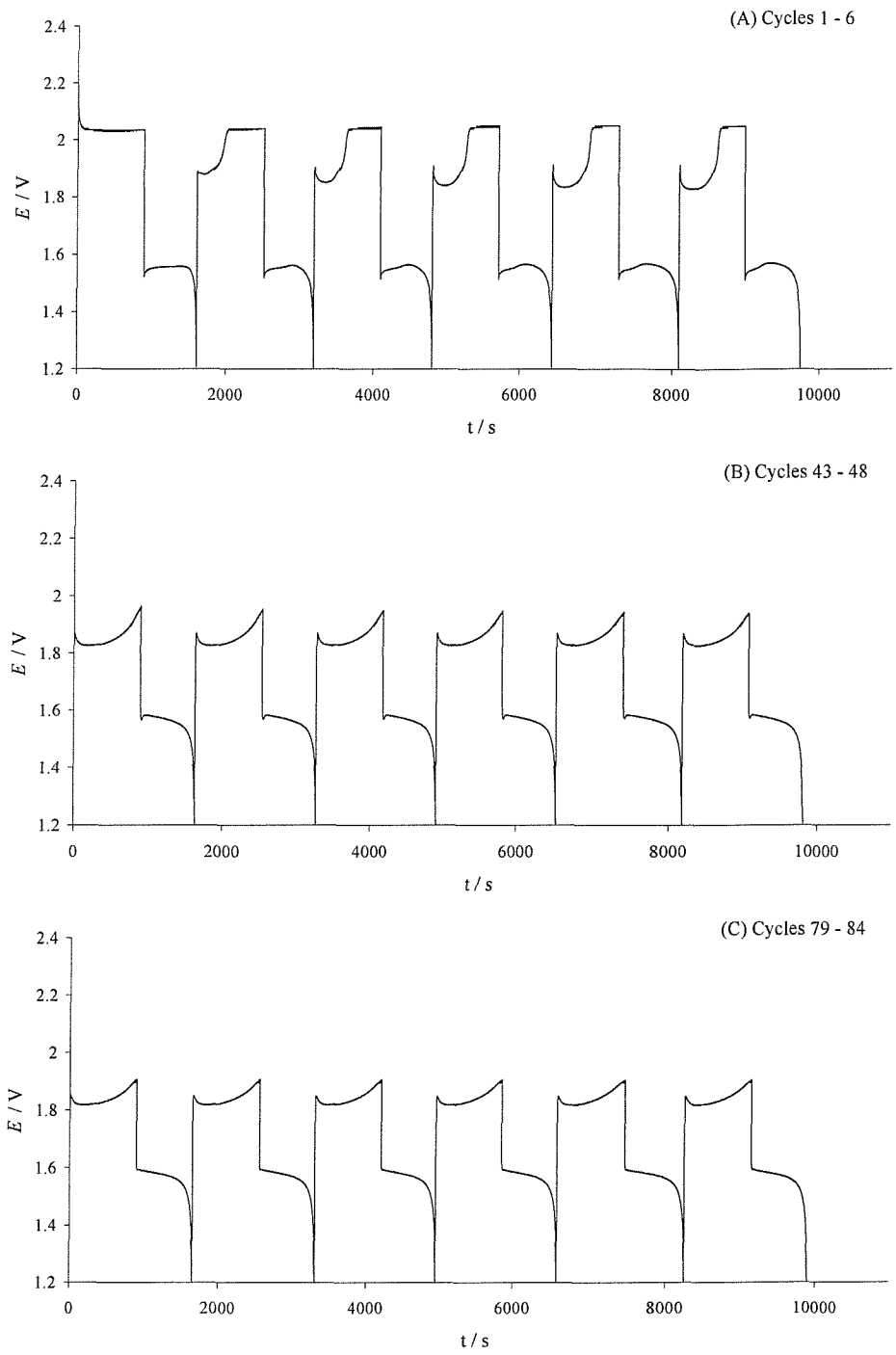

Figure 6.12: *Cell voltage vs. time data for various points in a series of 84 charge / discharge cycles of the flow cell. Each cycle consisted of a 900 s charge at 20 mA cm^{-2} followed by discharge, at the same current density, until the voltage dropped to 1.20 V. The electrolyte initially consisted of $Pb(CH_3SO_3)_2$ (1.5 mol dm^{-3}) and sodium ligninsulfonate (1.0 g dm^{-3}) in aqueous CH_3SO_3H (0.9 mol dm^{-3}). (A) cycles 1 – 6, (B) cycles 43 – 48, (C) cycles 79 – 84.*

Table 6.2 presents voltage data from the final cycle of this experiment and a similar experiment performed without the addition of sodium ligninsulfonate. Values given are for; average voltage over the full charge ($\bar{U}_c$ / V), average voltage over full discharge ($\bar{U}_d$ / V), the difference between charge and discharge voltages ($\bar{U}_c - \bar{U}_d$ / V), the average voltage during the first 50 s of discharge ($\bar{U}_{50}$ / V) and the average voltage during the first 150 s of discharge ($\bar{U}_{150}$ / V). It can be seen that over the whole charge / discharge cycle the voltages obtained are very similar. However the shape of the discharge curve is more sloped than without the additive and during the initial stages of discharge the voltages are circa 20 mV higher than without sodium ligninsulfonate present.

Sodium ligninsulfonate	$\bar{U}_c$ / V	$\bar{U}_d$ / V	$\bar{U}_c - \bar{U}_d$ / V	$\bar{U}_{50}$ / V	$\bar{U}_{150}$ / V
None	1.84	1.56	0.28	1.65	1.60
1.0 g dm^{-3}	1.85	1.56	0.29	1.67	1.62

Table 6.2: *Average voltage over the full charge ($\bar{U}_c$ / V), average voltage over full discharge ($\bar{U}_d$ / V), the difference between charge and discharge voltages ($\bar{U}_c - \bar{U}_d$ / V), the average voltage during the first 50 s of discharge ($\bar{U}_{50}$ / V) and the average voltage during the first 150 s of discharge ($\bar{U}_{150}$ / V)*

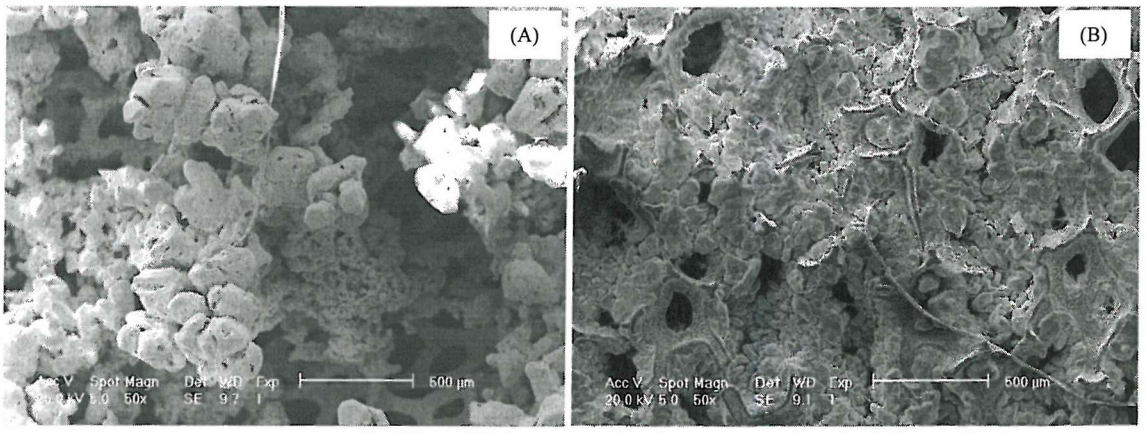

Figure 6.13: *SEM images of Pb electrodes (Type II), following repeated cycling, with: (A) No additive and (B) 1 g dm^{-3} sodium ligninsulfonate.*

Figure 6.13 shows SEM images comparing the Pb (type II) electrodes after the repeated cycling with 1.0 g dm^{-3} sodium ligninsulfonate and without additive. It can be seen that with sodium ligninsulfonate the deposit following the final charge is compact and held with in the nickel foam's structure. Without additive, however, there are considerable nodular Pb growths protruding above the surface of the nickel foam. In fact the deposit is quite irregular.

Figure 6.14 shows SEM images comparing the PbO_2 electrodes after the repeated cycling with 1.0 g dm^{-3} and without additive. Both with and without the use of sodium ligninsulfonate the PbO_2 deposits are quite different in appearance to single depositions performed on clean electrodes. Following repeated cycling the PbO_2 deposits are composed of a sheet of small, angular granules with diameter circa 2 μm with the use of sodium ligninsulfonate and circa 5 μm without the additive.

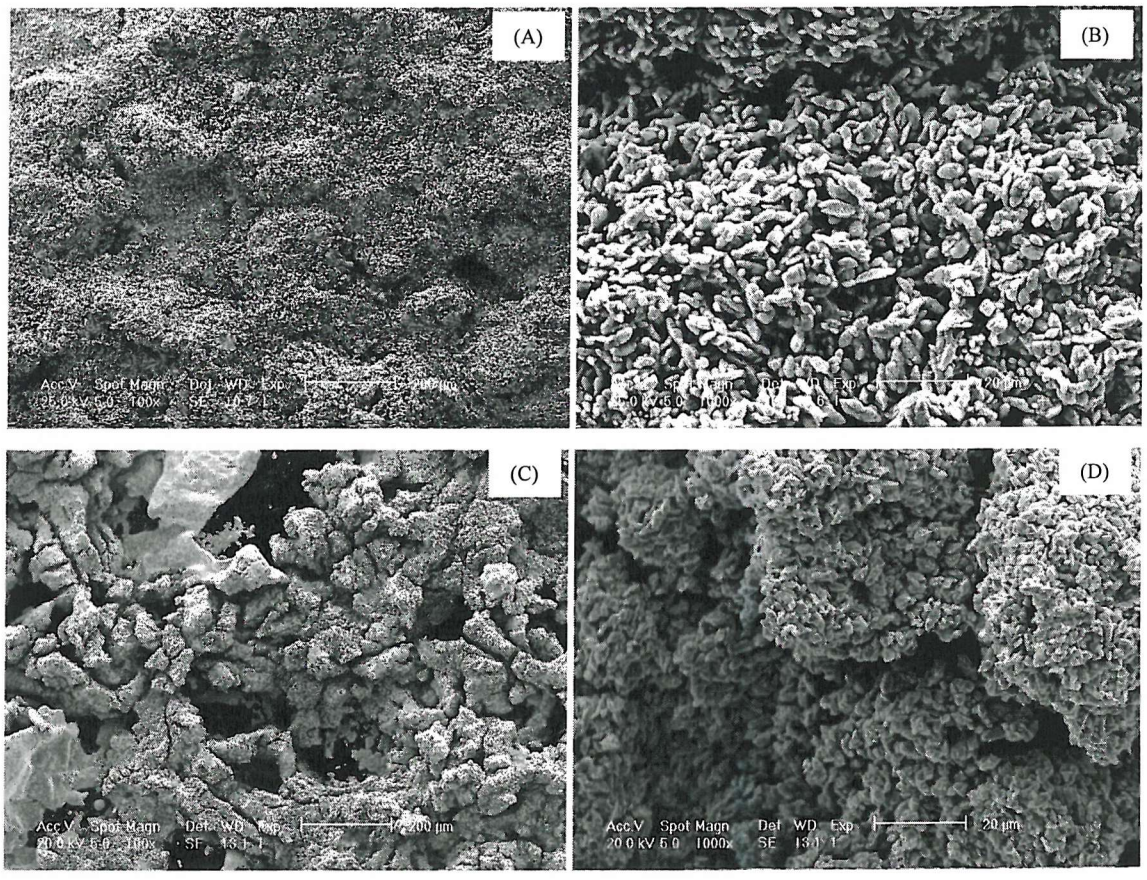

Figure 6.14: *SEM images of PbO_2 electrodes (Type IV), following repeated cycling, with: (A + B) No additive and (C + D) 1 g dm^{-3} sodium ligninsulfonate.*

A series of charge / discharge experiments was performed with the cell containing type III (RVC foam) electrodes (for both the Pb and PbO_2 electrodes) where the electrolyte contained $Pb(CH_3SO_3)_2$ (1.5 mol dm^{-3}) in aqueous CH_3SO_3H (0.9 mol dm^{-3}) with various concentrations of sodium ligninsulfonate (0 g dm^{-3}, 0.2 g dm^{-3}, 1.0 g dm^{-3} and 5.0 g dm^{-3}). The electrolyte reservoir was thermostated at 298 K and charged with 40 cm^3 of solution. The interelectrode gap was set at 1.6 cm and the linear flow rate across the electrode surface was 2.5 cm s^{-1}. A current density of 20 mA cm^{-2} was used for both charge / discharge and electrical connection was made via a screw contact to the reverse of the electrode. Each experiment involved 3 cycles with each cycle consisting of a 1 hour charge followed by discharge to 1.20 V. Each of the experiments showed the characteristic form for charge / discharge of the cell, with figure 6.15 presenting the voltage time profile from the experiment using 1.0 g dm^{-3} sodium lignin sulfonate.

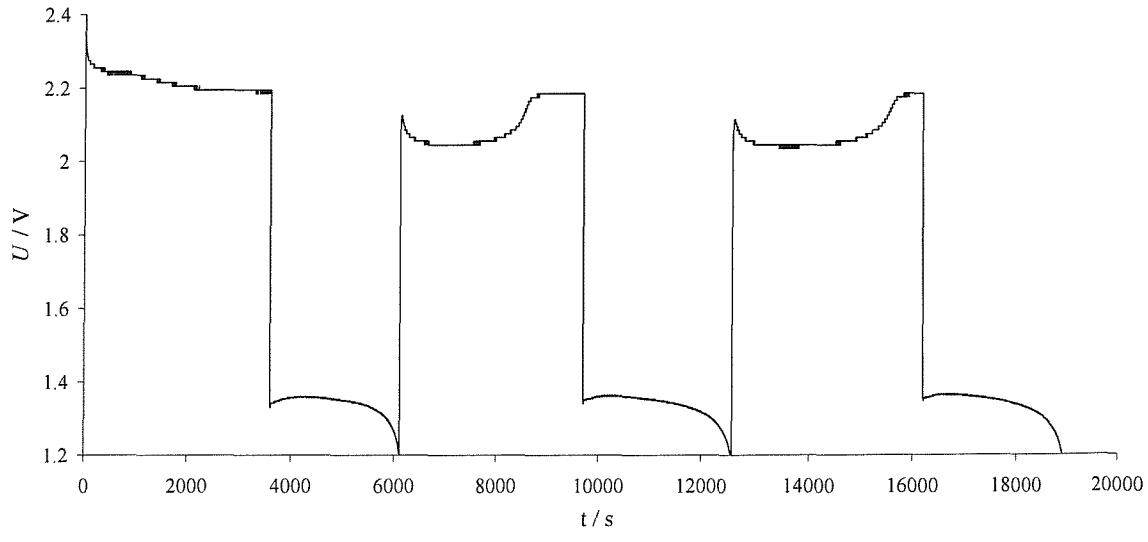

Figure 6.15: *Cell voltage vs. time plot for 3 charge / discharge cycles carried out in the flow cell fitted with type III electrodes and supplied with an electrolyte initially consisting of $Pb(CH_3SO_3)_2$ (1.5 mol dm^{-3}) and sodium ligninsulfonate (1.0 g dm^{-3}) in aqueous CH_3SO_3H (0.9 mol dm^{-3}). The interelectrode gap was set at 1.60 cm and the linear flow rate across the electrode surfaces was 2.5 cm s^{-1}. A current density of 20 mA cm^{-2} was used with an electrolyte temperature of 298 K.*

Table 6.3 presents voltage and efficiency data for the third cycle of each of the 1 hour charge / discharge experiments. It can be seen that with increasing sodium

ligninsulfonate concentration the difference between charge and discharge voltages increases. The efficiencies drop only slightly with the lower additive concentrations, however with 5.0 g dm^{-3} sodium ligninsulfonate there is a considerably more detrimental effect on the cell efficiencies.

Sodium Ligninsulfonate / g dm^{-3}	$\bar{U}_c$ / V	$\bar{U}_d$ / V	$\frac{Q_d}{Q_c}$ / %	$\frac{W_d}{W_c}$ / %
0	1.98	1.38	77	53
0.2	1.97	1.41	56	40
1.0	2.08	1.34	75	49
5.0	2.14	1.35	46	29

Table 6.3: *Voltage and efficiency data for the third cycle in a series of 1 hour charge / discharge experiments carried out in the flow cell fitted with type III electrodes and supplied with an electrolyte initially consisting of $Pb(CH_3SO_3)_2$ (1.5 mol dm^{-3}) and various concentrations of sodium ligninsulfonate in aqueous CH_3SO_3H (0.9 mol dm^{-3}). The interelectrode gap was set at 1.60 cm and the linear flow rate across the electrode surfaces was 2.5 cm s^{-1}. A current density of 20 mA cm^{-2} was used with an electrolyte temperature of 298 K.*

The cell was supplied with an electrolyte containing $Pb(CH_3SO_3)_2$ (1.5 mol dm^{-3}) in aqueous CH_3SO_3H (0.9 mol dm^{-3}). A 4 hour charge / discharge cycle was started, at a current density of 20 mA cm^{-2}, the interelectrode gap was 0.4 cm and the linear flow rate across the electrode surface was 9.5 cm s^{-1}. However approximately 3 hours into the experiment abnormal cell voltages were observed and the experiment stopped. When the cell was dismantled and the electrodes examined, it was seen that the Pb deposit had formed dendritic growths across the interelectrode gap, shorting the cell (see figure 6.1).

The experiment was repeated with the addition of 1.0 g dm^{-3} sodium ligninsulfonate at current densities of 20 mA cm^{-2} and 40 mA cm^{-2}. The voltage vs. time plots for these experiments are shown in figure 6.16. At 20 mA cm^{-2} the average charge and discharge voltages were 2.04 V and 1.56 V respectively. There was a good coulombic efficiency ($\frac{Q_d}{Q_c}$ = 79 %) and energy efficiency ($\frac{W_d}{W_c}$ = 60 %). At 40 mA cm^{-2} the average cell voltage during charge was slightly higher ($\bar{U}_c$ = 2.14 V) while the average discharge was slightly

lower ($\bar{U}_d$ = 1.54 V) which is expected and is probably a result of increased *IR* drop. The coulombic and energy efficiencies were also slightly lower ($\frac{Q_d}{Q_c}$ = 65 % and $\frac{W_d}{W_c}$ = 47 %) than at 20 mA cm^{-2}. However it should be noted that charging at 40 mA cm^{-2} corresponds to storing double the amount of charge. In fact charging for 4 hours at 40 mA cm^{-2} corresponds to the storage of 576 C cm^{-2}.

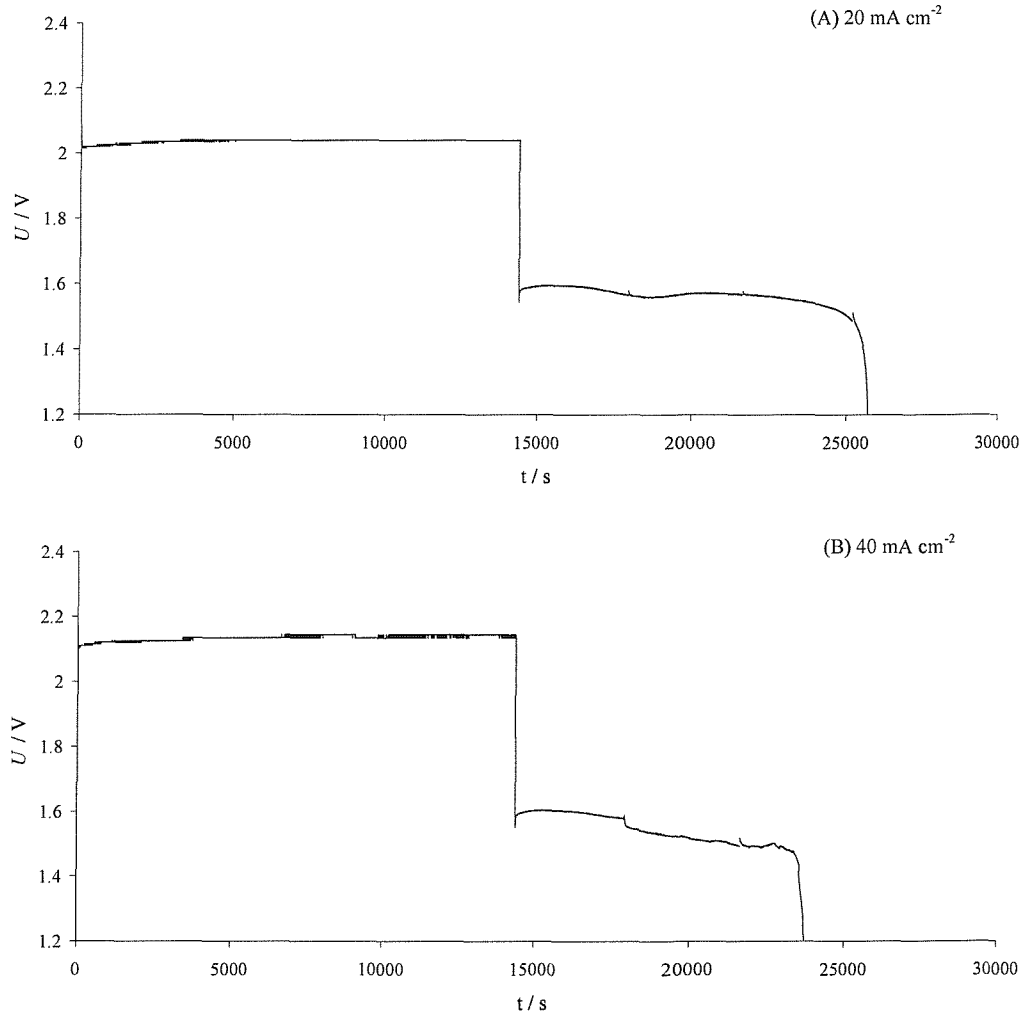

Figure 6.16: *Cell voltage vs. time data for two experiments, each involving a single charge / discharge cycle of the flow cell. Interelectrode gap: 0.4 cm, linear flow rate across the electrode surface: 10 cm s^{-1}. Electrolyte initially $Pb(CH_3SO_3)_2$ (1.5 mol dm^{-3}) and sodium ligninsulfonate (1 g dm^{-3}) in aqueous CH_3SO_3H (0.9 mol dm^{-3}). Temperature 298 K. (A) Current density = 20 mA cm^{-2}. (B) Current density = 40 mA cm^{-2}. Both experiments discharged at charging current density until voltage dropped to 1.20 V.*

6.3 Nickel (II)

6.3.1 Choosing Nickel (II) as an Additive: It has been observed that PbO_2 deposits from acidic media have different characteristics if Ni^{2+} is present in the solution.[111] A series of cyclic voltammograms was recorded at a vitreous carbon RDE (ω = 400, 900, 1600 and 2500 rpm) in an aqueous CH_3SO_3H (0.9 mol dm^{-3}) solution containing $Pb(CH_3SO_3)_2$ (1.5 mol dm^{-3}) and various concentrations of nickel carbonate (n = 0.1 g dm^{-3}, 1.0 g dm^{-3}, 5.0 g dm^{-3} and 10 g dm^{-3}). Experiments were performed at 298 K and with a scan rate of 50 mV s^{-1} and between potential limits of 0.0 V vs. SCE and 1.85 V vs. SCE. All of the voltammograms showed the characteristic response for the Pb^{2+}/PbO_2 couple in methanesulfonic acid. Table 6.4 presents the current density, at 1.90 V vs. SCE, for PbO_2 deposition (j_{anodic} / mA cm^{-2}), peak current density for PbO_2 dissolution ($j_{cathodic}$ / mA cm^{-2}), nucleation overpotential ($\eta_{nucl.}$ / mV) and charge efficiency ($\frac{Q_{cathodic}}{Q_{anodic}}$ / %) for the voltammograms recorded at 900 rpm. All of the voltammograms with Ni show a lower overpotential for the nucleation of PbO_2, however this is offset by modest charge efficiencies.

Nickel Carbonate / g dm^{-3}	j_{anodic} / mA cm^{-2}	$j_{cathodic}$ / mA cm^{-2}	$\eta_{nucl.}$ / mV	$\frac{Q_{cathodic}}{Q_{anodic}}$ / %
0	85.0	90.7	296	85
0.1	106	51.9	263	31
1.0	105	41.5	255	26
5.0	107	50.7	258	36
10	111	30.0	229	18

Table 6.4: *Data from cyclic volammograms of the Pb^{2+}/PbO_2 couple recorded at a vitreous carbon RDE (ω = 900). Electrolyte comprised of $Pb(CH_3SO_3)_2$ (1.5 mol dm^{-3}) in aqueous CH_3SO_3H (0.9 mol dm^{-3}) and various quantities of nickel carbonate additive. Temperature 298 K, scan rate of 50 mV s^{-1}.*

6.3.2 Nickel (II) in the Flow Cell: A series of charge / discharge experiments were performed, in the flow cell. Each experiment consisted of 6 cycles, each comprised of a 900

s charge (j = 20 mA cm^{-2}) followed by discharge, at the same current density, until the voltage dropped to 1.20 V. Supplying the cell was a thermostated reservoir (298 K) containing 40 cm^3 of an electrolyte consisting of $Pb(CH_3SO_3)_2$ (1.5 mol dm^{-3}) and various concentrations of nickel (II) (0 g dm^{-3}, 0.1 g dm^{-3}, 1.0 g dm^{-3}, 5.0 g dm^{-3} and 10 g dm^{-3}), prepared by the addition of nickel (II), in aqueous CH_3SO_3H (0.9 mol dm^{-3}). The interelectrode gap was set at 0.4 cm and the linear flow rate across the electrode surfaces was 9.5 cm s^{-1}. Type II and type IV electrodes were used for the negative and positive electrodes respectively. The voltage vs. time plots for each of the experiments were consistent in form with those reported previousely.

Nickel Carbonate / g dm^{-3}	$\bar{U}_c$ / V	$\bar{U}_d$ / V	$\frac{Q_d}{Q_c}$ / %	$\frac{W_d}{W_c}$ / %
0	1.93	1.54	91	73
0.1	1.88	1.55	80	66
1.0	1.88	1.55	80	66
5.0	1.88	1.55	86	71
10.0	1.86	1.53	74	61

Table 6.5: *Data from the 6th cycle of experiments using the flow cell with various concentrations of nickel carbonate additive. Each experiment involved 6 cycles consisting of a 900 s charge (j = 20 mA cm^{-2}) followed by discharge, at the same current density, until the voltage dropped to 1.20 V. A thermostated reservoir (298 K) containing 40 cm^3 of an electrolyte consisting of $Pb(CH_3SO_3)_2$ (1.5 mol dm^{-3}) and nickel carbonate (0 g dm^{-3}, 0.1 g dm^{-3}, 1 g dm^{-3}, 5 g dm^{-3} and 10 g dm^{-3}) in aqueous CH_3SO_3H (0.9 mol dm^{-3}), was supplied to the cell. The interelectrode gap was set at 0.4 cm and the linear flow rate across the electrode surfaces was 9.5 cm s^{-1}. Type II and type IV electrodes were used for the negative and positive electrodes respectively.*

Table 6.5 presents the average charge voltage ($\bar{U}_c$ / V), average discharge voltage ($\bar{U}_d$ / V), coulombic efficiency ($\frac{Q_d}{Q_c}$ / %) and the energy efficiency ($\frac{W_d}{W_c}$ / %) for the 6th cycle from each of the experiments. It can be seen that, with nickel (II) in the electrolyte, there is an improvement in the cell voltage, however this is offset by a decrease in both the coulombic and energy efficiencies. It should be noted that the efficiencies obtained with the flow cell (table 6.5) are significantly better than would be predicted from the Pb^{2+}/PbO_2 cyclic voltammograms (table 6.4). The difference may be explained by the experimental

conditions; during the cyclic voltammetry, a thin layer of PbO_2 is rapidly deposited at high current densities (up to circa 100 mA cm^{-2}) and then stripped at current densities up to 50 mA cm^{-2}. However, in the flow cell the deposition and stripping of PbO_2 takes place at a constant current density of 20 mA cm^{-2}.

A series of charge / discharge cycles was performed with the flow cell fitted with type II (Pb) and type IV (PbO_2) electrodes. Each cycle consisted of a 900 s charge (j = 20 mA cm^{-2}) followed by discharge, at the same current density, until the voltage dropped to 1.20 V. The experiment totalled 84 complete cycles followed by a final 900 s charge. The cell was supplied with an electrolyte initially containing $Pb(CH_3SO_3)_2$ (1.5 mol dm^{-3}) and nickel carbonate (1.0 g dm^{-3}) in aqueous CH_3SO_3H (0.9 mol dm^{-3}).

Figure 6.17 shows the voltage vs. time plots for the 1^{st} – 6^{th}, 43^{rd} – 48^{th} and 79^{th} – 84^{th} cycles of the cell. The profile of the plots is consistent with cycles performed without additive; constant voltages for charge and discharge during the first cycle, with a voltage trough appearing in the second and subsequent charges. With the presence of the nickel (II), the coulombic efficiency, from the 3^{rd} cycle onwards, remained steady at circa 80 % and the energy efficiency increased from around 65 % during the initial cycles to circa 75 % for the final cycles. The average voltages during charge ($\bar{U}_c$ = 1.84 V) and discharge ($\bar{U}_d$ = 1.56) for the final cycle are similar to those observed without the additive being present, in fact $\bar{U}_c$ - $\bar{U}_d$ = 290 mV with the addition of 1.0 g dm^{-3} nickel (II) compared with a value of 280 mV without the use of additive. It should be noted that these values are significantly better than those quoted in table 6.5 for 1.0 g dm^{-3} nickel (II) ($\bar{U}_c$ - $\bar{U}_d$ = 350 mV). This is due to a gradual improvement in the overpotentials associated with charge and discharge over the course of the 84 cycles.

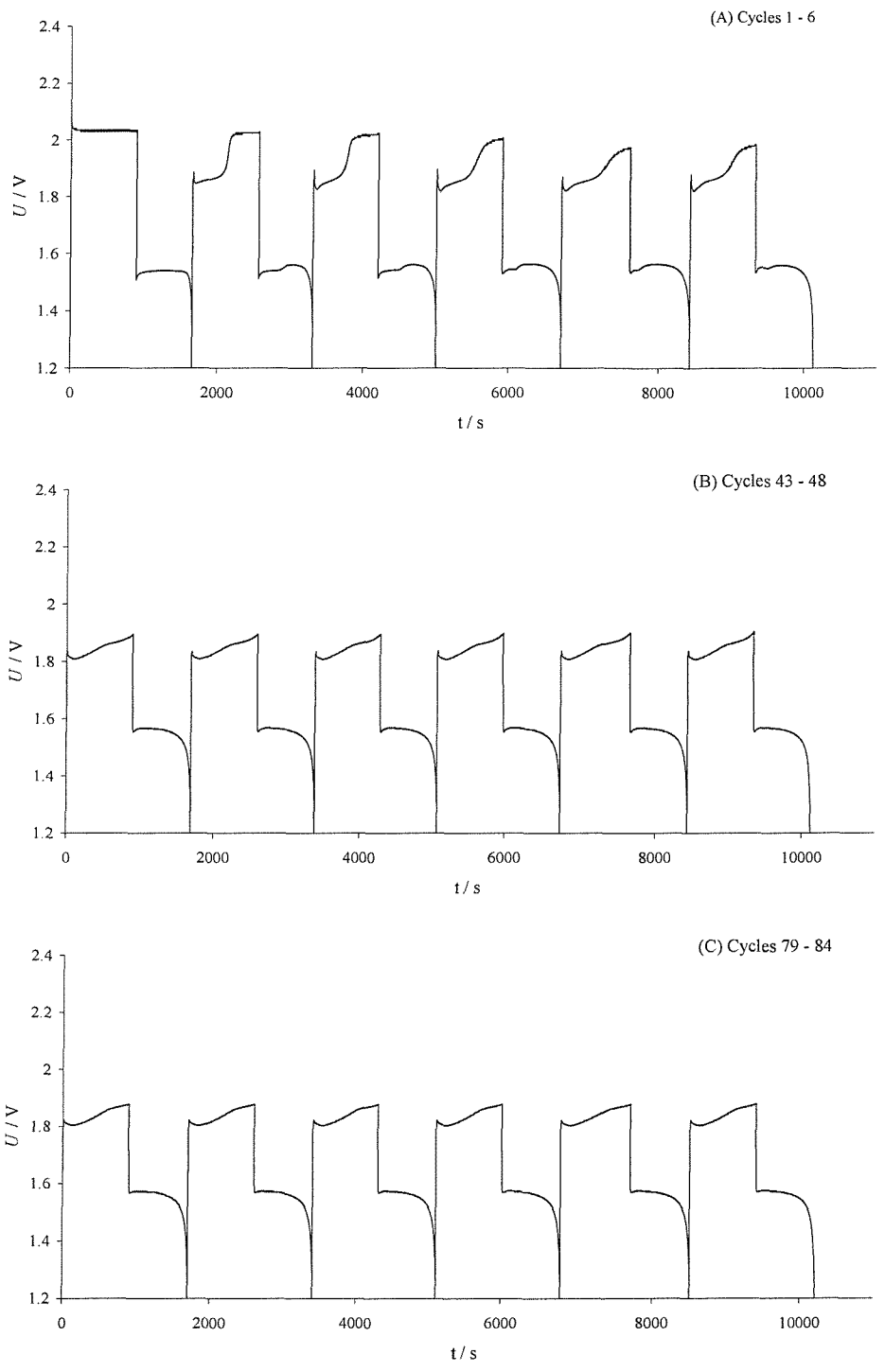

Figure 6.17 : *Cell voltage vs. time data for various points in a series of 84 charge / discharge cycles of the flow cell. Each cycle consisted of a 900 s charge at 20 mA cm^{-2} followed by discharge, at the same current density, until the voltage dropped to 1.20 V. The electrolyte initially consisted of $Pb(CH_3SO_3)_2$ (1.5 mol dm^{-3}) and nickel (II) (1.0 g dm^{-3}) in aqueous CH_3SO_3H (0.9 mol dm^{-3}). (A) cycles 1 – 6, (B) cycles 43 – 48, (C) cycles 79 – 84.*

6.4 Combining Nickel Carbonate and Sodium Ligninsulfonate

The cell was supplied with an electrolyte containing $Pb(CH_3SO_3)_2$ (1.5 mol dm^{-3}), sodium ligninsulfonate (1.0 g dm^{-3}) and nickel (II) (1.0 g dm^{-3}) in aqueous CH_3SO_3H (0.9 mol dm^{-3}). A 4 hour charge / discharge cycle was then performed, at a current density of 20 mA cm^{-2}, the interelectrode gap was 0.4 cm and the linear flow rate across the electrode surface was 9.5 cm s^{-1}. The experiment was repeated at a current density of 40 mA cm^{-2}. The voltage vs. time plots for these experiments are shown in figure 6.18. The voltages, coulombic efficiency and energy efficiency obtained did not alter significantly from those obtained in similar experiments with the addition of only sodium ligninsulfonate (section 6.3.2).

A series of charge / discharge cycles was performed with the flow cell fitted with type II (negative) and type IV (positive) electrodes. Each cycle consisted of a 900 s charge (j = 20 mA cm^{-2}) followed by discharge, at the same current density, until the voltage dropped to 1.20 V. The experiment totalled 84 complete cycles followed by a final 900 s charge. The cell was supplied with an electrolyte initially containing $Pb(CH_3SO_3)_2$ (1.5 mol dm^{-3}), sodium ligninsulfonate (1 g dm^{-3}) and nickel carbonate (1 g dm^{-3}) in aqueous CH_3SO_3H (0.9 mol dm^{-3}).

Figure 6.19 shows the voltage vs. time plots for the 1^{st} – 6^{th}, 43^{rd} – 48^{th} and 79^{th} – 84^{th} cycles of the cell. The profile of the plots is consistent with cycles performed without additive; constant voltages for charge and discharge during the first cycle, with a voltage trough appearing in the second and subsequent charges. The coulombic efficiency dropped from circa 80 % to circa 77 % over the 84 cycles. The energy efficiency, however, remained relatively steady, at circa 67 %, between the initial and final cycles.

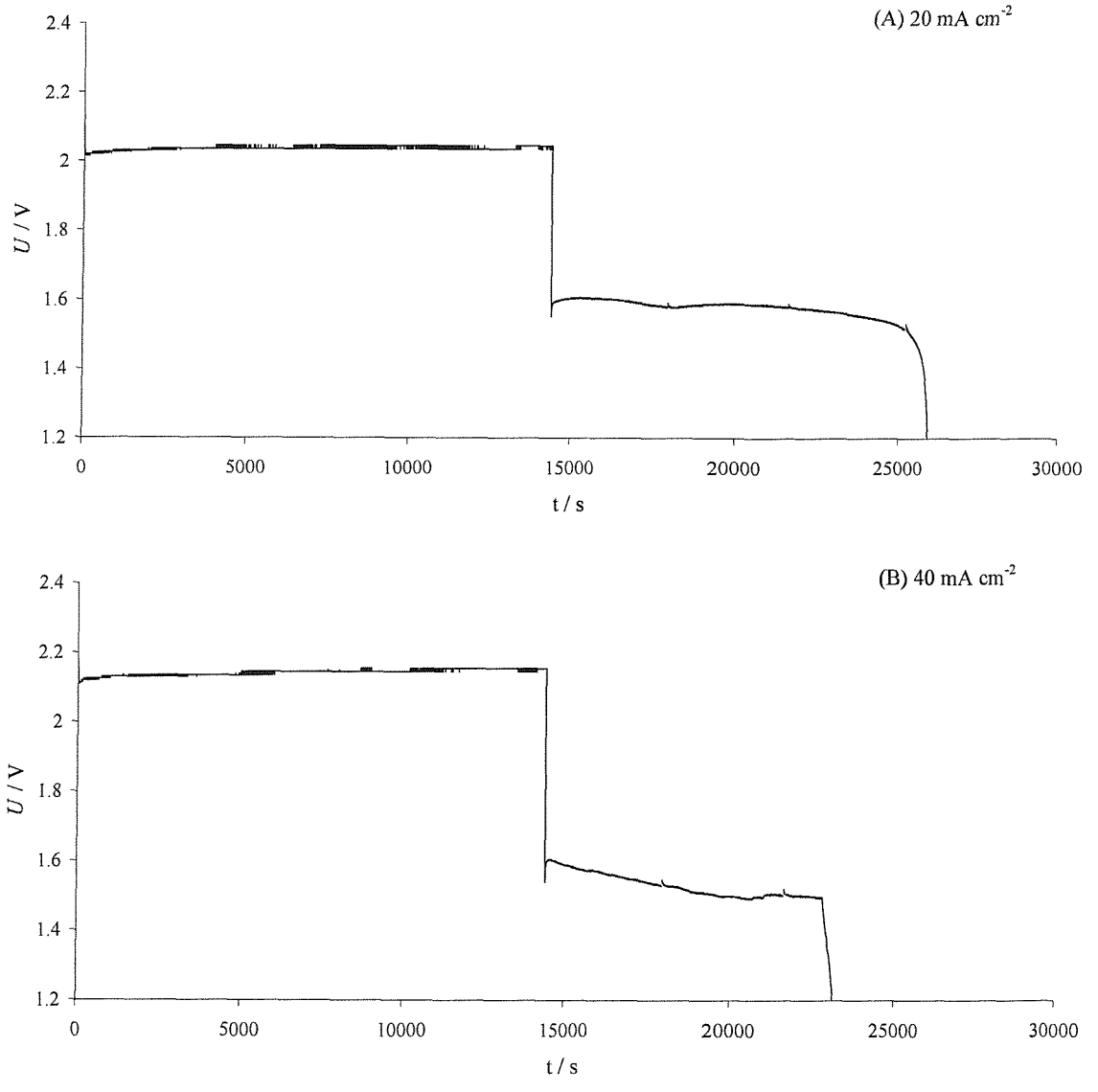

Figure 6.18: *Cell voltage vs. time data for two experiments, each involving a single charge / discharge cycle of the flow cell. Interelectrode gap: 0.4 cm, linear flow rate across the electrode surface: 20 cm s-1. Electrolyte initially $Pb(CH_3SO_3)_2$ (1.5 mol dm^{-3}) and sodium ligninsulfonate (1 g dm^{-3}) in aqueous CH_3SO_3H (0.9 mol dm^{-3}). Temperature 298 K. (A) Current density = 20 mA cm^{-2}. (B) Current density = 40 mA cm^{-2}. Both experiments discharged at charging current density until voltage dropped to 1.20 V.*

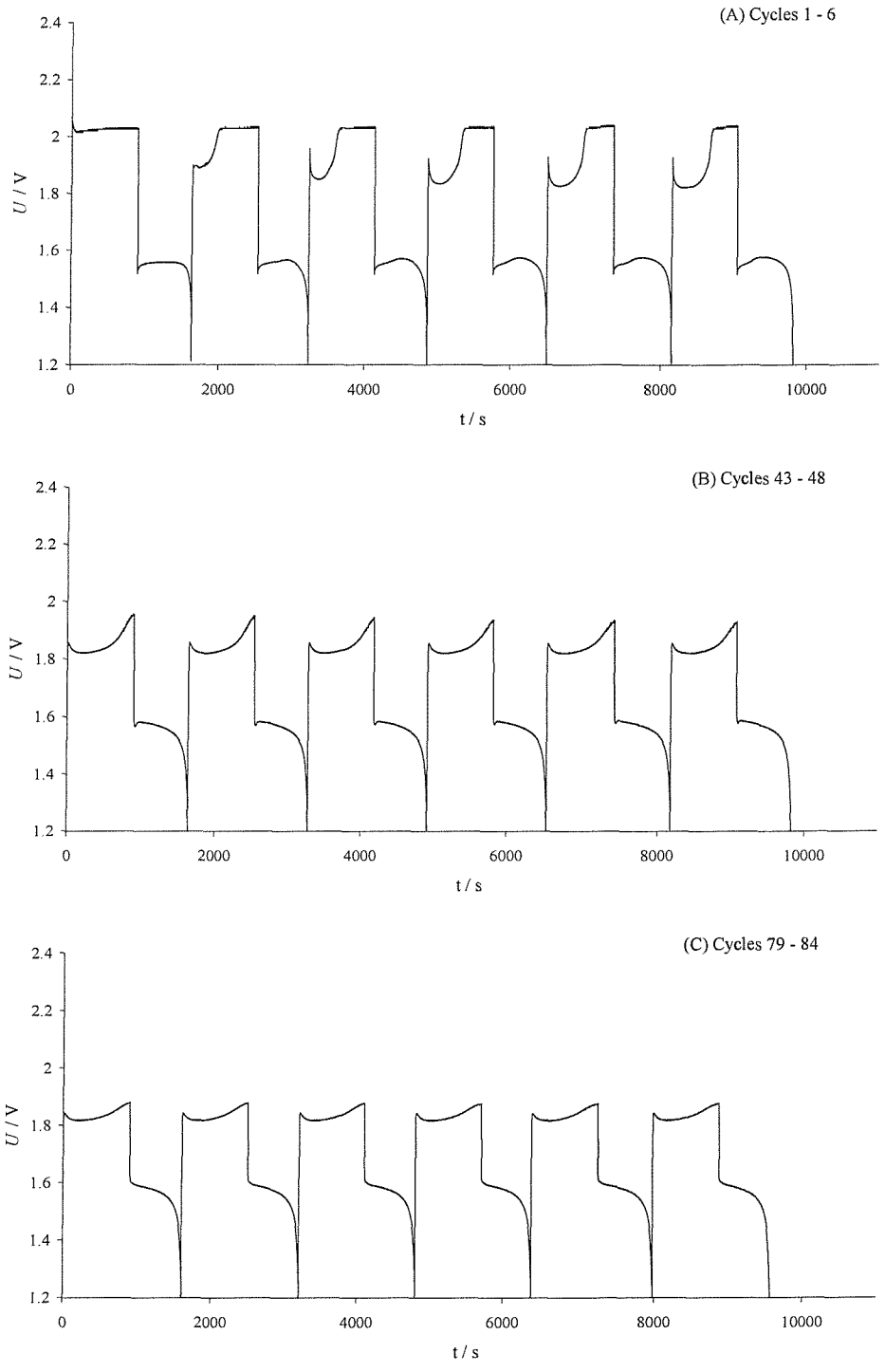

Figure 6.19: *Cell voltage vs. time data for various points in a series of 84 charge / discharge cycles of the flow cell. Each cycle consisted of a 900 s charge at 20 mA cm^{-2} followed by discharge, at the same current density, until the voltage dropped to 1.20 V. The electrolyte initially consisted of $Pb(CH_3SO_3)_2$ (1.5 mol dm^{-3}), nickel carbonate (1.0 g dm^{-3}) and sodium ligninsulfonate (1.0 g dm^{-3}) in aqueous CH_3SO_3H (0.9 mol dm^{-3}). (A) cycles 1 – 6, (B) cycles 43 – 48, (C) cycles 79 – 84.*

6.5 Alternative Additives and Electrolytes

6.5.1 Alternative additives: It has been suggested that Fe^{3+} may aid the deposition/dissolution of PbO_2.[82] Cyclic voltammograms investigating the Pb^{2+}/Pb and Pb^{2+}/PbO_2 couples were performed at a vitreous carbon RDE (ω = 1600 rpm) from an electrolyte solution containing $Pb(CH_3SO_3)_2$ (1.5 mol dm^{-3}) and Fe^{3+} (0 g dm^{-3}, 0.1 g dm^{-3}, 5 g dm^{-3} and 10 g dm^{-3}) in aqueous CH_3SO_3H (0.9 mol dm^{-3}). The electrolyte was maintained at 298 K and the potential scan rate was 25 mV s^{-1}. The voltammograms of both electrode couples were unaffected by the presence of the Fe in solution and no differences in current densities, overpotentials or charge efficiencies were observed compared to the voltammograms obtained without Fe present.

Preliminary investigations of polyethylene glycol-200 as an alternative for sodium ligninsulfonate were performed. A series of cyclic voltammograms probing the Pb^{2+}/Pb electrode couple were recorded at a nickel RDE (ω = 1600 rpm) from an electrolyte solution comprising $Pb(CH_3SO_3)_2$ (4 mmol dm^{-3}) in aqueous CH_3SO_3H (2.0 mol dm^{-3}) with the addition of various concentrations of polyethylene glycol-200. The potential was scanned at 50 mV s^{-1} between -300 mV sv. SCE and -650 mV vs. SCE. The temperature was maintained at 298 K. Figure 6.20 compares cyclic voltammograms obtained with the electrolyte solution additionally containing 1.0 g dm^{-3} polyethylene glycol-200 (figure 6.20 A) and 25 g dm^{-3} polyethylene glycol-200 (figure 6.20 B).

The voltammogram obtained with the addition of 1.0 g dm^{-3} polyethylene glycol-200 is comparable to similar voltammograms obtained without additive (figure 3.3). Scanning to negative potentials a sharp reduction wave, associated with the deposition of Pb onto the electrode surface, commencing at -520 mV vs. SCE is observed (cf. -510 mV vs. SCE without additive) leading to a plateau current density (j_L = -5.5 mA cm^{-2}). On the reverse scan the deposition continues to -475 mV vs. SCE giving a nucleation overpotential, $\eta_{nucl.}$, of 45 mV ($\eta_{nucl.}$ = 35 mV without the use of additive). As the potential is scanned further in the positive direction the current becomes anodic and a stripping peak is observed. Compared with the same concentration of lignin sulfonate (figure 6.2) the reduction wave is less draw out and the kinetics of the Pb^{2+}/Pb couple are much faster. As the concentration of polyethylene glycol is increased, the overpotential increases and the

reduction wave for Pb deposition becomes more drawn out. Also, the limiting current density decreases. The voltammogram obtained using 25 g dm^{-3} polyethylene glycol-200 (figure 6.20 B) gives an overpotential of 78 mV and limiting current density of -3.4 mA cm^{-2}. This is due to an increase in viscosity,

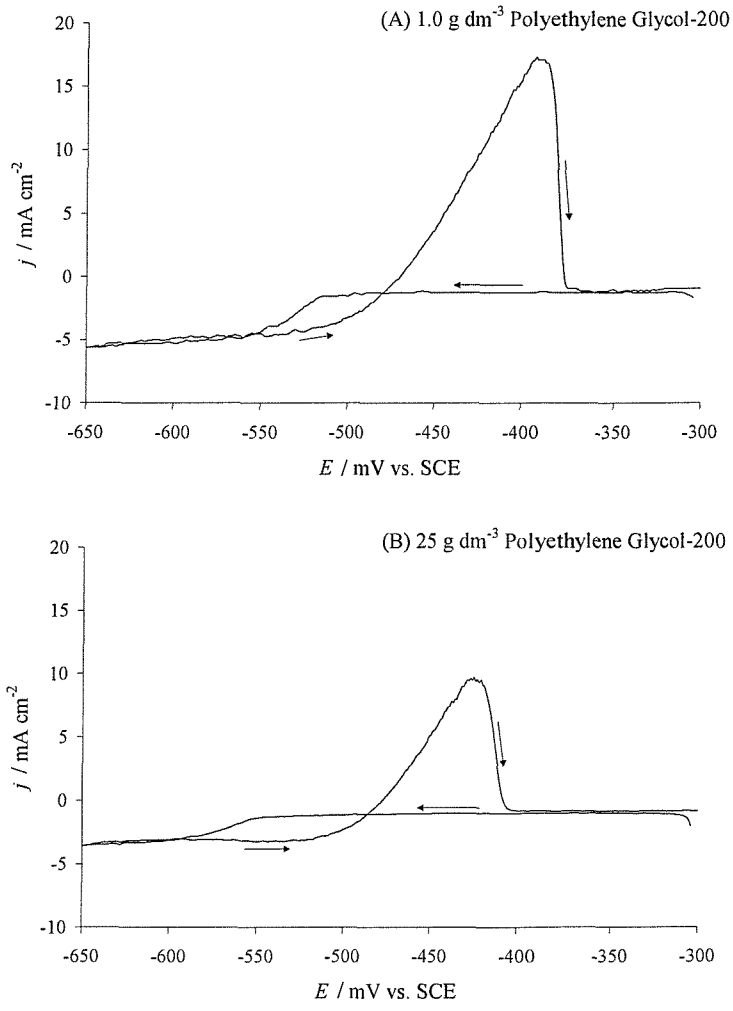

Figure 6.20: *Cyclic voltammograms of the Pb^{2+}/Pb couple performed at a nickel RDE (ω = 1600 RPM) between potential limits of -300 mV vs. SCE and -650 mV vs. SCE at a scan rate of 50 mV s^{-1}. The electrolyte solution contained $Pb(CH_3SO_3)_2$ (4 mmol dm^{-3}) in aqueous CH_3SO_3H (2.0 mol dm^{-3}). The temperature was maintained at 298 K. (A) with the addition of 0.1 g dm^{-3} polyethylene glycol-200; (B) 25 g dm^{-3} polyethylene glycol-200.*

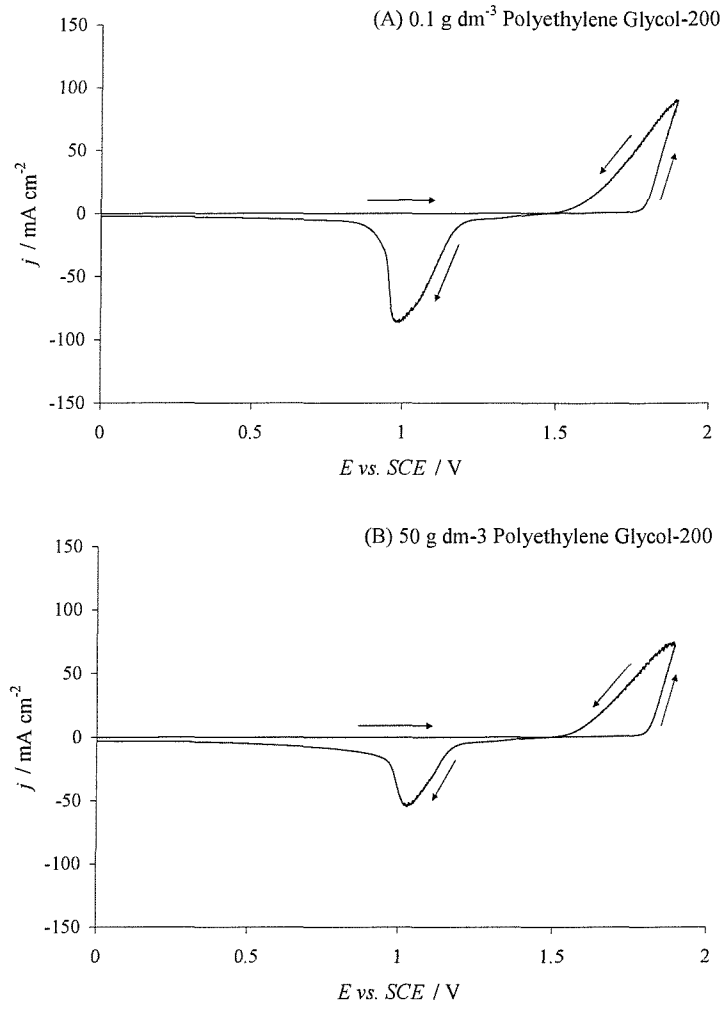

Figure 6.21: *Cyclic voltammograms of the Pb^{2+}/PbO_2 couple performed at a vitreous carbon RDE (ω = 1600 RPM) between potential limits of 0.0 V vs. SCE and 1.90 V vs. SCE at a scan rate of 50 mV s^{-1}. The electrolyte solution contained $Pb(CH_3SO_3)_2$ (1.5mol dm^{-3}) in aqueous CH_3SO_3H (0.9 mol dm^{-3}). The temperature was maintained at 298 K. (A) with the addition of 0.1 g dm^{-3} polyethylene glycol-200; (B) 50 g dm^{-3} polyethylene glycol-200.*

A series of cyclic voltammograms of the Pb^{2+}/PbO_2 couple were recorded at a vitreous carbon RDE (ω = 1600 rpm) from a solution containing $Pb(CH_3SO_3)_2$ (1.5 mol dm^{-3}) in aqueous CH_3SO_3H (0.9 mol dm^{-3}) and various concentrations of polyethylene glycol-200 (0.1, 0.5, 5, 25 and 50 g dm^{-3}). The potential was cycled between 0 V vs. SCE and 1.90 V vs. SCE with a scan rate of 50 mV s^{-1}. Figure 6.21 presents the voltammograms obtained with the addition of 0.1 g dm^{-3} and 50 g dm^{-3} polyethylene glycol-200. With the addition of 0.1 g dm^{-3} polyethylene glycol-200 the voltammogram is not significantly different to the

response obtained without additive. With the 50 g dm^{-3} polyethylene glycol-200, however, there is an increase in the nucleation overpotential and a lowering in current densities along with lower current efficiencies. Table 6.6 shows the nucleation overpotential ($\eta_{nucl.}$ / mV), current density at 1.85 V vs. SCE (j_{anodic} / mA cm^{-2}), peak current density for PbO_2 stripping ($j_{cathodic}$ / mA cm^{-2}) and charge efficency ($\frac{Q_{cathodic}}{Q_{anodic}}$ / %). With increasing polyethylene glycol-200 concentration the current densities drop, the nucleation overpotential increases and the charge efficiency drops. The overpotential and charge efficiencies compare well with values obtained at 900 rpm (table 6.1) and 1600 rpm with the use of sodium ligninsulfonate.

Polyethylene Glycol-200 Concentration / g dm^{-3}	j_{anodic} / mA cm^{-2}	$j_{cathodic}$ / mA cm^{-2}	$\eta_{nucl.}$ / mV	$\frac{Q_{cathodic}}{Q_{anodic}}$ / %
0.0	98.6	99.6	310	80
0.1	88.4	87.8	311	81
0.5	79.3	66.6	316	82
5.0	83.3	74.4	322	80
25	78.2	61.7	326	73
50	74.0	51.1	327	67

Table 6.6: *Data from cyclic voltammograms recorded at a vitreous carbon RDE rotating at 1600 rpm. The electrolyte comprised $Pb(CH_3SO_3)_2$ (1.5 mol dm^{-3}) in aqueous CH_3SO_3H (0.9 mol dm^{-3}) with various concentrations of polyethylene glycol-200 additive. Voltammograms recorded between potential limits of 0.0 V vs. SCE and 1.90 V vs. SCE, at a scan rate of 50 mV s^{-1}. Temperature 298 K. Current densities at 1.90 V vs. SCE for PbO_2 deposition, peak current densities for PbO_2 dissolution, nucleation overpotential and charge efficiency.*

A series of Pb depositions were carried out on a nickel rotating disc electrode (ω = 900 rpm) from an electrolyte solution containing $Pb(CH_3SO_3)_2$ (0.3 mol dm^{-3}) in aqueous CH_3SO_3H (2.0 mol dm^{-3}) with the addition of various quantities of polyethylene glycol-200. The Pb layers were deposited using a current density of -50 mA cm^{-2} for a time period of 600 s. The electrolyte was maintained at 298 K. The deposits obtained with the addition of between 1.0 g dm^{-3} and 50 g dm^{-3} polyethylene glycol-200 were indistinguishable in appearance. Figure 6.22 presents an SEM image of the deposit obtained from an electrolyte solution additionally containing 50 g dm^{-3} polyethylene glycol-200. It can be seen that,

even with high concentrations of polyethylene glycol-200, the resultant deposit shows a significant edge effect and is no smoother than deposits obtained without the use of the additive (cf. figure 6.3).

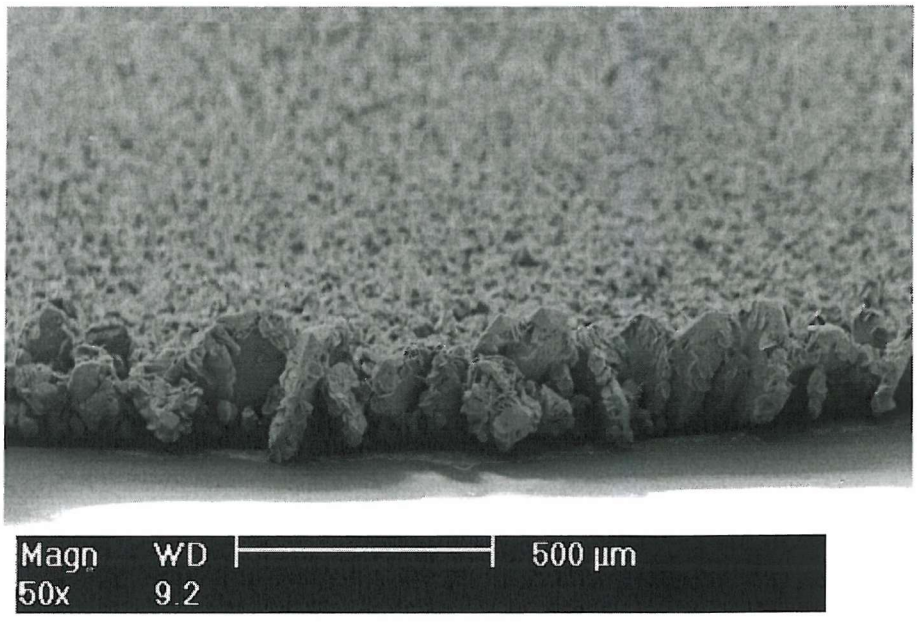

Figure 6.22: *SEM image of a Pb deposit on a vitreous carbon RDE (ω = 900 RPM). A current density of 50 mA cm^{-2} for 600 s was used to deposit the layer, with an electrolyte temperature of 298 K. The electrolyte consisted of $Pb(CH_3SO_3)_2$ (0.3 mol dm^{-3}) and polyethylene glycol-200 (50 g dm^{-3}) in aqueous CH_3SO_3H (2.0 mol dm^{-3}).*

6.5.2 Preliminary investigation of Alternative Electrolytes: Some preliminary experiments were carried out in nitrate, acetate and plumbate media to determine their suitability as alternatives to methanesulfonic acid. Pb^{2+} concentrations of 0.5 mol dm^{-3} were readily obtainable in all of the acidic electrolytes ([acid] = 0.6 mol dm^{-3}), however in the basic, plumbate solution a Pb^{2+} concentration of 0.1 mol dm^{-3} was used due to a lower solubility of Pb^{2+} in aqueous NaOH (4.6 mol dm^{-3}).

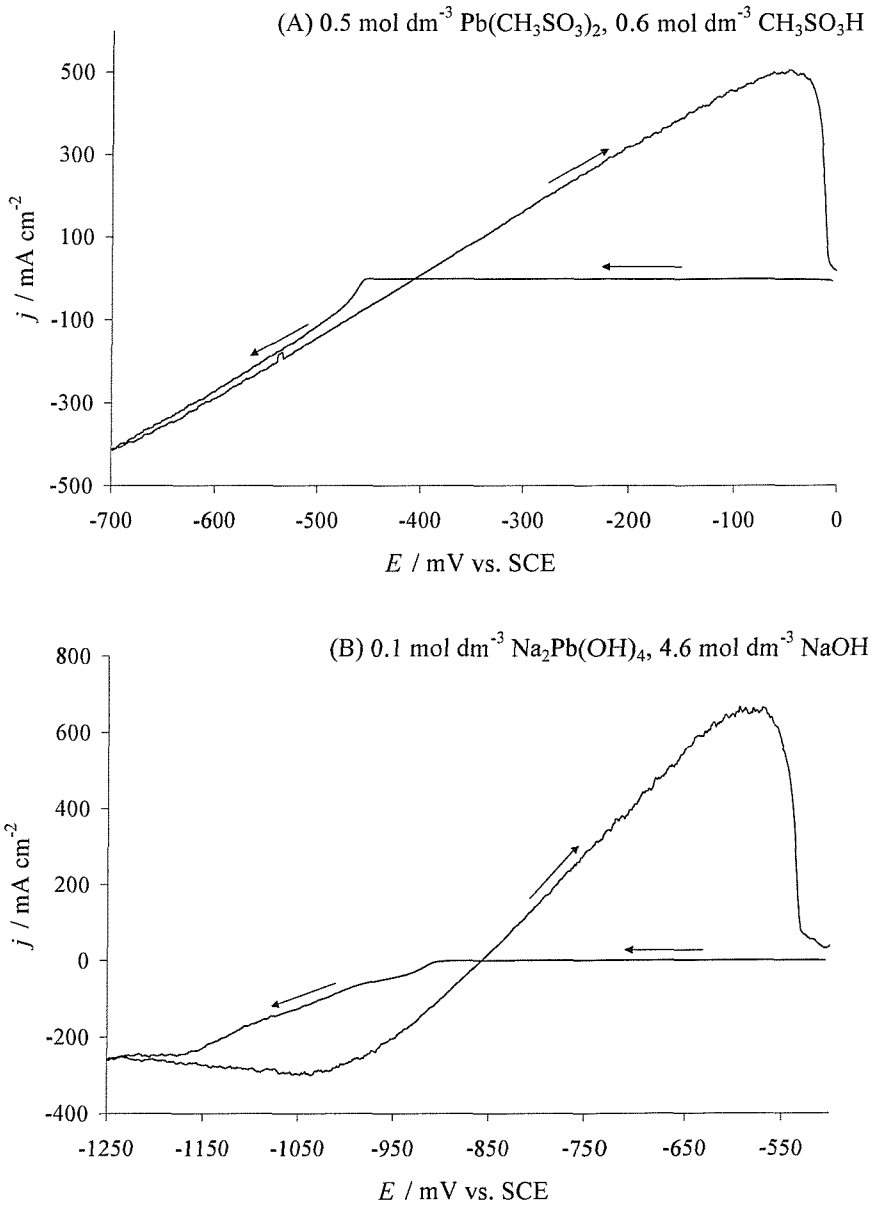

Figure 6.23: *Cyclic voltammograms of the Pb^{2+}/Pb couple obtained using electrolyte solutions comprising:* ***(A)*** *$Pb(CH_3SO_3)_2$ (0.5 mol dm^{-3}) in aqueous CH_3SO_3H (0.6 mol dm^{-3}),* ***(B)*** *$Na_2Pb(OH)_4$ (0.1 mol dm^{-3}) in aqueous NaOH (4.6 mol dm^{-3}). Voltammograms performed at a vitreous carbon RDE (ω = 900 rpm) using a scan rate of 25 mV s^{-1}. Temperature = 298 K.*

Cyclic voltammograms were recorded, using a scan rate of 25 mV s^{-1}, at a vitreous carbon RDE over the potential range in which the Pb^{2+}/Pb couple was active for each of the electrolytes tested. The experiments were performed using an SCE reference electrode and

a rotation rate of 900 rpm. The temperature was maintained at 298 K. Due to the high concentration of Pb each of the voltammograms was heavily distorted by uncompensated resistance. The voltammograms obtained from acidic electrolytes were all of similar form: a cathodic reduction wave commencing at circa -450 mV vs. SCE showing straight line, ohms law characteristics, which on the reverse scan followed back on itself, with the current becoming anodic at circa -410 mV vs. SCE. Current densities, measured at -700 mV vs. SCE, of 440 mA cm^{-2}, 650 mA cm^{-2} and -80 mA cm^{-2} were recorded respectively for the $Pb(CH_3SO_3)_2$, $Pb(NO_3)_2$ and $Pb(CH_3CO_2)_2$ containing electrolytes. In the plumbate electrolyte the voltammogram was again distorted by uncompensated IR drop, but did show some features associated with mass transport controlled kinetics. A cathodic wave corresponding to the reduction of Pb^{2+} to Pb commenced at circa -910 mV vs. SCE. This wave was drawn out but reached a plateau current (j_L = -250 mA cm^{-2}). On the reverse scan Pb deposition continued to -855 mV vs. SCE at which point the current became anodic and a stripping peak was observed. Figure 6.23 shows the voltammograms obtained using electrolyte solutions comprised of: (A) $Pb(CH_3SO_3)_2$ (0.5 ml dm^{-3}) in aqueous CH_3SO_3H (0.5 mol dm^{-3}) and (B) $Na_2Pb(OH)_4$ (0.1 mol dm^{-3}) in NaOH (4.6 mol dm^{-3}).

Cyclic voltammograms were recorded, using a scan rate of 25 mV s^{-1}, at a vitreous carbon RDE over the potential range in which the Pb^{2+}/PbO_2 couple was active for each of the electrolytes tested. The experiments were performed using an SCE reference electrode and a rotation rate of 900 rpm, at 298 K. Figure 6.24 compares cyclic voltammograms of the Pb^{2+}/PbO_2 couple obtained from electrolyte solutions comprising: (A) $Pb(CH_3SO_3)_2$ (0.5 mol dm^{-3}) in aqueous CH_3SO_3H (0.6 mol dm^{-3}), (B) $Pb(NO_3)_2$ (0.5 mol dm^{-3}) in aqueous HNO_3 (0.6 mol dm^{-3}), (C) $Pb(CH_3CO_2)_2$ (0.5 mol dm^{-3}) and $NaCH_3CO_2$ (0.6 mol dm^{-3}) in aqueous CH_3CO_2H (0.6 mol dm^{-3}) and (D) $Na_2Pb(OH)_4$ (0.1 mol dm^{-3}) in aqueous NaOH (4.6 mol dm^{-3}).

The voltammogram obtained using the electrolyte containing $Pb(CH_3SO_3)_2$ (0.5 mol dm^{-3}) in aqueous CH_3SO_3H (0.6 mol dm^{-3}) is typical in appearance to the voltammograms obtained from similar solutions, containing different concentrations of $Pb(CH_3SO_3)_2$ and CH_3SO_3H. The voltammogram obtained from a solution consisting of $Pb(NO_3)_2$ (0.5 mol dm^{-3}) in aqueous HNO_3 (0.6 mol dm^{-3}) compared well with voltammogram 6.23 A, both having the same appearance and nucleation overpotential (μ = 250 mV). However, the

$Pb(NO_3)_2$ voltammogram gave higher current densities (j = 280 mA cm^{-2} and 200 mA cm^{-2} for $Pb(NO_3)_2$ and $Pb(CH_3SO_3)_2$ respectively, measured at 1.80 V vs. SCE) and a better charge balance between deposition and stripping of Pb (circa 80 % and 70 % for $Pb(NO_3)_2$ and $Pb(CH_3SO_3)_2$ respectively).

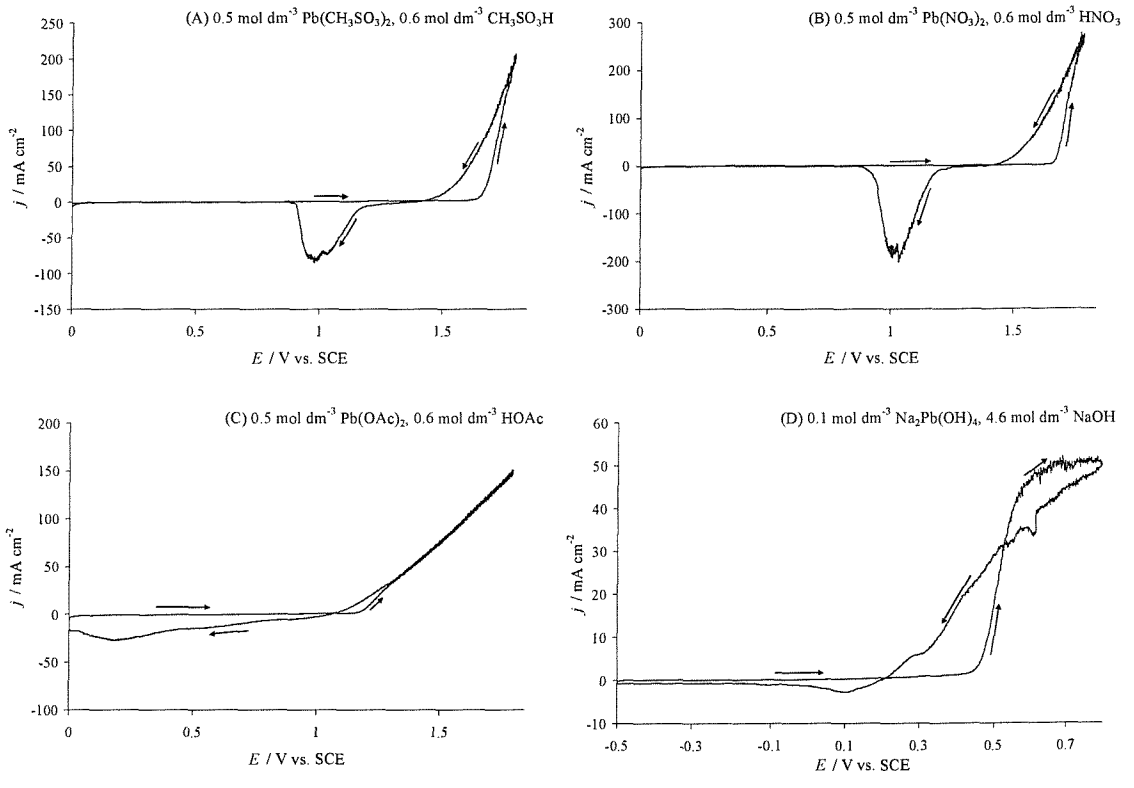

Figure 6.24: *Cyclic voltammograms of the Pb^{2+}/PbO_2 couple obtained using electrolyte solutions comprising:* ***(A)*** *$Pb(CH_3SO_3)_2$ (0.5 mol dm^{-3}) in aqueous CH_3SO_3H (0.6 mol dm^{-3}),* ***(B)*** *$Pb(NO_3)_2$ (0.5 mol dm^{-3}) in aqueous HNO_3 (0.6 mol dm^{-3}),* ***(C)*** *$Pb(CH_3CO_2)_2$ (0.5 mol dm^{-3}) and $NaCH_3CO_2$ (0.6 mol dm^{-3}) in aqueous CH_3CO_2H (0.6 mol dm^{-3}) and* ***(D)*** *$Na_2Pb(OH)_4$ (0.1 mol dm^{-3}) in aqueous NaOH (4.6 mol dm^{-3}). Voltammograms performed at a vitreous carbon RDE (ω = 900 rpm) using a scan rate of 25 mV s^{-1}. Temperature = 298 K.*

The voltammogram obtained using the electrolyte containing $Pb(CH_3CO_2)_2$ (0.5 mol dm^{-3}) and $NaCH_3CO_2$ (0.6 mol dm^{-3}) in aqueous CH_3CO_2H was less encouraging. PbO_2 deposition proceeded at 1.18 V vs. SCE with an overpotential of 140 mV. However the voltammogram was very drawn out with the deposition of PbO_2 appearing to be

dominated by uncompensated IR and no defined stripping peak was evident. In fact the charge efficiency was circa 10 %. The voltammogram obtained from the solution containing $Na_2Pb(OH)_4$ (0.1 mol dm^{-3}) in aqueous NaOH (4.6 mol dm^{-3}) gave a sharp anodic oxidation wave, corresponding to PbO_2 deposition, commencing at 450 mV vs. SCE, leading to a plateau region of current (j_L = 770 mA cm^{-2}) indicating the deposition becomes mass transport controlled. On the reverse scan the deposition of PbO_2 continues to 205 mV vs. SCE, at which point the current becomes cathodic. However there is only a very small stripping peak and the charge efficiency between deposition and stripping of PbO_2 is less than 5 %.

Pb Species	E_c / mV vs. SCE	E_d / mV vs. SCE	$\lvert E_c - E_d \rvert$ / mV	$\frac{Q_d}{Q_c}$ / %
$Pb(CH_3SO_3)_2$	-429	-367	62	97
$Pb(CH_3CO_2)_2$	-557	-389	168	27
$Pb(NO_3)_2$	-435	-374	61	84
$Na_2Pb(OH)_4$	-889	-845	44	91

Table 6.7: *Data from Pb deposition/dissolution experiments (j = 50 mA cm^{-2}) performed at a vitreous carbon rotating disc electrode (ω = 900 rpm). Temperature maintained at 312 K. Table shows the deposition potential (E_c / mV vs. SCE), stripping potential (E_d / mV vs. SCE), the difference between deposition and stripping potentials ($\lvert E_c - E_d \rvert$ / mV) and charge efficiency (Q_d/Q_c / %) from the third cycle of each experiment.*

A series of chronopotentiometric experiments was performed at a vitreous carbon rotating disc electrode (ω = 900 rpm) to investigate the Pb^{2+}/Pb couple in each of the electrolyte solutions. Each experiment involved three deposition/stripping cycles. Each cycle consisted of a 900 s deposition (j = 50 mA cm^{-2}) followed by anodic dissolution at the same current density until the voltage sharply dropped, indicating the deposit had been consumed. The temperature was maintained at 313 K. With each of the electrolytes the form of the voltage vs. time plots were typical for cathodic deposition and anodic stripping of Pb on a vitreous carbon rotating disc electrode (cf. figure 3.6). At the beginning of each deposition a small, nucleation overpotential is observed before a plateau current is reached for the remainder of the deposition. Plateau currents were also observed for the dissolution of the Pb deposit. Table 6.7 presents the deposition potential (E_c / mV vs. SCE), stripping

potential (E_d / mV vs. SCE), the difference between deposition and stripping potentials ($|E_c - E_d|$ / mV) and charge efficiency ($\frac{Q_d}{Q_c}$ / %) from the third cycle of each experiment.

The $Pb(CH_3SO_3)_2$ and $Pb(NO)_3$ containing electrolytes gave similar results, with the $Pb(CH_3SO_3)_2$ solution giving a slightly higher charge efficiency. The results obtained from the $Pb(CH_3CO_2)_2$ containing electrolyte showed high overpotentials and very low charge efficiency. As with the cyclic voltammetry the $Na_2Pb(OH)_4$ containing electrolyte showed some promise by giving the lowest overpotentials and good charge balancing. It should be noted, though, that this electrolyte contained only one fifth the concentration of Pb compared to the others tested.

A similar series of chronopotentiometric experiments were performed at a vitreous carbon rotating disc electrode (ω = 900 rpm) to investigate the Pb^{2+}/PbO_2 couple in each of the electrolyte solutions. Each experiment involved three deposition/stripping cycles. Each cycle consisted of a 900 s deposition (j = 50 mA cm^{-2}) followed by anodic dissolution at the same current density until the voltage sharply dropped, indicating the deposit had been consumed. The temperature was maintained at 313 K. With each of the electrolytes the form of the voltage vs. time plots were typical for anodic deposition and cathodic stripping of PbO_2 on a vitreous carbon rotating disc electrode (cf. figure 3.12) except that the plots obtained from the electrolytes containing $Pb(OAc)_2$ and $Na_2Pb(OH)_4$ showed no voltage trough during depositions and with the electrolyte containing $Pb(NO_3)_2$ only a small trough was observed, followed by a small peak before the voltage reached a plateau. Table 6.8 presents the deposition potential (E_c / V vs. SCE), stripping potential (E_d / V vs. SCE), the difference between deposition and stripping potentials ($|E_c - E_d|$ / mV) and charge efficiency ($\frac{Q_d}{Q_c}$ / %) from the third cycle of each experiment.

As with the Pb deposition and stripping the electrolytes containing $Pb(CH_3SO_3)_2$ and $Pb(NO_3)_2$ gave similar voltage vs. time responses, however the charge efficiency for the $Pb(NO_3)_2$ containing solution was substantially lower. The $Na_2Pb(OH)_4$ containing solution showed no features associated with PbO_2 stripping, with the voltage sharply dropping immediately as the cathodic current was applied.

Pb Species	E_c / V vs. SCE	E_d / V vs. SCE	$\lvert E_c - E_d \rvert$ / mV	$\frac{Q_d}{Q_c}$ / %
$Pb(CH_3SO_3)_2$	1.54	1.12	420	89
$Pb(CH_3CO_2)_2$	0.96	0.67	290	61
$Pb(NO_3)_2$	1.50	1.11	390	48
$Na_2Pb(OH)_4$	0.31	-	-	-

Table 6.8: *Data from PbO_2 deposition/dissolution experiments (j = 50 mA cm^{-2}) performed at a vitreous carbon rotating disc electrode (ω = 900 rpm). Temperature maintained at 312 K. Table shows the deposition potential (E_c / V vs. SCE), stripping potential (E_d / V vs. SCE), the difference between deposition and stripping potentials ($\lvert E_c - E_d \rvert$ / mV) and charge efficiency (Q_d/Q_c / %) from the third cycle of each experiment.*

6.6 Chapter 6 Summary

It has been shown that adding sodium ligninsulfonate to the battery electrolyte significantly improves the quality of deposited Pb layers without impairing battery operation or efficiencies to any great extent. The use of this additive inhibits dendrite formation and produces smoother more compact deposits. This is particularly important when using high current densities, which have a higher tendency for dendrite formation. Sodium ligninsulfonate also enables the deposition of considerable Pb and PbO_2 layers and hence enhances the energy storage capacity.

Although the addition of nickel to the electrolyte solution initially reduces the overpotential associated with Pb^{2+}/PbO_2 couple, with extended cycling this effect diminishes and the charge/discharge efficiencies drop compared to without additive. However it should be noted that with the nickel present the voltages, and thus the efficiencies, of the battery are slightly higher than without the additive during the initial periods of discharge. One suggested use for the battery involves load levelling and black start capacity for power stations. In this application the battery would only be partially discharged/charged during load levelling, with only the occasional deep discharge for black

starting. If the higher voltages during the initial stages of discharge were obtainable under such usage the lower overall efficiency would be less significant.

The initial studies of alternative additives were not encouraging, with Fe showing no effect on either of the electrode couples and polyethylene glycol-200 not improving the quality of Pb deposits. However it should be noted that there are a vast number of possible additives that may show more effect.

From the various electrolytes tested, the initial choice of $Pb(CH_3SO_3)_2$ in aqueous CH_3SO_3H shows the most promise for the battery system. $Pb(NO_3)_2$ (0.5 mol dm^{-3}) in aqueous HNO_3 (0.6 mol dm^{-3}) gave similar responses however the efficiencies associated with charge and discharge were lower than with the $Pb(CH_3SO_3)_2$ containing electrolyte. Experiments using $Pb(CH_3CO_2)_2$ (0.5 mol dm^{-3}) and $NaCH_3CO_2$ (0.6 mol dm^{-3}) in aqueous CH_3CO_2H (0.6 mol dm^{-3}) gave lower efficiencies, particularly associated with the Pb^{2+}/Pb couple. Good results were obtained for the Pb^{2+}/Pb couple using the electrolyte containing $Na_2Pb(OH)_4$ (0.1 mol dm^{-3}) in aqueous NaOH (4.6 mol dm^{-3}), however significant problems were encountered with the Pb^{2+}/PbO_2 couple.

Chapter 7: Conclusions and Further Work

This thesis has presented the chemistry, electrochemistry and characterisation of a novel lead-acid flow battery. It has been shown that both the Pb^{2+}/Pb and Pb^{2+}/PbO_2 electrode couples are sufficiently facile to enable high rates of electrodeposition/dissolution ($j > 50$ mA cm^{-2}) in aqueous CH_3SO_3H. The battery has an opencircuit voltage of circa 1.7 V, dependant on state of charge.

The performance of the battery is significantly altered with the addition of certain additives to the electrolyte. The inclusion of small quantities ($\leq$ 1 g dm^{-3}) of sodium ligninsulfonate to the electrolyte considerable retards the formation of Pb dendrites and promotes the deposition of smooth, compact Pb layers.

Within the confines of laboratory operation, the battery performed well. The storage of 576 C cm^{-2} using a current density of 40 mA cm^{-2} was achieved with coulombic and energy efficiencies of 65 % and 47 % respectively. At lower current densities higher eficiencies were readily obtainable ($\frac{Q_d}{Q_c} \geq 80\%$, $\frac{W_d}{W_c} \geq 70$ %). During repetitive cycling the charge and discharge characteristics of the battery tended towards a uniform and repeatable profile.

It is clear that the proposed battery shows some potential, however further work is needed to fully assess the viability of commercial use and a few possible extensions to the project are listed:

♦ *Scaling up*: The flow cell used in this project was designed to accommodate two small electrodes (A = 2 cm^2) and was typically operated with an electrolyte volume of 40 cm^3. Any further investigations would ideally use a scaled up battery, with a larger total electrode area and combination of two or more cells, possibly with a bipolar electrode configuration.

♦ *Extended cycling*: The cycling experiments conducted during this project generally consisted of a short charge period followed complete discharge until the one or

both of the active materials had been fully consumed. Further experiments could involve cycling the battery to the full capacity of the electrolyte ($0.1 \text{ mol dm}^{-3} \leq c_{Pb^{2+}} \leq 1.5 \text{ mol dm}^{-3}$) or more accurately modelling the use expected with a load levelling application.

♦ *Additives*: A small number of additives were evaluated in this project however it is quite possible that superior battery performance could be achieved with any number of alternative additives.

References

[1] A. Price, *Power Eng. Int.* 2001, *107.*

[2] D. W. Murphy, J. Broadhead and B. C. H. Steele, *Materials For Advanced Batteries*, Plenum Press, London, 1979.

[3] R. M. Dell and D. A. J. Rand, *Understanding Batteries*, RSC Paperbacks, 2001.

[4] D. Lindenmeyer, H. W. Dommel and M. M. Adibi, *Elect. Power Energ. Sys.* 2001, *23*, 219.

[5] R. M. Dell and D. A. J. Rand, *J. Power Sourc.* 2001, *100*, 2.

[6] J. Kondoh, I. Ishii, H. Yamaguchi, A. Murata, K. Otani, K. Sakuta, N. Higuchi, S. Sekine and M. Kamimoto, *Energ. Convers. Manage.* 2000, *41*, 1863.

[7] M. R. Mohan, S. R. Paranjothi and S. P. Israel, *Electr. Mach. Pow. Syst.* 1997, *25*, 1047.

[8] A. W. Grupping, *Erdol. Kohle. Erdgas.* 1993, *46*, 296.

[9] H. Oman, *IEEE Aero. El. Sys. Mag.* 1996, *11*, 37.

[10] J. M. Iocca, R. W. Potts and A. C. Kelsall, *Power Eng.* 1986, *90*, 30.

[11] K. Okajima, T. Toya and M. Sudoh, *Kagaku Kogaku Ronbun.* 2003, *29*, 255.

[12] S. C. Tripathy and I. P. Mishra, *Energ. Convers. Manage.* 1996, *37*, 1787.

[13] P. Y. Emelin, F. G. Rutberg and B. E. Fridman, *Instrum. Exp. Tech+.* 1993, *36*, 730.

[14] H. Teshima, T. Tawara, J. Kobuchi, T. Suzuki and R. Shimada, *Power Conversion Conference* (Nagaoka) 1997, 701.

[15] T. Ogata, T. Takahashi and R. Shimada, *Power Conversion Conference* (Yokohoma) 1993, 587.

[16] J. R. Hull, T. M. Mulcahy, K. L. Uherka, R. A. Erck and R. G. Abboud, *Appl. Supercond.* 1994, *2*, 449.

[17] D. G. Infield, *Renew. Energ.* 1994, *5*, 618.

[18] N. Koshizuka, F. Ishikawa, H. Nasu, M. Murakami, K. Matsunaga, S. Saito, O. Saito, Y. Nakamura, H. Yamamoto, R. Takahata, Y. Itoh, H. Ikezawa and M. Tomita, *Physica. C.* 2003, *386*, 444.

[19] J. S. Kim and S. H. Lee, *Supercond. Sci. Tech.* 2003, *16*, 473.

[20] P. Tsao, M. Senesky and S. R. Sanders, *IEEE T. Ind. Appl.* 2003, *39*, 1710.

[21] B. Nordell, J. Ritola, K. Sipila and B. Sellberg, *Tunn. Undergr. Sp. Tech.* 1994, *9*, 243.

[22] B. Sanner, C. Karytsas, D. Mendrinos and L. Rybach, *Geothermics* 2003, *32*, 579.

[23] M. Bartolozzi, *J. Power Sourc.* 1989, *27*, 219.

[24] K. Nozaki and T. Ozawa, *Prog. Batteries Solar Cells* 1984, *5*, 327.

[25] F. Beck and P. Ruetschi, *Electrochim. Acta* 2000, *45*, 2467.

[26] D. H. Collins, *Batteries: Research and Development in Non-Mechanical Electrical Power Sources*, Pergamon Press, 1963.

[27] S. Male, *13th International Forum on Electrolysis in the Chemical Industry* (Clearwater Beach, FL) 1999.

[28] A. Price, S. Bartley, S. Male and G. Cooley, *Power Eng. J.* 1999, *13*, 122.

[29] C. J. Rydh, *J. Power Sourc.* 1999, *80*, 21.

[30] I. Tsuda, K. Nozaki, K. Sakuta and K. Kwokawa, *Sol. Energ. Mater. Sol. Cell.* 1997, *47*, 101.

[31] I. Takefumi, K. Takashi, I. Atsuo, K. Kouchei, T. Hara and T. Nobuyuki, *Soc. Automot. Eng. J.* 1999, *13*, 122.

[32] C. Menictas, D. R. Hong, Z. H. Yan, J. Wilson, M. Kazacos and M. Skyllas-Kazacos, *Electrical Engineering Congress 1994(EEC'94)* (Sydney) 1994.

[33] M. Skyllas-Kazacos, D. Kasherman, R. R. Hong and M. Kazacos, *J. Power Sourc.* 1991, *35*, 399.

[34] M. Kazacos and M. Skyllas-Kazacos, *J. Electrochem. Soc.* 1989, *136*, 2759.

[35] P. Lex and B. Jonshagen, *Power Eng. J.* 1999, *13*, 142.

[36] P. C. Butler, P. A. Eidler, P. C. Grimes, S. E. Klassen and R. C. Miles in "*Handbook of Batteries*". (Ed. D. Linden), McGraw Hill, New York, 1994.

[37] W. R. Grove, *Phil. Mag.* 1839, *3*, 127.

[38] A. J. Appleby, *Fuel Cells: Grove Anniversary Symposium '89*, Elsivier, 1990.

[39] W. Ostwald, *Z. Electrochimie* 1894, *1*, 122.

[40] N. N. Greenwood and A. Earnshaw, *Chemistry of the Elements*, Butterworth-Heinemann, Oxford, 1997.

[41] A. T. Kuhn, *The Electrochemistry of Lead*, Academic Press, New York, 1979.

[42] M. Jordan in *Electrodepostion of Lead and Lead Alloys*, (Ed. M. Schlesinger and M. Paunovic), John Wiley and Sons, 2000.

[43] M. D. Gernon, M. Wu, T. Buszta and P. Janney, *Green Chemistry* 1999, *1*, 127.

[44] T. F. Sharpe, *Encyclopedia of Electrochemistry of the Elements*, New York, 1973, p. 304.

[45] C. A. Jackson and A. T. Kuhn, *Industrial Electrochemical Processes*, Elsevier, London, 1971, p. 524.

[46] A. M. Couper, D. Pletcher and F. C. Walsh, *Chem. Revs.* 1990, 837.

[47] D. W. Wabner, H. P. Fritz and R. Huss, *Chem. Eng. Tech.* 1977, *49*, 329.

[48] C. Comninellis and E. Plattner, *J. Applied Electrochem.* 1982, *12*, 399.

[49] N. Munichandraiah and S. Sathyanarayani, *J. Appl. Electrochem* 1987, *17*, 22.

[50] L. Gherardini, P. A. Michaud, M. Panizza, C. Comninellis and N. Vatistas, *J. Electrochem. Soc.* 2001, *148*, D78.

[51] P. K. Shen and X. L. Wei, *Electrochim. Acta* 2003, *48*, 1743.

[52] D. J. Gilroy, *J. Appl. Electrochem.* 1982, *12*, 181.

[53] A. B. Velichenko, *J. Electrochem. Soc.* 2002, *149*, C445.

[54] J. Gonzalez-Garcia, *J. Electrochem. Soc.* 2000, *147*, 2969.

[55] J. Gonzalez-Garcia, *Thin Solid Films* 1999, *352*, 49.

[56] *Croatica. Chimica. Acta.* 2000, *73*, 667.

[57] J. P. Carr and N. A. Hampson, *J. Electrochem. Soc.* 1971, *118*, 1262.

[58] *J. Electrochem. Soc.* 1996, *143*, 1157.

[59] D. Pavlov and B. Monahov, *J. Electrochem. Soc.* 1996, *143*, 3616.

[60] J. Gonzalez-Garcia, *Electroanalysis,* 2001, *13*.

[61] E. Exposito, *J. Power Sourc.* 2000, *87*, 137.

[62] A. B. Velichenko, D. V. Girenko and F. I. Danilov, *Electrochim. Acta* 1995, *40*, 2803.

[63] A. B. Velichenko, *J. Electroanal. Chem.* 1998, *454*, 203.

[64] A. J. Saterlay, *J. Electrochem. Soc.* 2001, *148*, E66.

[65] F. Marken, *Electroanalysis* 1998, *10*.

[66] L. A. Larew, *J. Electrochem. Soc.* 1990, *137*.

[67] H. Chang and D. C. Johnson, *J. Electrochem. Soc.* 1990, *137*.

[68] M. D. Capelato, J. A. Nobrega and E. F. A. Neves, *J. Appl. Electrochem.* 1995, *25*, 408.

[69] E. Hwang, *Bull. Korean Chem. Soc.* 1994, *15*.

[70] J. Lee, H. Verela, S. Uhm and Y. Tak, *Electrochem. Comm.* 2000, *2*, 646.

[71] F. Beck and H. Bohn, *Berchte Der Bunsen-Gesellschaft Fur Physikalische Cheme. Freicher Zeitshrift Fur Electrocheme* 1975, *79*, 233.

[72] M. Fleischmann and M. Liler, *M. Trans. Faraday Soc.* 1958, 1370.

[73] S. Fletcher, *J. Electroanal. Chem.* 2002, *530*, 119.

[74] S. Fletcher, *J. Electroanal. Chem.* 2002, *530*, 105.

[75] A. B. Velichenko, D. V. Girenko and F. I. Danilov, *J. Electroanal. Chem.* 1996, *405*, 127.

[76] A. Hazza, D. Pletcher and R. Wills, *Phys. Chem. Chem. Phys.* 2004, *6*, 1773.

[77] S. C. Baker, D. P. Kelly and J. C. Murrell, *Nature* 1991, *350*, 627.

[78] J. P. Schrodt, W. T. Otting, J. O. Schoegler and D. N. Craig, *Trans. Electrochem. Soc.* 1946, *90*, 405.

[79] J. C. White, W. H. Powers, R. L. McMurtric and R. T. Pierce, *Trans. Electrochem. Soc.* 1947, *91*, 1947.

[80] G. D. McDonald, E. Y. Weissman and T. S. Roemer, *J. Electrochem. Soc.* 1972, *119*, 660.

[81] F. Beck in *Lead Batteries*, United States Patent: 4,001,037, 1977.

[82] Wurmb in *Secondary Battery*, United States Patent: 4,092,463, 1978.

[83] P. Henk in *Lead Salt Electric Storage Battery*, United States Patent: 4,331,744, 1982.

[84] P. Henk in *Lead Salt Electric Storage Battery*, United States Patent: 4,400,499, 1983.

[85] A. Hazza, Thesis: A Preliminary Study of A Novel and Simple Redox Battery for Load Levelling, Southampton, 2001.

[86] F. C. Walsh, *A First Course in Electrochemical Engineering*, The Electrochemical Consultancy, Romsey, 1993.

[87] D. Pletcher and F. C. Walsh, *Electrochemical Technology for a Cleaner Environment*, The Electrosynthesis Co., Lancaster NY, 1992.

[88] J. M. Friedrich, C. Ponce-de-Leon, G. W. Reade and F. C. Walsh, *Electroanal. Chem.* 2004, 203.

[89] D. Pletcher, I. Whyte, C. Walsh and J. P. Millington, *J. Appl. Electrochem.* 1991, *21*, 659.

[90] R. Parsons, *Handbook of Electrochemical Constants*, Butterworths Scientific Publications, London, 1959.

[91] M. D. Gernon, T. Buszta and P. Janney in *The Substitution of Environmentally Friendly Methanesulfonic Acid for Fluoroboric Acid and Fluorosilicic Acid in Indusrial Electrochemicl Processes Involving Lead*, 1999.

[92] V. M. M. Lobo, *Handbook of Electrolyte Solutions*, Elsevier, 1989.

[93] D. Pletcher, *A First Course in Electrode Processes*, The Electrochemical Consultancy, 1991.

[94] K. M. Tyutina, G. A. Selivanova and L. K. Niem, *Protect. Met.* 1995, *31*, 86.

[95] C. S. Chen, C. C. Wan and Y. Y. Wang, *J. Chin. Chem. Eng.* 1999, *30*, 199.

[96] C. S. Chen, C. C. Wan and Y. Y. Wang, *Trans, Inst. Met. Finish.* 1998, *76*, 54.

[97] L. Muresan, L. Oniciu and R. Wiart, *J. Appl. Electrochem* 1994, *23*, 66.

[98] P. Yu and T. J. O'Keefe, *J. Electrochem. Soc.* 1999, *146*, 1361.

[99] F. Beck in *"The Electrochemistry of Lead"* (Ed. A. T. Kuhn), Academic Press, New York, 1979, p. 65.

[100] H. Bode, *Lead-Acid Batteries*, Wiley Interscience, 1977.

[101] M. Schlesinger and M. Paunovic in *"Modern Electroplating"* (Ed. F A Lowenheim) Whiley Interscience 1974.

[102] A. T. Kuhn, *The Electrochemistry of Lead*, Academic Press, 1979.

[103] A. K. Graham and H. L. Pinkerton, *Proc. Am. Electroplat. Soc.* 1963, *50*, 135.

[104] A. K. Graham and H. L. Pinkerton, *Proc. Am. Electroplat. Soc.* 1963, *50*, 139.

[105] D. E. Danly and C. R. Campbell in *Techniques of Electroorganic Synthesis, Part III*, (Ed. N. L. Weinberg and B. V. Tilak), Wiley, New York, 1982, 287.

[106] C. A. Jackson and A. T. Kuhn in *"The Electrochemistry of Lead"* (Ed. A. T. Kuhn), Elsevier, London, 1971. p. 535.

[107] F. Caldara, A. Delmastro, G. Fracchia and M. Maja, *J. Electrochem. Soc.* 1980, 1869.

[108] A. Baggio, M. Maja and N. Penazzi, *J. Power Sources* 1983, *9*, 221.

[109] S. Treimer, J. Feng, M. D. Scholten, D. C. Johnson and A. J. Davenport, *J. Electrochem. Soc.* 2001, E459.

[110] D. C. Johnson, H. Chang, J. Feng and W. Wang (Ed. J. D. Genders and N. L. Weinberg), The Electrosynthesis Co., Lancaster NY, 1992.

[111] D. Pletcher and Y. Mohd *Unpublished work.*

[112] M. I. Smirnov, K. M. Tyutina and A. N. Popov, *Russ. J. Electrochem.* 1994, *31*, 498.

[113] M. Goodenough and K. J. Whitlaw, *Trans, Inst. Met. Finish.* 1989, *67.*